Doctoral Thesis

Transition Metal Based Nanomaterials for Hydrogen and Oxygen Involving Energy Conversion Reactions

Siraj Sultan

Department of Chemistry

Graduate School of UNIST

2020

Transition Metal Based Nanomaterials for Hydrogen and Oxygen Involving Energy Conversion Reactions

Siraj Sultan

Department of Chemistry

Graduate School of UNIST

Transition Metal Based Nanomaterials for Hydrogen and Oxygen Involving Energy Conversion Reactions

A thesis/dissertation
submitted to the Graduate School of UNIST
in partial fulfillment of the
requirements for the degree of
Doctor of Philosophy

Siraj Sultan

January 06/2020
Approved by

Advisor
Prof. Kwang Soo Kim

Transition Metal Based Nanomaterials for Hydrogen and Oxygen Involving Energy Conversion Reactions

Siraj Sultan

This certifies that the thesis/dissertation of Siraj sultan is

Approved

January 06/2020

Advisor: Prof. Kwang Soo Kim

Prof. Hyeon Suk Shin: Thesis Committee Member

Prof. Tae-Hyuk Kwon: Thesis Committee Member

Prof. Jong-Beom Baek: Thesis Committee Member

Prof. Ji Wook Jang; Thesis Committee Member

Abstract

The growing demand for clean energy and the rapid consumption of conventional fossil fuels have provoked considerable research interest in exploring and developing highly efficient with low cost and environment-friendly alternative energy conversion and storage technologies. Many advanced devices and technologies such as water electrolysis, fuel cells and metal-air batteries serve as key components for storage and clean energy conversion. The core of these clean energy conversion devices and technologies are a series of electrochemical reactions, which include hydrogen evolution reaction (HER) at the cathode and oxygen evolution reaction (OER) at the anode of an electrolytic cell producing molecular hydrogen and oxygen, respectively; and oxygen reduction reaction (ORR) that occur on the cathode of the hydrogen-oxygen fuel cell. The commercialization of the above mentioned clean energy conversion devices and technologies depends on the synthesis and development of low-cost electrocatalysts that can efficiently catalyze these reactions on the surface of each electrode to achieve a very high current density at very low overpotential. To date, platinum-based nanomaterials remains the most active electrocatalyst for HER and ORR, whereas the oxides of ruthenium and iridium are highly efficient towards OER. However, the high cost and scarcity of these precious metals limits their widespread practical applications in clean and renewable energy technologies and devices. Therefore, searching for novel inexpensive transition metal-based electrocatalysts which show high electrocatalytic activity and stability toward these key reactions that can facilitate the realization of eco-friendly sustainable energy infrastructure are highly desirable. In this regard, this thesis aims to synthesis of metal alloy nanoparticles encapsulated/supported in nitrogen-rich graphitic tube/reduced-graphene-oxide for catalyzing HER, ORR and OER reactions.

In the first chapter, we briefly introduce the general background, basic mechanism and essential chemical reactions of electrochemical HER, OER and ORR reactions as well as general parameters for scientific assessment of the catalytic activity of electrocatalysts. In second chapter, we synthesize a new class of electrocatalyst [$Fe_3Co(PO_4)_4$@reduced-graphene-oxide(rGO)] showing outstanding OER performance (much higher than state-of-the-art Ir/C catalyst), the design of which was aided by first-principles calculations. This electrocatalyst displays low overpotential (237 mV at high current density 100 $mA{\cdot}cm^{-2}$ in 1M KOH), high turnover frequency (TOF: 0.54 s^{-1}), high Faradaic efficiency (98%) and long-term durability. The remarkable performance is ascribed to the optimal free energy for OER at Fe sites and efficient mass/charge-transfer. When a $Fe_3Co(PO_4)_4$@rGO anodic electrode is integrated with a Pt/C cathodic electrode, the electrolyzer requires only 1.45 V to achieve 10 $mA{\cdot}cm^{-2}$ for whole-water-splitting in 1M KOH (1.39 V in 6M KOH) which is much smaller than commercial Ir-C//Pt-C electrocatalysts. This cost-effective powerful oxygen production material with carbon supporting-substrates offers a great promise for water splitting.

The third chapter describes our approach to hydrogen production in acidic water using a multicomponent catalyst with an ultralow Pt loading (1.4 μg per electrode area (cm^2)) supported on melamine-derived graphitic tubes (GTs) that encapsulate a FeCo alloy and have Cu deposited on the inside tube walls. With a 1/80th Pt loading of a commercial 20% Pt/C catalyst, the catalyst achieves a current density of 10 mA cm^{-2} at an overpotential of 18/66 mV in 0.5M- H_2SO_4/ 0.1M-$HClO_4$ solution, and shows a turnover frequency of 7.22 s^{-1} (96 times higher than that of the Pt/C catalyst) and long-term durability (10,000 cycles). We propose that a synergistic effect between the Pt clusters and single Pt atoms embedded in the GTs enhances the catalytic activity.

In fourth chapter, we introduce the precise tuning of the atomic ratio of Fe and Co encapsulated in melamine-derived nitrogen-rich graphitic tube (NGT) for ORR catalyzing reactions. The $Co_{1.08}Fe_{3.34}$ hybrid with metal-nitrogen bonds ($Co_{1.08}Fe_{3.34}$@NGT) shows remarkable ORR catalytic activities (80 mV higher in onset potential and 50 mV higher in half-wave potential than those of state-of the- art commercial Pt/C catalysts), high current density, and stability. In acidic solution, **1** also shows compatible performance to commercial Pt/C in terms of ORR activity, current density, stability, and methanol tolerance. The high ORR activity is ascribed to the co-existence of Fe-N, Co-N, and sufficient metallic FeCo alloys which favor faster electron movement and better adsorption of oxygen molecules on the catalyst surface. In the alkaline anion exchange membrane fuel cell setup, this cell delivers the power density of 117 mW cm^{-2}, demonstrating its potential use for energy conversion and storage applications.

Table of Contents

List of Figures

List of Tables

Abbreviations

1. OER: Oxygen Evolution Reaction
2. HER: Hydrogen Evolution Reaction
3. HOR: Hydrogen Oxidation Reaction
4. ORR: Oxygen Reduction Reaction
5. LSV: Linear sweep voltammetry
6. ΔG_{H^*}: Hydrogen adsorption free energy
7. AFC: Alkaline fuel cell
8. MCFC: Molten carbonate fuel cell
9. SOFC: Solid oxide fuel cell
10. PEMFC: Proton exchange membrane fuel cell
11. AAEMFC: Alkaline anion exchange membrane fuel cell
12. GTs: Graphitic tubes
13. TOF: Turnover frequency
14. CV: Cyclic voltammetry
15. RHE: Reversible hydrogen electrode
16. SCE: Saturated calomel electrode
17. FE-SEM: Field-Emission Scanning Electron Microscope
18. TEM: Transmission Electron Microscope
19. HRTEM: High resolution transmission electron microscope
20. HAADF-STEM: High-angle annular dark-field scanning transmission electron microscopy
21. EDX: Energy-dispersive X-ray spectroscopy
22. EELS: Electron energy loss spectroscopy
23. XRD: X-ray Diffraction
24. ICP-OES: Inductively Coupled Plasma Optical Emission Spectroscopy
25. ICP-MS: inductively coupled plasma–mass spectrometry
26. ICP-AES: inductively-coupled-plasma atomic-emission-spectroscopy
27. XPS: X-ray Photoelectron Spectroscopy
28. FT-EXAFS: Fourier transform of the extended X-ray absorption fine structure
29. XAS: X-ray absorption spectra
30. XANES: X-ray absorption near edge structure
31. PAL: Pohang Accelerator Laboratory
32. CN: coordination number
33. DFT: Density functional theory
34. CNT: Carbon nanotube
35. FT: Fourier transform
36. FT-IR: Fourier-transform infrared spectroscopy
37. BET: Brunnauer-Emmett-Teller
38. BJH: Barrett–Joyner–Halenda

39. GTo: pristine GT, GTN: N-doped GT, GTp; pyridinic-N-doped GT
40. EIS: Electrochemical impedance spectroscopy
41. PDOS: Projected density of states
42. NPs: Nanoparticles
43. σ: Electrical conductivity
44. NGT: Nitrogen-rich graphitic tube
45. RDE: Rotating disk electrode
46. RRDE: Rotating ring-disk electrode
47. ECS: Electrochemical active sites
48. C_{dl}: Double-layer capacitance
49. RF: roughness factor
50. GDL: Das diffusion layer
51. IPA: Isopropyl alcohol
52. MEA: Membrane electrode assembly
53. ADTs: Accelerated durability tests
54. OCV: Open-circuit voltage
55. K–L: Koutecky–Levich
56. rGO: reduced-graphene-oxide
57. Hg/HgO: Mercury-Mercurous sulfate
58. GCE: Glassy carbon electrode
59. NF: Nickel foam
60. CA: Chronoamperometry
61. GGA: Generalized gradient approximation
62. TS: Tkatchenko-Scheffler
63. η: overpotential
64. FFT: Fast-Fourier-transform

Chapter 1

1. General Introduction

1.1. Background

The aggravated energy crisis due to the rapid depletion of conventional fossil fuels is a hot and interesting topic in modern society, which encourages the global intense research effort into the energy field.[1-3] Especially the geopolitical anxieties and the increasing threats in climate changes and global warming stimulate the movement toward clean, stable, eco-friendly and renewable benign energy resources.[1-4] The current demand for global energy is around 15 terawatts and the light irradiance from the sun can provide larger than 50 terawatts energy.[4-5] Since other resources of renewable energy are limited and lower than our current societal needs, thus the sun is the most plentiful and ultimate energy resource. The existing photovoltaic technologies and devices can convert the sunlight energy into an electrical potential, however, sun shining is limited to a few hours in each day, and additionally due to shadowing it is not equally distributed across the entire earth's surface. Moreover, the light rays are spread over the whole surface of the earth and decreasing their power to a high extent. Thus, due to both diffuse and intermittent nature of sunlight energy, alternative devices and methods for storing and converting this light energy into potential energy are highly required.

Many advanced devices and technologies for conversion of clean energy, for example, metal-air batteries, CO_2 to fuel conversion, water electrolysis, and fuel cells are the subject of fundamental and utilitarian perspectives.[6-9] These technologies and devices work as key components for utilization of sustainable energy have been extensively discussed by the government and academic organizations.[6-9] The heart of these clean energy conversion technologies and devices are a series of basic electrocatalytic processes, which include electrochemical oxygen evolution reaction (OER) and hydrogen evolution reaction (HER) that occur on the anode and cathode of water electrolyzer for generating molecular oxygen and hydrogen gases, respectively; and hydrogen oxidation reaction (HOR) and oxygen reduction reaction (ORR) at the anode and cathode of hydrogen-oxygen liquid fuel cell, respectively (note: oxygen and hydrogen gases from water electrolyzer can be recombined in fuel cell at point of usage for generation of electricity).[10] Figure 1.1 presents the steady-state linear sweep voltammetry (LSV) curves and typical half-cell reactions for HOR, HER, OER and ORR. The equations in figure 1.1 for the above-mentioned four reactions can be grouped into two couples of reversible reactions. One of the couple reactions are hydrogen involving HOR and HER reactions as exemplified by a red curve at equilibrium potential of 0 V versus RHE (reversible hydrogen electrode) and the other couple is OER and ORR reactions illustrated by a blue colour at equilibrium potential of 1.23 V versus RHE. Although both couple reactions are reversible, but the LSV shape of all the four half-cell reactions are not the same: OER and HER usually follow the Butler–Volmer model (the reaction rate is controlled by the

rate of electrochemical charge transfer process),[10] while for ORR and HOR (due to the limitation in the rate of mass transfer process) the current approach to a constant value at large overpotentials.[10]

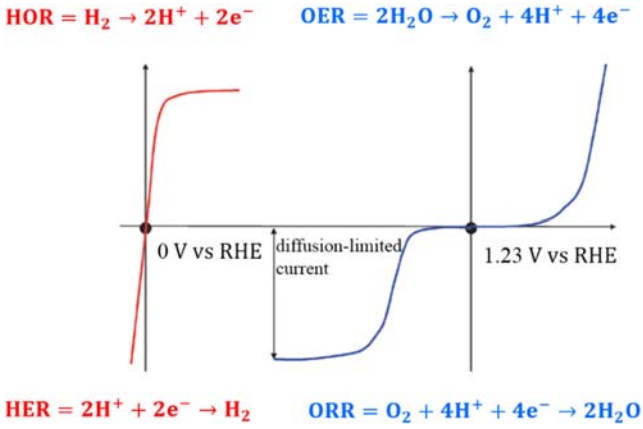

Figure 1.1. linear sweep voltammetry curves and overall reaction equations for two couple of the key energy-related electrochemical HOR/HER and OER/ORR reactions. Blue and red curves refer to the oxygen-involving and hydrogen-involving reactions. The lines are without a scale. Reproduced with permission from ref.[10] Copyright 2015 Royal Society of Chemistry.

Recently these HOR/HER and OER/ORR reactions have gained extensive investigation in a clean and renewable energy field and also in the exploring of more and high complicated multi-electron transfer reactions. In electrocatalysis, the HOR/HER is considered as the simplest reactions due to its limited reaction path with the involvement of two electrons and one reaction intermediate and therefore its theoretical activity can be investigated only from hydrogen adsorption free energy (ΔG_{H^*}).[11-13] In contrast, OER/ORR operates in more complex four proton-coupled electron transfer reaction and therefore its theoretical activity can be estimated from the free energy changes of each step of the reaction.[14-17]

The feasibility and kinetics of these key electrochemical reactions influence significantly the output and performance of the aforementioned renewable clean energy conversion technologies and devices. The most debatable and critical problem in the energy field is how to catalyze effectively these cornerstones HOR/HER and OER/ORR reactions on the surface of each electrode to achieve a very high current density at very low overpotential. Generally, the kinetics of HOR and HER half-cell reactions is facile and can easily occur on several metal-based electrocatalysts at low overpotential,[11-13] while OER and ORR half-cell reactions are kinetically sluggish and require high overpotential.[14-17] For example, the major cause of the low efficiency of water electrolyzer and the proton exchange membrane fuel cells are the poor electrocatalytic performance of the anodic OER electrode (in water electrolyzer)[18] and the cathodic ORR electrode (in hydrogen/oxygen fuel cells).[7, 19] Therefore, for industrial application noble metals such as iridium (Ir), ruthenium (Ru), and platinum (Pt) based electrocatalysts are used for obtaining the favorable reaction kinetics of the OER and ORR reactions respectively.[20-22] Besides the

high electrocatalytic activity requirement, the main issues associated with the noble metal-based electrocatalysts are their high cost and scarcity, which put them out of reach from large-scale practical applications in clean and renewable energy technologies and devices.[23-26] Therefore, the development and synthesis of novel low-cost transition metal-based catalysts that show higher electrocatalytic activity toward these key reactions with high durability and can facilitate the realization of eco-friendly sustainable energy infrastructure are highly desirable. At present, Significant breakthroughs have been made in the synthesis of non-noble metal-based catalysts for the electrocatalysis of HER, OER and ORR reactions, but unfortunately, the catalytic activity or stability of the most reported catalysts are far away than the activity of commercially available HER, OER and ORR catalysts.[7, 11-26] In this esteem, further research for synthesis and development of extremely competent electrodes for water electrolyzer (HER and OER electrodes) and fuel cell (cathodic ORR electrode) that can be applicable at industrial scale is highly required. The objective of this thesis is concerned with the synthesis and development of different electrode materials and their potential applications for hydrogen-and-oxygen-related energy conversion reactions. In this chapter, we will first introduce about the basic mechanistic study and catalyst selections for water splitting (HER/OER) and fuel cell (ORR) and then in the next chapters, we will present our research work which will provide a thoughtful understanding for the electrode selection and potential avenues for hydrogen-and-oxygen-related energy conversion reactions.

1.2. Water splitting

Water splitting is a two half-cell reactions, in which hydrogen is produced at the cathode (known as hydrogen evolution reaction: HER) and oxygen is produced at the anode (known as oxygen evolution reaction: OER). Figure 1.2 illustrates the simplest water splitting electrolyzer in which a cathode and an anode are immersed in a conductive electrolyte separated by a membrane and connected by an external power circuit. In water electrolyzer, the water is first oxidized at an anode and generating the molecular oxygen and H^+ ions (Anode Reaction: $2H_2O \rightarrow O_2 + 4H^+ + 4e^-$). The generated H^+ ions move across the applied membrane to the cathode and electrons through the external circuit. At the cathode, the H^+ combine with the electrons from the external circuit forming the molecular hydrogen according to the reaction (Cathode Reaction: $4H^+ + 4e^- \rightarrow 2H_2$). In water electrolyzer, both cathodic HER and anodic OER are fundamental and highly demanding reactions for which the change in Gibbs free energy (ΔG) is 237.2 kJ mol^{-1} (equivalent to a cell voltage of 1.23 V= thermodynamic potential).[26-27] However, in real water electrolyzer, the hydrogen and oxygen are generating at larger overpotential (due to some kinetic barriers at cathode and anode sides of water electrolyzer) than the thermodynamic potential. This large overpotential can be overcome only with the development of highly active cathodic and anodic electrode materials. The electrode material for water splitting would have the following important characteristic properties: (i) high efficiency; (2) high electrocatalytic activity and stability in wide pH ranges; (3) low cost and plentiful resources; (4) eco-friendliness; and (6) the abilities to integrate for both HER and OER in water electrolyzer.

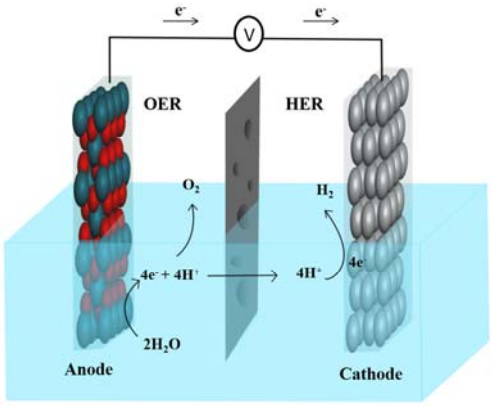

Figure 1.2. Schematic of an electrolysis cell for whole water splitting.

The highly efficient and stable cathodic and anodic materials for water electrolyzer can be achieved only by knowing the fundamental theoretical and experimental concepts of HER and OER reactions on the electrode surface. It is documented that the electrocatalytic activity of HER catalyst is correlated with Gibbs free energy of the H^+ adsorption (ΔG_{H^*}), while the activity of OER catalyst depends on the adsorption free energies of OH/O/OOH (ΔG_{OH^*}, ΔG_{O^*}, ΔG_{OOH^*}, * represents the active sites on the catalyst surface) reaction intermediates.[28-30] Plotting the HER exchange current density versus ΔG_{H^*} (HER structural parameters) and the OER overpotential versus $\Delta G_{O^*} - \Delta G_{OH^*}$ (adsorption free energies of OER reaction intermediates) for different transition metals give triangular-shaped volcano plots (figure 1.3a, b) [28-30], which disclose that there is an optimal binding energy at which the catalyst can show maximum catalytic activity for HER/OER reactions. This behavior of HER/OER volcano plots is related to the general explanatory paradigm in heterogeneous catalysis and electrocatalysis of the Sabatier principle, which stated that the efficient electrocatalytic activity from the catalyst can be obtained when its catalyzing surface have optimal binding interaction or free energy for the reaction intermediates.[1, 31] In other words, the active and efficient electrocatalyst will bind the reactant intermediate neither too weekly nor too strongly.[1, 31] If the reaction intermediates bind very weakly to the active catalytic sites, the surface of the electrocatalyst will be unable to stimulate it for the fast and proper reaction, while if they bind very strongly, they will occupy and block most of the active catalytic sites and will hinder the effective reactions.[1, 31] In each specific case of HER, this general paradigm can be guided from the computation of ΔG_{H^*} on the catalyst surface, which is the most common and reasonable descriptor for determining HER activities for a variety of metals, non-metals, and alloys. In 1957, Parsons demonstrated that the catalyst surface having ΔG_{H^*} near to zero will be very active for HER catalysis.[32] It can be seen from Figure 1.3 that the metals (Pt, Rh, Re, and Ir) which are located near the apex of HER volcano plot have the optimal binding energy for hydrogen atoms. In the case of OER volcano plot, the theoretical overpotential versus the ($\Delta G_{O^*} - \Delta G_{OH^*}$) shows good consistency with the electrocatalytic activity for water oxidation.[30] The metal oxides located at the bottom of the volcano

plot such as ReO_2, NbO_2, VO_2, CrO_2, and SnO_2 exhibit high overpotential for water oxidation due to their weak or strong binding interaction with OER intermediate species (O*, OH* and HOO*). The metal oxides at or near the apex of OER volcano plot such as IrO_2, RuO_2, NiO_x, Co_3O_4 and PtO_2 have optimal binding strengths for OER intermediate species and satisfy small overpotential for water oxidation reactions.[30, 33] However, most of the efficient HER/OER materials which are located at or near the apex of HER/OER volcano plots are expensive noble metals/metal oxides, which limits their widespread industrial applications.[33-34] Therefore, most of the research efforts for finding and designing efficient HER/OER electrocatalysts are diverting toward Ni, Co, and Fe based materials which are next to noble metals in the volcano plots.

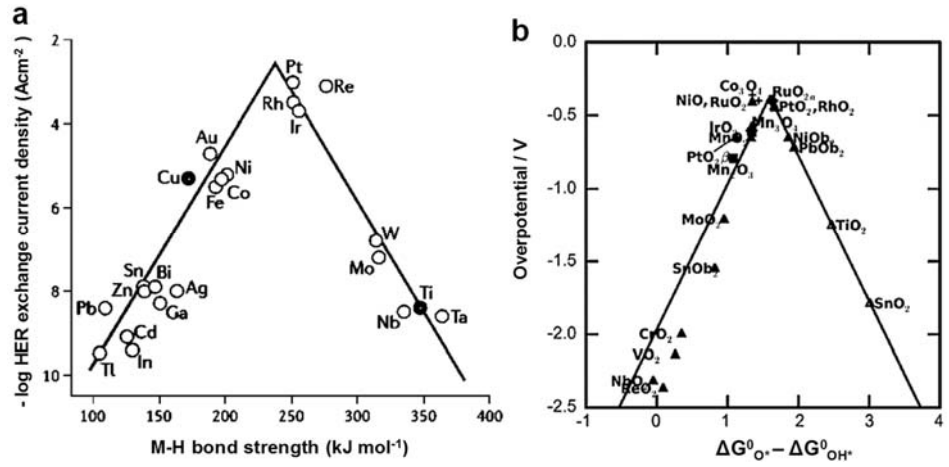

Figure 1.3. Volcano plots for **(a)** hydrogen evolution reaction Reproduced with permission from ref.[29] Copyright 1972 Elsevier, Inc. **(b)** oxygen evolution reaction. Reproduced with permission from ref.[30] Copyright 2011 John Wiley and Sons.

The volcano plots are providing valuable guidelines for understanding and designing efficient electrocatalysts in view of controlling the adsorption energy on catalyst surface for HER/OER intermediates. However, in addition to material selection for fabricating efficient electrocatalysts, the rational design of catalysts in terms of structure and morphology can be used to improve the catalytic performance of HER and OER. The synthesized catalyst would have the following characteristic feature for better performance: (1) large surface area and high density of active sites, (2) high catalytic activity and a large number of active sites, (3) improved electrical contact to active sites, (4) increased open spaces and porosity among adjacent nanostructures of the catalyst for efficient charge transport and electrolyte permeation into the deep portion of catalyst surface, and (5) increased crystal and topological defects which increase the electron density and conductivity of the materials.

1.3. Basic mechanistic study of HER

HER is a simple two electrons half-cell reaction taking place in two different individual steps (figure 1.4).[35] In the first step of HER, the proton (H^+) is discharging from the electrolyte and forming H^* intermediate by receiving an electron from the electrode surface, which is call discharging or Volmer reaction.[35] As HER is either proceeding in an acidic or basic electrolyte. In acidic electrolyte, the source of H^+ is hydronium ion (H_3O^+), while in basic solution the source of H^+ is a water molecule.[11] In the second reaction step, the formation of molecular hydrogen gas in both acidic/basic solutions may occur via two different reaction mechanisms (Volmer–Tafel or Volmer–Heyrovsky mechanism), depending on the coverage of H^* on the electrode surface.[36] If the H^* coverage on the electrode surface is low, then single H^* will combine with H^+ and finally will receive an electron from the electrode surface to form molecular hydrogen, known as atom + ion reaction or Volmer Heyrovsky mechanism.[27, 37] In contrast, if the H^* coverage on the electrode surface is large, then two adjacent H^* will simply recombine for the formation of molecular hydrogen, known as combination reaction or Volmer Tafel mechanism.[27, 36] Moreover, the ΔG_{H^*} value of the catalyst surface is frequently accepted as a good descriptor for the rate-determining of the HER reaction. If the ΔG_{H^*} value of the catalyst is more negative, the binding of H^* to the electrode surface will be more favorable and the initial reaction (Volmer step) will be very easy; however, at a larger negative value, the second reaction (Tafel or Heyrovsky step) would be highly difficult. In contrast, if the catalyst surface has a more positive ΔG_{H^*} value, the whole HER reaction will be slow and ineffective due to weak binding interactions of H^+ to the electrode surface. Therefore, HER active catalyst should have nearly zero ΔG_{H^*} value.

The theoretical valve of Tafel slope for three different HER reaction kinetics has been calculated from the well-known Butler-Volmer equation,[37] such as; (i) if the H^+ discharging in Volmer step is fast and the molecular hydrogen are generating by combination rate-determining reaction process (Tafel mechanism), the slope value should be 2.3RT/2F (Tafel slop = 29 $mVdec^{-1}$ at 25 °C); (ii) if the H^+ discharging reaction is fast and molecular hydrogen are generating by atom + ion reaction process (Heyrovsky mechanism), the slope value should be 4.6RT/3F (Tafel slop = 38 $mVdec^{-1}$ at 25 °C); if the H^+ discharging reaction is slow and the molecular hydrogen are generating by Tafel mechanism or Heyrovsky mechanism, the slope value should be 4.6RT/F (Tafel slop = 116 $mVdec^{-1}$ at 25 °C). The detail possible HER reaction mechanism with the Tafel slope valve are summarized in figure 1.4.

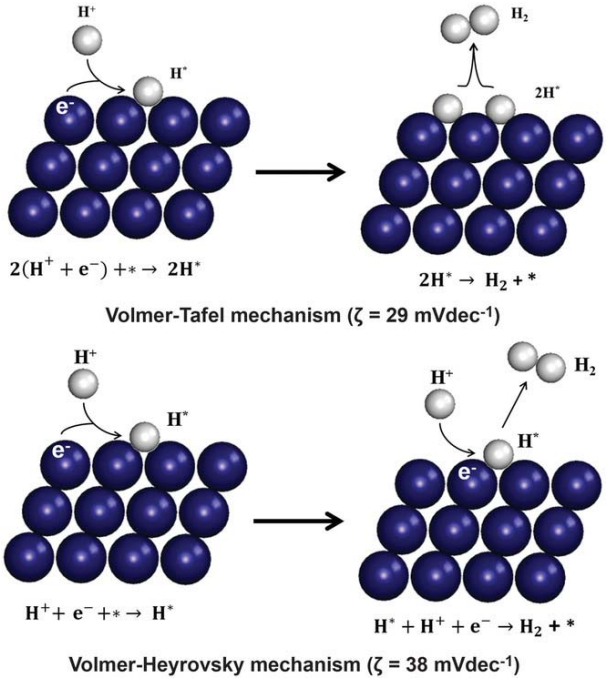

Figure 1.4. HER mechanisms on the electrode surface of the catalyst. If the theoretical Tafel slope is ~29 mVdec^{-1}, the possible HER mechanism on the electrode surface of the catalyst will be Volmer-Tafel. The HER mechanism will be Volmer-Heyrovsky, the Tafel slope is ~38 mVdec^{-1}. In HER the * denotes the active sites of the catalyst; H* denotes the adsorbed hydrogen to the active site of the catalyst. Copyright 2019 John Wiley and Sons.

1.4. Basic mechanistic study of OER

OER in water splitting is a sluggish oxidative half-cell reaction which generates a molecular oxygen through a four electron-proton couple reaction process.[28, 38] The OER process proceeds in four main steps with involvements of OH*, O* and OOH* intermediates in both acidic and basic conditions.[28, 38] However, the initiation and the pathways of the OER process depends on the pH of the electrolyte.[28, 38] In acidic solution, the OER reactions start from the oxidation of water molecules, while in basics solutions, its start from the oxidation of the hydroxyl group.[28, 38] The proposed OER reaction mechanism with free energies are summarized in equations 1.1 to 1.8.

The OER reaction mechanism with free energies in acidic conditions (equations 1.1-1.4):

$$H_2O + * \rightleftharpoons OH^* + (H^+ + e^-)$$
$$\Delta G_1 = \Delta G_{OH^*} - eU + KT\ln[H^+] \qquad (1.1)$$

$$OH^* \rightleftharpoons O^* + (H^+ + e^-)$$
$$\Delta G_2 = \Delta G_{O^*} - \Delta G_{OH^*} - eU + KT\ln[H^+] \qquad (1.2)$$

$$O^* + H_2O \rightleftharpoons OOH^* + (H^+ + e^-)$$
$$\Delta G_3 = \Delta G_{OOH^*} - \Delta G_{O^*} - eU + KTln[H^+] \quad (1.3)$$

$$OOH^* \rightleftharpoons * + O_2 + (H^+ + e^-)$$
$$\Delta G_4 = \Delta G_{O_2} - \Delta G_{OOH^*} - eU + KTln[H^+] \quad (1.4)$$

The OER reaction mechanism basic conditions (equations 1.5-1.8):

$$OH^- + * \rightleftharpoons OH^* + e^- \quad (1.5)$$

$$OH^* + OH^- \rightleftharpoons O^* + H_2O + e^- \quad (1.6)$$

$$O^* + OH^- \rightleftharpoons OOH^* + e^- \quad (1.7)$$

$$OOH^* + OH^- \rightleftharpoons * + O_2 + H_2O + e^- \quad (1.8)$$

Where, * denote the active catalytic sites of the catalyst and OH*, O* and OOH* indicates the reactions intermediates, which are similar in acidic/basic electrolytes. Therefore, the changes in free energies of each step in OER reactions in acidic/basic electrolytes are calculated through the same energies equations (equations 1.1-1.4). The theoretical overpotential of electrocatalyst for OER catalyzing is calculated from the maximum value differences of ΔG_1 to ΔG_4 according to the following equation (1.9).

$$\eta^{OER} = \max(\Delta G_1, \Delta G_2, \Delta G_3, \Delta G_4)/e - 1.23\ V \quad (1.9)$$

According to Density functional theory (DFT) calculations, the OER overpotential is effected from the high energy barriers of ΔG_{OH^*}, ΔG_{O^*} and ΔG_{OOH^*} intermediates (figure 1.5).[30, 39-40] For example, the paper of Rossmeisl group demonstrated that at standard conditions (T= 298.15 K, pH=0 potential U=0 vs. standard hydrogen electrode) the free energy of each reaction step in ideal OER electrocatalyst is 1.23 eV (i.e. $\Delta G_{OOH^*} - \Delta G_{OH^*}$ =2.46/2=1.23 eV, red colour line in figure 1.5).[40] However, in case of real ORE electrocatalyst (i.e. $LaMnO_3$), the differences in energy changes during the conversion of OH* to OOH* is about 3.22 eV instead of 2.46 eV (green line in figure 1.5), representing that the OH* → O*→ OOH* reaction intermediates are the main hindrance in OER process.[40] Thus, the overpotential for OER process can be decreased by designing an active electrocatalyst which can reduce ΔG correlated to the formation of OOH* in water oxidation reactions.

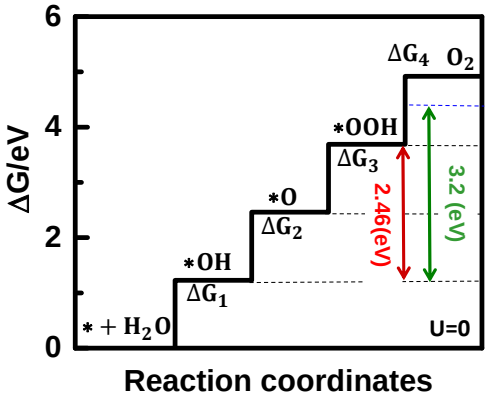

Figure 1.5. The diagrammatic representation of standard free energy changes during each step of OER reaction intermediates using a real and ideal electrocatalyst. The red and green lines represent the standard free energy changes for ideal electrocatalyst (2.46 eV) and green line for real electrocatalyst ($LaMnO_3$: 3.22 eV). Reproduced with permission from ref.[30] Copyright 2011 John Wiley and Sons.

1.5. Fuel cell

Fuel cells are more promising, secure, and environment-friendly devices than the existing fuel-based combustion systems.[41-42] As in fuel cells, there is no moving or combustion part, because, they are converting directly the chemical energy of fuels (Hydrogen, methanol, hydrocarbons) into electrical energy, thereby generating power with minimal pollutants and high efficiency (its theoretical efficiency can reach to ~ 80 %, while in fuel-based combustion system the theoretical efficiency is limited to ~20%).[43-45] In the past half-century, various types of the fuel cell such as alkaline fuel cell (AFC), molten carbonate fuel cell (MCFC), solid oxide fuel cell (SOFC), proton exchange membrane fuel cell (PEMFC) and alkaline anion exchange membrane fuel cell (AAEMFC) has been developed.[46-47]Among these different fuel cells, the AFC was successfully used in the United States Apollo project (human spaceflight program), which is the first implemented fuel cell in practical applications.[48] However, AFC is very sensitive to CO_2 poisoning[49] and therefore its further developments for more terrestrial application in the 1970s and 1980s were unsuccessful. In the last few decades, enormous research work focused on the development of PEMFC owing to its high power density generation and practical applications in Vehicles. But the PEMFC depend on expensive Pt-based electrocatalysts which put them out of reach from widespread practical applications.[50-51] To overcome this difficulty, AAEMFC were proposed and investigated intensively in the last decade. By switching from PEMFC to AAEMFC, it is possible to replace the Pt for the cathode reaction in a fuel cell with a nonprecious electrocatalyst, because in AAEMFC the alkaline environment is more suitable for non-noble metal-based electrocatalysts with faster and facile electrochemical kinetics compared to the acidic solution in PEMFC.[52-53] Both PEMFC and AAEMFC are typical hydrogen/oxygen (H_2/O_2) fuel system which has been considered in this research work.

Figure 1.6 shows the basic operating principle and working conditions of PEMFC and AAEMFC. In PEMFC the hydrogen fuel is fed continuously to anode and oxygen to the cathode (Figure 1.6a). At an anode, the hydrogen dissociates into protons (H^+) with the release of electrons, which is called hydrogen oxidation reaction (HOR: equation 1.10). The H^+ ions permeate via proton exchange membrane (PEM) and the electrons travel through the external circuit to the cathode, where, they combine with the oxygen molecules forming the water molecules and generates the output current of the fuel cell, which is called oxygen reduction reaction (ORR: equation 1.11).

The structure of AAEMFC is almost similar to that of PEMFC except for a few differences, such as; solid membrane (in AAEMFC the membrane is an anion exchange membrane (AEM) between cathode and anode, while in PEMFC the membrane is PEM between cathode and anode) and charge carrier (in AAEMFC the OH^- is transporting from the cathode to the anode through AAEM, while in PEMFC the H^+ is transporting from the anode to cathode through PEM). In detail, the hydrogen fuel in AAEMFC is provided at the anode side and oxygen/water through the cathode side (Figure 1.6b). At cathode, the oxygen molecules are reduced to OH^- ions and migrates through AEM to the anode (equation 1.13). At the anode, the OH^- ions react with hydrogen and forming the water molecules with the release of electrons (equation 1.14). Finally, the resulted electrons travel toward cathode through the external circuit and generating the output current of the full electrochemical reaction.

The basic electrochemical reactions of PEMFC and AAEMFC is summarized as:

The electrochemical reactions of PEMFC (equations 1.10-1.12)[19]:

Anode:	$H_2 \rightarrow 2H^+ + 2e^-$	(electrode potential: 0.00 V)	(1.10)
Cathode:	$\frac{1}{2}O_2 + 2H^+ + 2e^- \rightarrow H_2O$	(electrode potential: 1.23 V)	(1.11)
Overall :	$H_2 + \frac{1}{2}O_2 \rightarrow H_2O$	(Overall potential: 1:23 V)	(1.12)

The electrochemical reactions of AAEMFC (equations 1.13-1.15) [54]:

Anode:	$H_2 + 2OH^- \rightarrow 2H_2O + 2e^-$	(electrode potential: -0.83 V)	(1.13)
Cathode:	$\frac{1}{2}O_2 + H_2O + 2e^- \rightarrow 2OH^-$	(electrode potential: 0.40 V)	(1.14)
Overall:	$H_2 + \frac{1}{2}O_2 \rightarrow H_2O$	(Overall potential: 1.23 V)	(1.15)

In H_2/O_2 fuel cell, the anodic HOR reaction is very fast and facile,[10] but the cathodic ORR reactions are several orders slower than the HOR reaction.[55] Currently, the platinum and their alloys are the best available electrocatalysts for anodic HOR and cathodic ORR reactions, providing faster kinetic rates in H_2/O_2 fuel cell.[55] However, due to sluggish kinetics of ORR reactions, a large content of expensive Pt is required at the cathode side of H_2/O_2 fuel cell, and therefore, limited its large-scale commercial application.[56-57] Besides the high cost, Pt suffers from several deficiencies, such as inadequate durability, dissolution during operation, poisoning, the decrease in active electrochemical surface areas and corrosion of the supported carbon.[58-60] To overcome these challenges and to make the H_2/O_2 fuel cell for commercial-scale applications, extensive experimental work is required on the synthesis and exploring of stable and efficient ORR electrocatalysts.

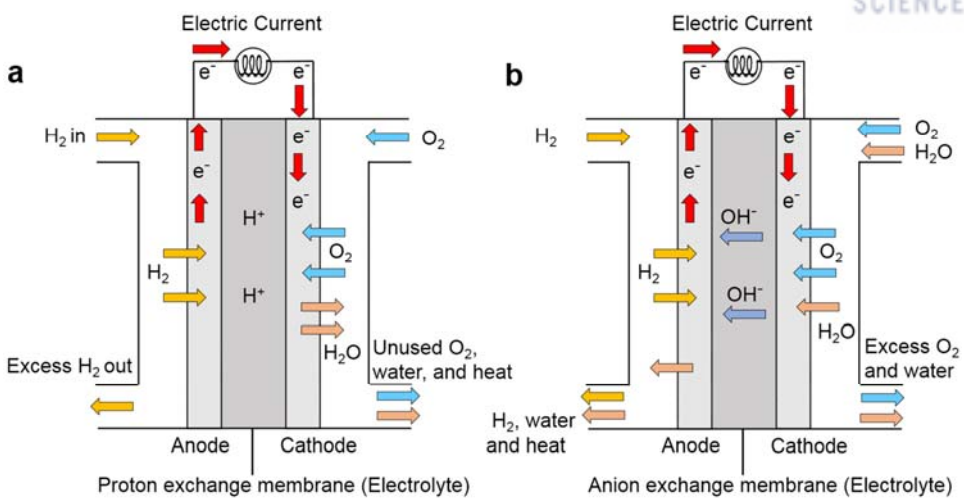

Figure 1.6. The Schematic presentation and working principle of **(a)** proton exchange membrane fuel cell and **(b)** alkaline anion exchange membrane fuel cell.

1.6. Basic mechanistic study of ORR

The cathodic ORR reactions in a fuel cell can occur either through a direct four-electron-proton pathway or through two-step/two-electron pathways depend on the electrode surface.[61-62] In four-electron pathway (can be either associative or dissociative in nature, depending on the energy barrier of oxygen molecules on the catalyst surface), the oxygen molecules are directly reducing to water molecules which is highly preferred in fuel cell for getting larger efficiency,[22] while in two-step/two-electron pathways, the oxygen molecules are first reduced to peroxide intermediate and then subsequently reduced to water molecules or chemically decompose to oxygen and water molecules.[63-64] The two-step/two-electron ORR reactions are attractive for the industrial-scale hydrogen peroxide production,[64] but not desirable in a fuel cell because the reduction of oxygen to water through peroxide intermediated leads to low conversion energy efficiency.[65] The detail ORR reaction mechanism in both acidic and basic solutions are summarized in equations 1.16 to 1.37.

The direct four-electron pathway in acidic solution (equation 1.16):[66]

$$O_2 + 4H^+ + 4e^- \rightarrow 2H_2O \qquad 1.16$$

The stepwise reaction of equation 1.16:

Dissociative:

$$O_2 + 2^* \rightarrow 2O^* \qquad 1.17$$

$$2O^* + 2H^+ + 2e^- \rightarrow 2OH^* \qquad 1.18$$

$$2OH^* + 2H^+ + 2e^- \rightarrow 2H_2O + 2^* \qquad 1.19$$

Associative

$$O_2 + * \rightarrow O_2^* \qquad 1.20$$

$$O_2^* + H^+ + e^- \rightarrow OOH^* \qquad 1.21$$

$$OOH^* + H^+ + e^- \rightarrow O^* + H_2O \qquad 1.22$$

$$O^* + H^+ + e^- \rightarrow OH^* \quad 1.23$$

$$OH^* + H^+ + e^- \rightarrow H_2O + * \quad 1.24$$

The direct four-electron pathway in basic solution (equation 1.25):[67]

$$O_2 + 2H_2O + 4e^- \rightarrow 4OH^- \quad 1.25$$

The stepwise reaction of equation 1.25:

Dissociative:

$$O_2 + 2^* \rightarrow 2O^* \quad 1.26$$

$$2O^* + 2e^- + 2H_2O \rightarrow 2OH^* + 2OH^- \quad 1.27$$

$$2OH^* + 2e^- \rightarrow 2OH^- + 2^* \quad 1.28$$

Associative

$$O_2 + * \rightarrow O_2^* \quad 1.29$$

$$O_2^* + H_2O + e^- \rightarrow OOH^* + OH^- \quad 1.30$$

$$OOH^* + e \rightarrow O^* + OH^- \quad 1.31$$

$$O^* + H_2O + e^- \rightarrow OH^* + OH^- \quad 1.32$$

$$OH^* + e^- \rightarrow OH^- + * \quad 1.33$$

The two-electron pathway in acidic solution (equation 1.34-1.35):[53]

$$O_2 + 2H^+ 2e^- \rightarrow H_2O_2 \quad 1.34$$

$$H_2O_2 + 2H^+ + 2e^- \rightarrow 2H_2O \quad 1.35$$

The two-electron pathway in basic solution (equation 1.36-1.37):[53]

$$O_2 + H_2O + 2e^- \rightarrow OOH^- + OH^- \quad 1.36$$

$$OOH^- + H_2O + 2e^- \rightarrow 3OH^- \quad 1.37$$

According to DFT calculation, the ORR activity of electrocatalyst is strongly related to its binding energies for the above oxygen intermediates.[33, 68-69] In order to get high ORR activity, the catalyst will bind the oxygen species tightly enough that can initiate the facile reduction reactions, but not too strong that the oxygen intermediates can completely block and poison the catalyst surface.[33, 68-69] For example, the electrocatalyst that binds the oxygen intermediates very strongly, the electrocatalytic activity is limited by electron-proton transfer to O* or OH*.[33, 68-69] In contrast, if the electrocatalyst binds the oxygen intermediates very weakly, the electrocatalytic activity is limited by electron-proton transfer to O_2* in associative mechanism and O-O splitting in a dissociative mechanism.[33, 68-69] Moreover, the ORR reaction pathways (direct four-electron-proton pathway, or two-step/two-electron pathway) also depends on oxygen dissociating energy barrier on the catalyst surface.[10, 70] Many DFT calculation has disclosed that the carbon-based material has very high energy barrier for oxygen dissociation and therefore, is not considered as a favorable surface for the four-electron-proton pathway.[10, 70] The reported experimental literature also shows that the ORR reactions on most of the carbon-and-silver-

based materials are proceeding through two-step/two-electron pathways.[10, 71] On the other hand, the metal-based electrocatalysts have low energy barrier for oxygen dissociation (e.g. oxygen dissociation on Pt (111) surface is smaller than 0.3 eV) and therefore is considered as a good surface for the dissociative four-electron-proton ORR reaction pathway,[10] which is consistent with the experimental observations.

Experimentally, two conventional methods such as the rotating ring-disk electrode measurement (RRD) and rotating ring-disk electrode measurement (RRDE) are usually used to calculate the electron transfer number (n) during the ORR reactions.

The "n" from RRD measurement can be calculated according to the following Koutecky-Levich equation (1.38-1.40):

$$\frac{1}{j} = \frac{1}{j_l} + \frac{1}{j_k} = \frac{1}{B\omega^{0.5}} + \frac{1}{j_k} \qquad 1.38$$

$$B = 0.64nFAC_0D_0^{2/3}n^{-1/6} \qquad 1.39$$

$$j_k = nFkC_d \qquad 1.40$$

where J is the measured current density, J_k and J_l are the kinetic and limiting current densities, ω is the rotation rate of electrode, F is the Faraday constant, A is the geometric area of the electrode, C_0 is the O_2 concentration, D_0 is the O_2 diffusion coefficient, V is the kinematic viscosity of the electrolyte, and k is rate constant.

From RRDE method, both "n" and percentage of peroxide (p) can be calculated according to the 1.41 and 1.42 equations:

$$n = 4 \times \frac{I_d}{I_d + I_r/N} \qquad 1.41$$

$$p = 200 \times \frac{I_r/N}{I_d + I_r/N} \qquad 1.42$$

where I_r and I_d are the ring and disk current, N is the current collection efficiency of the ring part of the electrode (Pt ring ~0.37).

1.7. Reference

1. Greeley, J.; Jaramillo, T. F.; Bonde, J.; Chorkendorff, I.; Nørskov, J. K., Computational high-throughput screening of electrocatalytic materials for hydrogen evolution. *Nat. Mater.* **2006,** *5*, 909.
2. Faber, M. S.; Jin, S., Earth-abundant inorganic electrocatalysts and their nanostructures for energy conversion applications. *Energy Environ. Sci.* **2014,** *7* (11), 3519-3542.
3. Liu, Y.; et al., Self-optimizing, highly surface-active layered metal dichalcogenide catalysts for hydrogen evolution. *Nat. Energy* **2017,** *2*, 17127.
4. Yagi, M.; Kaneko, M. Molecular Catalysts for Water Oxidation. *Chem. Rev.* **2001,** *101* (1), 21-36.
5. Cho, A., Energy's Tricky Tradeoffs. *Science* **2010,** *329* (5993), 786.
6. Aricò, A. S. et al., Nanostructured materials for advanced energy conversion and storage devices. *Nat. Mater.* **2005,** *4*, 366.
7. Steele, B. C. H.; Heinzel, A., Materials for fuel-cell technologies. *Nature* **2001,** *414*, 345.
8. Bruce, P. G.; Freunberger, S. A.; Hardwick, L. J.; Tarascon, J-M. Tarascon, J.-M., Li–O_2 and Li–S batteries with high energy storage. *Nat. Mater.* **2011,** *11*, 19.
9. Benson, E. E.; Kubiak, C. P.; Sathrum, A. J.; Smieja, J. M., Electrocatalytic and homogeneous approaches to conversion of CO2 to liquid fuels. *Chem. Soc. Rev.* **2009,** *38* (1), 89-99.
10. Jiao, Y.; Zheng, Y.; Jaroniec, M.; Qiao, S. Z., Design of electrocatalysts for oxygen- and hydrogen-involving energy conversion reactions. *Chem. Soc. Rev.* **2015,** *44* (8), 2060-2086.
11. Vij, V. at al., Nickel-Based Electrocatalysts for Energy-Related Applications: Oxygen Reduction, Oxygen Evolution, and Hydrogen Evolution Reactions. *ACS Catal.* **2017,** *7* (10), 7196-7225.
12. Nørskov, J. K.; et al., Trends in the Exchange Current for Hydrogen Evolution. *J. Electrochem. Soc.* **2005,** *152* (3), J23-J26.
13. Qiu, Y.; et al. BCC-Phased PdCu Alloy as a Highly Active Electrocatalyst for Hydrogen Oxidation in Alkaline Electrolytes. *J. Am. Chem. Soc.* **2018,** *140* (48), 16580-16588.
14. Kim, J. S.; Kim, B.; Kim, H.; Kang, K. Recent Progress on Multimetal Oxide Catalysts for the Oxygen Evolution Reaction. *Adv. Energy Mater.* **2018,** *8* (11), 1702774.
15. Danilovic, N.; et al., Activity–Stability Trends for the Oxygen Evolution Reaction on Monometallic Oxides in Acidic Environments. *J. Phys. Chem. Lett.* **2014,** *5* (14), 2474-2478.
16. Wang, J.; et al., Design of N-coordinated Dual-Metal Sites: A stable and active Pt-free catalyst for acidic oxygen reduction reaction. *J. Am. Chem. Soc.* **2017,** *139* (48), 17281-17284.
17. Liang, Y.; et al., Co_3O_4 nanocrystals on graphene as a synergistic catalyst for oxygen reduction reaction. *Nat. Mater.* **2011,** *10*, 780.
18. Wang, X.; et al., Constructing NiCo/Fe_3O_4 heteroparticles within MOF-74 for efficient oxygen evolution reactions. **2018,** *140* (45), 15336-15341.
19. Debe, M. K., Electrocatalyst approaches and challenges for automotive fuel cells. *Nature* **2012,** *486*, 43.
20. Su, X.; Wang, Y.; Zhou, J.; Gu, S.; Li, J.; Zhang, S., Operando spectroscopic identification of active sites in NiFe prussian blue analogues as electrocatalysts: activation of oxygen atoms for oxygen evolution reaction. *J. Am. Chem. Soc.* **2018,** *140* (36), 11286-11292.
21. Sultan, S.; et al., Single atoms and clusters based nanomaterials for hydrogen evolution, oxygen evolution reactions, and full water splitting. *Adv. Energy Mater.* **2019,** *9* (22), 1900624.
22. Sultan, S.; et al., Highly efficient oxygen reduction reaction activity of graphitic tube encapsulating nitrided Co_xFe_y alloy. *Adv. Energy Mater.* **2018,** *8* (25), 1801002.
23. Marković, N. M.; Schmidt, T. J., Oxygen reduction reaction on Pt and Pt bimetallic surfaces: a selective review. *Fuel Cells* **2001,** *1* (2), 105-116.
24. Antolini, E., Palladium in fuel cell catalysis. *Energy Environ. Sci.* **2009,** *2* (9), 915-931.
25. Antolini, E., Iridium as catalyst and cocatalyst for oxygen evolution/reduction in acidic polymer electrolyte membrane electrolyzers and fuel cells. *ACS Catal.* **2014,** *4* (5), 1426-1440.
26. Sultan, S.; et al., Superb water splitting activity of the electrocatalyst Fe3Co(PO4)4 designed with computation aid. *Nat. Commun.* **2019,** *10* (1), 5195.

27. Fang, M.; Dong, G.; Wei, R.; Ho, J. C., Hierarchical nanostructures: design for sustainable water splitting. *Adv. Energy Mater.* **2017,** *7* (23), 1700559.
28. Roger, I.; Shipman, M. A.; Symes, M. D., Earth-abundant catalysts for electrochemical and photoelectrochemical water splitting. *Nat. Rev. Chem.* **2017,** *1*, 0003.
29. Trasatti, S., Work function, electronegativity, and electrochemical behaviour of metals: III. electrolytic hydrogen evolution in acid solutions. *J. Electroanal. Chem. Interfacial Electrochem.* **1972,** *39* (1), 163-184.
30. Man, I. C.; et al., Universality in oxygen evolution electrocatalysis on oxide surfaces. *ChemCatChem* **2011,** *3* (7), 1159-1165.
31. Sheng, W.; Myint, M.; Chen, J. G.; Yan, Y., Correlating the hydrogen evolution reaction activity in alkaline electrolytes with the hydrogen binding energy on monometallic surfaces. *Energy Environ. Sci.* **2013,** *6* (5), 1509-1512.
32. Parsons, R. The rate of electrolytic hydrogen evolution and the heat of adsorption of hydrogen. *Trans. Faraday Soc.* **1958,** *54* (0), 1053-1063.
33. Seh, Z. W.; et al., Combining theory and experiment in electrocatalysis: Insights into materials design. *Science* **2017,** *355* (6321), eaad4998.
34. Zhang, J.; Zhao, Z.; Xia, Z.; Dai, L., A metal-free bifunctional electrocatalyst for oxygen reduction and oxygen evolution reactions. *Nat. Nanotechnol.* **2015,** *10*, 444.
35. Tiwari, J. N.; et al., Multicomponent electrocatalyst with ultralow Pt loading and high hydrogen evolution activity. *Nat. Energy* **2018,** *3* (9), 773-782.
36. Wang, J.; Xu, F.; Jin, H.; Chen, Y.; Wang, Y., Non-noble metal-based carbon composites in hydrogen evolution reaction:fundamentals to applications. *Adv. Mater.* **2017,** *29* (14), 1605838.
37. Yu, X.; et al., Hydrogen evolution reaction in alkaline media: alpha-or beta-nickel hydroxide on the surface of platinum. *ACS Energy Lett.* **2018,** *3* (1), 237-244.
38. Hunter, B. M.; Gray, H. B.; Müller, A. M., Earth-Abundant Heterogeneous Water Oxidation Catalysts. *Chem. Rev.* **2016,** *116* (22), 14120-14136.
39. Wannakao, S.; Maihom, T.; Kongpatpanich, K.; Limtrakul, J.; Promarak, V., Halogen substitutions leading to enhanced oxygen evolution and oxygen reduction reactions in metalloporphyrin frameworks. *Phys. Chem. Chem. Phys.* **2017,** *19* (43), 29540-29548.
40. Fabbri, E.; et. al., Developments and perspectives of oxide-based catalysts for the oxygen evolution reaction. *Catal. Sci. Technol.* **2014,** *4* (11), 3800-3821.
41. Jiao, K.; He, P.; Du, Q.; Yin, Y., Three-dimensional multiphase modeling of alkaline anion exchange membrane fuel cell. *Int. J. Hydrogen Energy* **2014,** *39* (11), 5981-5995.
42. An, L.; Zhao, T. S.; Shen, S. Y.; Wu, Q. X.; Chen, R., Alkaline direct oxidation fuel cell with non-platinum catalysts capable of converting glucose to electricity at high power output. *J. Power Sources* **2011,** *196* (1), 186-190.
43. Boudghene Stambouli, A., Fuel cells, an alternative to standard sources of energy. *Renew. Sustain. Energy Rev.* **2002,** *6* (3), 295-304.
44. Cullen, J. M.; Allwood, J. M., Theoretical efficiency limits for energy conversion devices. *Energy* **2010,** *35* (5), 2059-2069.
45. Pan, Z. F.; An, L.; Zhao, T. S.; Tang, Z. K., Advances and challenges in alkaline anion exchange membrane fuel cells. *Prog. Energy Combust. Sci.* **2018,** *66*, 141-175.
46. Pan, Z. F.; Chen, R.; An, L.; Li, Y. S., Alkaline anion exchange membrane fuel cells for cogeneration of electricity and valuable chemicals. *J. Power Sources* **2017,** *365*, 430-445.
47. Gopi, K. H.; Peera, S. G.; Bhat, S. D.; Sridhar, P.; Pitchumani, S., Preparation and characterization of quaternary ammonium functionalized poly(2,6-dimethyl-1,4-phenylene oxide) as anion exchange membrane for alkaline polymer electrolyte fuel cells. *Int. J. Hydrogen Energy* **2014,** *39* (6), 2659-2668.
48. Kirubakaran, A.; Jain, S.; Nema, R. K. A review on fuel cell technologies and power electronic interface. *Renew. Sustain. Energy Rev.* **2009,** *13* (9), 2430-2440.
49. Acres, G. J. K.; et al., Electrocatalysts for fuel cells. *Catal. Today* **1997,** *38* (4), 393-400.
50. Greeley, J. et al., Alloys of platinum and early transition metals as oxygen reduction electrocatalysts. *Nature Chemistry* **2009,** *1*, 552.

51. Stamenkovic, V. R.; et al., Improved oxygen reduction activity on $Pt_3Ni(111)$ via increased surface site availability. *Science* **2007,** *315* (5811), 493.
52. He, Q.; Cairns, E. J.; et al., Review-recent progress in electrocatalysts for oxygen reduction suitable for alkaline anion exchange membrane fuel cells. *J. Electrochem. Soc.* **2015,** *162* (14), F1504-F1539.
53. Varcoe, J. R.; et al., Anion-exchange membranes in electrochemical energy systems. *Energy Environ. Sci.* **2014,** *7* (10), 3135-3191.
54. Dekel, D. R., Review of cell performance in anion exchange membrane fuel cells. *J. Power Sources* **2018,** *375*, 158-169.
55. Sheng, W.; Gasteiger, H. A.; Shao-Horn, Y. J. Hydrogen oxidation and evolution reaction kinetics on platinum: acid vs alkaline electrolytes. *Electrochem. Soc.* **2010,** *157* (11), B1529-B1536.
56. Tiwari, J. N.; et. al., High-affinity-assisted nanoscale alloys as remarkable bifunctional catalyst for alcohol oxidation and oxygen reduction reactions. *ACS Nano* **2017,** *11* (8), 7729-7735.
57. Long, N. V.; et al., The development of mixture, alloy, and core-shell nanocatalysts with nanomaterial supports for energy conversion in low-temperature fuel cells. *Nano Energy* **2013,** *2* (5), 636-676.
58. Tong; Kim, H. S.; et al. An NMR Investigation of CO Tolerance in a Pt/Ru Fuel Cell Catalyst. *J. Am. Chem. Soc.* **2002,** *124* (3), 468-473.
59. Li, Q.; et al., High-Activity PtRuPd/C Catalyst for Direct Dimethyl Ether Fuel Cells. *Angew. Chem. Int. Ed* **2015,** *54* (26), 7524-7528.
60. Nie, Y.; Li, L.; Wei, Z., Recent advancements in Pt and Pt-free catalysts for oxygen reduction reaction. *Chem. Soc. Rev.* **2015,** *44* (8), 2168-2201.
61. Zhang, J.; Xia, Z.; Dai, L., Carbon-based electrocatalysts for advanced energy conversion and storage. *Science Advances* **2015,** *1* (7), e1500564.
62. Gong, K.; Du, F.; Xia, Z.; Durstock, M.; Dai, L., Nitrogen-doped carbon nanotube arrays with high electrocatalytic activity for oxygen reduction. *Science* **2009,** *323* (5915), 760.
63. Zhang, L.; Niu, J.; Dai, L.; Xia, Z., Effect of microstructure of nitrogen-doped graphene on oxygen reduction activity in fuel cells. *Langmuir* **2012,** *28* (19), 7542-7550.
64. Sánchez-Sánchez, C. M.; Bard, A. J., Hydrogen Peroxide Production in the Oxygen Reduction Reaction at Different Electrocatalysts as Quantified by Scanning Electrochemical Microscopy. *Analytical Chemistry* **2009,** *81* (19), 8094-8100.
65. Wang, B., Recent development of non-platinum catalysts for oxygen reduction reaction. *J. Power Sources* **2005,** *152*, 1-15.
66. Zhang, C.; et al., Single-atomic ruthenium catalytic sites on nitrogen-doped graphene for oxygen reduction reaction in acidic medium. *ACS Nano* **2017,** *11* (7), 6930-6941.
67. Nikitina, V. A.; et al., ORR on simple manganese oxides: molecular-level factors determining reaction mechanisms and electrocatalytic activity. *J. Electrochem. Soc.* **2018,** *165* (15), J3199-J3208.
68. Wang, R.; Chen, Z.; Hu, N.; Xu, C.; Shen, Z.; Liu, J., Nanocarbon-based electrocatalysts for rechargeable aqueous Li/Zn-air batteries. *ChemElectroChem* **2018,** *5* (14), 1745-1763.
69. Stacy, J.; Regmi, Y. N.; Leonard, B.; Fan, M., The recent progress and future of oxygen reduction reaction catalysis: A review. R*enew. Sustain. Energy Rev.* **2017,** *69*, 401-414.
70. Yu, L.; Pan, X.; Cao, X.; Hu, P.; Bao, X. Oxygen reduction reaction mechanism on nitrogen-doped graphene: A density functional theory study. *J. Catal.* **2011,** *282* (1), 183-190.
71. Alducin, M.; Busnengo, H. F.; Muiño, R. D., Dissociative dynamics of spin-triplet and spin-singlet O2 on Ag(100). *J. Chem. Phys.* **2008,** *129* (22), 224702.

Chapter 2

Superb water splitting activity of the electrocatalyst $Fe_3Co(PO_4)_4$ designed with computation-aid

2.1. Abstract

For efficient water splitting it is essential to develop inexpensive and super-efficient electrocatalysts for oxygen evolution reaction (OER). Herein, we report a phosphate-based electrocatalyst [$Fe_3Co(PO_4)_4$@reduced-graphene-oxide(rGO)] showing outstanding OER performance (much higher than state-of-the-art Ir/C catalyst), the design of which was aided by first-principles calculations. This electrocatalyst displays low overpotential (237 mV at high current density 100 mA cm^{-2} in 1M KOH), high turnover frequency (TOF: 0.54 s^{-1}), high Faradaic efficiency (98%) and long-term durability. The remarkable performance is ascribed to the optimal free energy for OER at Fe sites and efficient mass/charge-transfer. When a $Fe_3Co(PO_4)_4$@rGO anodic electrode is integrated with a Pt/C cathodic electrode, the electrolyzer requires only 1.45 V to achieve 10 mA cm^{-2} for whole-water-splitting in 1M KOH (1.39 V in 6M KOH) which is much smaller than commercial Ir-C//Pt-C electrocatalysts. This cost-effective powerful oxygen production material with carbon supporting-substrates offers a great promise for water splitting.

2.2. Introduction

The OER is a fundamental reaction in electrochemical energy conversion process which is the basis of water splitting, batteries and photoelectrochemical cells.[1-3] The water splitting is considered as a promising and renewable method for producing hydrogen and oxygen gases.[4-7] However, the efficiency of water splitting in basic electrolyte is largely hindered by sluggish kinetics of the oxidative half-cell OER reaction,[2, 7] and so commercial water splitting usually works at high voltage of 1.8−2.0 V.[8] Recently, noble metal-based compounds such as IrO_2 and RuO_2 exhibit good catalytic activities toward OER.[9-10] However, the widespread practical application of these noble metal-based compounds is restricted due to their skyrocketing price and scarcity.[5, 9] Therefore, development of cost-effective catalysts with high electrocatalytic activity and stability for OER is in high demand, which would lead to a cost-effective production of oxygen via water splitting. In this regard, inexpensive earth abundant transition metals based OER electrocatalysts would be a good choice not only because of their high abundance and low cost but also due to their high electrocatalytic activity and stability in wide pH ranges.[11-13]

Over the past decade, transition metal based OER electrocatalysts (for instance cobalt phosphate, surface oxidized steels, NiFe layered-double-hydroxide, oxy-hydroxides, oxide, perovskites, cobalt phosphate composites, and Co_3O_4 etc.) have been explored due to their high potential for water oxidation, high durability under basic condition and their benign environmental nature.[5, 7-9, 12-14]

Nevertheless, these materials exhibit large overpotential (η) for OER.[5, 7-9] Therefore, effective designing of state-of-the-art electrocatalyst and clear understanding of OER catalytic mechanism remain challenging tasks.

Herein, we report a phosphate-based electrocatalyst of $Fe_3Co(PO_4)_4$/rGO (**1**) for OER, which is predicted to be highly active by density functional theory (DFT). The as synthesized **1** indeed serves as a highly active electrocatalyst for OER in basic media with overpotential of ~237 mV at 100 mA cm^{-2} and long-term durability (5000 cycles). On the basis of theoretical modelling and experimental observations, the high OER activity of the designed electrocatalyst is ascribed to the PO_4-induced positive shift of the redox potential. The efficient mass and charge transfer due to defects/dislocations in the PO_4-induced mix-phase as well as large Brunauer-Emmett-Teller (BET) surface area also help in the OER activity. When it was integrated into asymmetric two-electrode water-splitting cells, the electrolyzer required a potential ~1.45 V in 1M KOH (or ~1.39 V in 6M KOH) to drive a current density of 10 mA cm^{-2} for whole water splitting, which is much smaller than that of the integrated commercial Ir-C//Pt-C electrocatalysts (~1.53 V in 1M KOH).

2.3. Experimental Section

2.3.1. Chemicals

Cobalt(II) perchlorate hexahydrate, iron (III) chloride (reagent grade, 97%), red phosphorus (reagent grade, 99.99%) and 5 wt% of Nafion, perchloric acid were purchased from Sigma-Aldrich. Benchmark 20 wt% Ir/C (commercial) and 20 wt% Pt/C (commercial) catalysts were purchased from Johnson Matthey and Premetek Co. All the chemicals were of analytical grade and used as received without further purification.

2.3.2. Synthetic procedure

In synthesis, 200 mg of graphene oxide (GO) and 70 mg of red phosphorus with different weight ratios of iron chloride ($FeCl_3$) to cobalt perchlorate hexahydrate $Co(ClO_4)_2.6H_2O$ were used as starting materials. During the synthesis process, 200 mg of GO was dispersed in 100 mL double distilled water by sonication. The precursors' weight ratios were chosen as 0.70 g $FeCl_3$, 0.35g $Co(ClO_4)_2.6H_2O$ and 0.07g red phosphorus for **1** [**1**: $Fe_3Co(PO_4)_4$@rGO], 0.6 g $FeCl_3$, 0.45 g $Co(ClO_4)_2.6H_2O$ and 0.07g red phosphorus for **2** [**2**: $Fe_{1-1.33}Co(PO_4)_2$@rGO or $FeCo(PO_4)_2$@rGO], and 0.65 g $FeCl_3$, 0.4g $Co(ClO_4)_2.6H_2O$ and 0.07g red phosphorus for **3** [**3**: $Fe_{1.5-2}Co(PO_4)_4$@rGO or $Fe_2Co(PO_4)_4$@rGO]. The resulting solutions were sonicated for 10h to obtain fine homogeneous mixture. The mixture was then dried and thoroughly ground. The ground powder was annealed at 750°C for 3 h with a temperature ramping rate of 3°C/min in nitrogen atmosphere. To remove the inactive species, the obtained product was leached with 0.1M $HClO_4$ for 10 h, then filtered and washed with ethanol and water, and finally dried in vacuum at 60°C. The atomic and weight percent of metals and non-metals in catalysts **1-3** obtained with inductively-coupled-plasma atomic-emission-spectroscopy (ICP-AES) and X-ray photoelectron spectroscopy (XPS) are shown in table 2.1 and 2.2. For the synthesis of **4** and **5**

(**4**: $Fe_2P_2O_7$@rGO, **5**: ($CoFe_2O_4$)(Fe_2O_3)@rGO), the same method was employed using 0.70 g $FeCl_3$ and 0.07 mg red phosphorus for **4**, and 0.70 g $FeCl_3$ and 0.35g $Co(ClO_4)_2.6H_2O$ for **5**. To study the effect of GO and red phosphorous on the OER performance, we have synthesized catalysts with different amount of GO and red phosphorous such as: **6** [**6**: 0.7 g $FeCl_3$, 0.35 g $Co(ClO_4)_2.6H_2O$, 100 mg GO and 0.07g red phosphorus], **7** [**7**: 0.7 g $FeCl_3$, 0.35 g $Co(ClO_4)_2.6H_2O$, 300 mg GO and 0.07g red phosphorus], **8** [**8**: 0.7 g $FeCl_3$, 0.35 g $Co(ClO_4)_2.6H_2O$, 200 mg GO and 0.035g red phosphorus] and **9** [**9**: 0.7 g $FeCl_3$, 0.35 g $Co(ClO_4)_2.6H_2O$, 200 mg GO and 0.140 g red phosphorus]. The C and P contents obtained from XPS analysis in catalysts **6-9** are shown in table 2.3.

2.3.3. Characterization techniques

The cold field emission SEM (FESEM) images were taken using Hitachi High-Technologies S-4800 microscope. TEM and HRTEM images and HAADF-STEM images were taken on JEM-2100F with 200 kV acceleration voltage. XPS data were carried out on K-alpha (Thermo Fisher, UK) system. The surface area, pore size distribution, and pore volume with N_2 adsorption/desorption isotherms from BET technique were measured on BELSORP-miniII (BEL Japan, Inc.) system. The atomic and weight percent of metals and non-metals in each synthesized catalyst were obtained with ICP-AES (700-ES, Varian) and XPS. EXAFS analysis was performed on ionization detectors at the Pohang Accelerator Laboratory (PAL). The X-ray absorption spectra for the Fe K-edge and Co K-edge were acquired at room temperature using beamlines 6D and 10C (PAL), where their X-ray energies from EXAFS analysis were calibrated with Fe-foil and Co-foil, respectively. Background subtraction, normalization and FT were done by standard procedure with ATHENA program.[15] The extracted EXAFS signal, $\chi(r)$ and $k^3\chi(k)$ were analyzed for all three metals. The Artemis program was used for EXAFS fitting. Soft XAS measurements were performed at the soft X-ray 10D XAS KIST beamline operating at 3.0 GeV with a maximum storage current of 360 mA. XAS spectra for Fe and Co $L_{3,2}$-edge were collected in the total electron yield mode at room temperature in vacuum of $\sim 1.5\times10^{-8}$ Torr. All the spectra were background subtracted and normalized with respect to the incident photon flux measured by inserting a gold (Au) mesh in the path of the X-ray beam.

Table 2.1. ICP-AES Chemical composition analysis: ICP-AES analysis gives the atomic percentage of bulk sample. The analysis of C and O is not possible through ICP-AES, while the content of P tends to be underestimated compared with metals. Thus, only contents of Co and Fe are investigated here. Among four different samples, two mid-value data are reported, and the Fe/Co compositions of catalysts **1-3** are roughly determined. Copyright 2019, Springer Nature.

Catalysts	Co (g/kg)	Fe (g/kg)	Co:Fe [at. ratio]	Composition
1	81.0	233	1: 3.0	$CoFe_3$
	66.5	197	1: 3.1	$CoFe_3$
2	129	130	1: 1.1	CoFe
	114	136	1: 1.3	~ Co_3Fe_4
3	91.0	128	1: 1.5	Co_2Fe_3
	83.0	144	1: 1.8	~ $CoFe_2$

Table 2.2. XPS Chemical composition analysis: XPS analysis provides the atomic percentage near sample surface. As compared with ICP-AES bulk sample analysis, the XPS surface analysis increases the $Fe(PO_4)$ content, while the atomic content of P (or PO_4) is almost the sum of Co and Fe atomic contents, indicating the charges of Co and Fe are +3. The content of O is slightly larger than 4 times of the content of P due to environmental oxygen. An extra content of $Fe(PO_4)$, as noted from XPS over ICP-AES could be present on the surface more than in bulk. However, the XPS data are not so reliable for accurate composition analysis as compared with ICP-AES. The Fe/Co metals composition ratio from ICP-AES is more reliable. Copyright 2019, Springer Nature.

Catalysts	Co	Fe	P	O	C	Co:Fe:P:O	Composition
1	1.07	4.02	4.86	21.31	68.73	1: 3.8: 4.5: 19.9	$CoFe_3(PO_4)_4$+$Fe(PO_4)$
2	1.09	2.32	3.80	20.06	70.99	1: 2.1: 3.5: 18.4	$CoFe(PO_4)_2$+$Fe(PO_4)$
3	0.94	2.95	4.37	18.91	72.48	1: 3.1: 4.6: 20.1	$CoFe_2(PO_4)_3$+$Fe(PO_4)$

Table 2.3. XPS Chemical composition analysis of catalysts 6-9: The atomic content of C and P obtained from XPS analysis in Catalysts **6-9**. Copyright 2019, Springer Nature.

Catalysts	6	7	8	9
C	53.04	82.28	76.23	67.14
P	4.59	2.96	2.56	6.09

2.3.4. Electrochemical characterization

All electrochemical measurements were performed on VSP instrument (BioLogic Science instruments, Inc.) with three-electrode setup using graphite rod and Hg/HgO as a counter and reference electrodes, respectively. The working electrodes in our experiment were glassy carbon electrode (GCE; 0.0706 cm^2) and NF with a geometric area of 3 cm^2. For working electrode preparation, 1 mg cm^{-2} loading amount of the catalyst was achieved through a drop casting method. To ensure the H_2O/O_2 equilibrium during the electrochemical measurement for OER, the electrolyte (1M KOH) was saturated with a continuous flow of oxygen for 20 min. For stabilizing the working electrodes, the cyclic voltammograms (CVs) were first conducted at a sweep rate of 100 mV s^{-1} in the potential range of 1.1 to 1.7 V versus reversible hydrogen electrode (RHE). The linear sweep voltammograms (LSVs) test were performed at a scan rate of 5 mV s^{-1} with 100% iR-compensation, which was automatically derived from the electrochemical workstation. The cycling durability test was carried out at a scan rate of 100 mV s^{-1} for 5000 CV cycles in the potential range of 1.2 to 1.6 V versus RHE. Chronoamperometry (CA) responses were performed on both GC (for 55 h) and NF (for 70 h) substrates at potentials on which the current densities reached to the range of 10 mA cm^{-2}. To evaluate the durability of **1** for high current density generation, the CA response were performed on NF substrate at a current density of ~210 mA cm^{-2} for 45 h. All the CA response were performed without iR-compensation. Polarization curves obtained before and after the durability CV cycles were collected for comparison. The current density (mA cm^{-2}) was normalized to the electrode geometrical area and the potentials recorded vs. Hg/HgO (1M NaOH) were converted to RHE according to the reference electrode calibration value (Figure 2.1). For double layer capacitance (C_{dl}) measurements, the potential in a non-Faradic region (1.059 to 1.174 V versus RHE) were cycled at a different applied scan rate of 10, 20, 30, 40, and 50 mV s^{-1}. The current from CV curves was plotted versus applied scan rate at a potential of 1.125 V and the slope obtained from the straight line of current and scan rate were assigned to C_{dl}. The EIS was performed at an overpotential of 0.30 V versus RHE in a frequency range of 100 kHz to 0.01Hz with a modulation amplitude of 10 mV in 1M KOH solution. The full water splitting was measured in a two-electrode setup with **1** as an OER electrode and Pt/C as a HER catalyst in 1M KOH (the catalyst loading was 1.5 mg cm^{-2}) and 6M KOH (the catalyst loading was 5 mg cm^{-2}) solutions.

The Tafel plots and slopes were calculated according to the equation (2.1):

$$\eta = b \log j + C \qquad (2.1)$$

where η, j, b, and C represent overpotential, current density, Tafel slope, and intercept, respectively.

The overpotential was calculated according to the equation (2.2):

$$\eta = E(\text{vs. RHE}) - 1.23 \qquad (2.2)$$

TOF of catalyst: The number of oxygen turnovers was calculated from the current density using the equation (2.3): [16]

$$\text{TOF} = \frac{\text{Total number of } O_2 \text{ turnovers/geometric area } (\text{cm}^2)}{\text{Number of active sites/geometric area } (\text{cm}^2)} \qquad (2.3)$$

$$\text{Number of } O_2 \text{ turnovers} = \left(\text{j}\frac{\text{mA}}{\text{cm}^2}\right)\left(\frac{1\frac{\text{C}}{\text{s}}}{1000\ \text{mA}}\right)\left(\frac{1\ \text{mol e}^-}{96485\ \text{C}}\right)\left(\frac{1\ \text{mol O}_2}{4\ \text{mol e}^-}\right)\left(\frac{6.022\times10^{23}\ \text{mol O}_2}{1\ \text{mol O}_2}\right)$$

$$= 1.56 \times 10^{15}\left(\frac{O_2/\text{s}}{\text{cm}^2}\right)\ \text{per}\ \left(\frac{\text{mA}}{\text{cm}^2}\right)$$

The number of Fe and Co ions in **1** was obtained from the ICP analysis ~28.9 wt.%. Consequently, the density of active sites based on bulk Fe and Co is:

$$\left(\frac{28.9\ \text{mg}}{100\ \text{mg}}\right) \text{x} \left(\frac{1\ \text{mg}}{\text{cm}^2}\right) \text{x} \left(\frac{1\ \text{mmole}}{606.35\text{mg}}\right) \text{x}\ 6.022\ \text{x}\ 10^{20}\left(\frac{\text{sites}}{\text{mmole}}\right) = 2.87\ \text{x}\ 10^{17}\ \text{sites/cm}^2$$

The TOF of the catalyst at an overpotential of 237 mV (current density 100 mA cm^{-2}) was calculated as:

$$\frac{1.56\ \text{x}\ 10^{15}\left(\frac{O_2/\text{s}}{\text{cm}^2}\right)\ \text{per}\left(\frac{\text{mA}}{\text{cm}^2}\right) \text{x}\ 100\left(\frac{\text{mA}}{\text{cm}^2}\right)}{2.87\ \text{x}\ 10^{17}\ \text{sites/cm}^2} = 0.54/\text{site}\ \text{s}^{-1}$$

Faradaic efficiency: Faradaic efficiency was calculated using the equation (2.4):

$$\text{Faradaic efficiency} = \frac{\text{experimental } \mu\text{mol of } O_2 \text{ gas}}{\text{theoretical } \mu\text{mol of } O_2\text{gas}} \times 100 \qquad (2.4)$$

The theoretical amount of O_2 gas was calculated from Faraday's law equation (2.5):

$$\text{n} = \frac{\text{I} \times \text{t}}{\text{z} \times \text{F}} \qquad (2.5)$$

where n is the number of mol, I is the current in ampere, t is the time in seconds, z is the transfer of electrons (for O_2 z = 4), and F is the Faraday constant (96485 C mol^{-1}).

The theoretical amount of O_2 gas before stability = 19.52 µmol

The theoretical amount of O_2 gas after stability = 19.00 µmol.

The experimental amount of O_2 gas was evaluated from the water displacement method using the following protocol:

In our calculations the pressure is converted into units of an atmosphere by Dalton's law of partial pressure equations (2.6):

$$P_{\text{Total}} = P_{\text{oxygen}} + P_{\text{water}} \qquad (2.6)$$

At ambient conditions, the vapor pressure of water is 21.1 mmHg (this valve was chosen from vapor pressure table).

$$762\ \text{mmHg} = P_{\text{oxygen}} + 21.1\ \text{mmHg}$$

$$P_{\text{oxygen}} = 762\ \text{mmHg} - 21.1\ \text{mmHg}$$

$$P_{oxygen} = 740.9\ mmHg$$

The pressure in our calculations with respect to one atmosphere was:

$$(740.9\ \text{mmHg})(1\ \text{atm}/760\ \text{mmHg}) = 0.975\ \text{atm}$$

Finally, the number of mol oxygen gas produced in water displacement is calculated by the equation (2.7):

$$PV = nRT \qquad (2.7)$$

V is the volume of produced gas in liters, T is the temperature in kelvin, and R is the ideal gas constant (0.0821 L atm/mol K).

The number of moles oxygen gas produced in water displacement before the stability:

$$(0.975\ \text{atm})\ (0.00048\text{L}) = n\ (0.0821\ \text{L atm/mol K})\ (298\text{K})$$

$$n = \frac{(0.975\ \text{atm}) \times (0.00048\ \text{L})}{(0.0821\ \text{L atm/mole K}) \times (298\text{K})}$$

$$n = 19.1\ \mu\ \text{mol}$$

The number of mol oxygen gas produced in water displacement after the stability:

$$(0.975\ \text{atm})\ (0.00046\text{L}) = n\ (0.0821\ \text{L atm/mole K})\ (298\text{K})$$

$$n = \frac{(0.975\ \text{atm}) \times (0.00046\text{L})}{(0.0821\ \text{L atm/mole K}) \times (298\text{K})}$$

$$n = 18.3\ \mu\ \text{mol}$$

Faradaic efficiency before stability.

$$\text{Faradaic efficiency} = \frac{19.10}{19.52} * 100$$

Faradaic efficiency after stability.

$$\text{Faradaic efficiency} = \frac{18.30}{19.00} * 100$$

The Faradaic efficiency before stability was 98%, while it was 96% after the 54 h of chronoamperometric stability test.

2.3.5. Calibration of reference electrode

Reference electrode calibration was carried in a three electrode system with Pt foil as working and counter electrode and Hg/HgO (1M NaOH) as reference electrode. The calibration was performed in high purity hydrogen saturated 1M KOH electrolyte. Steady-state linear-sweep voltammetry (LSV) was run at a scan rate of 0.5 mV s^{-1} and the potential at which current crosses zero was taken as thermodynamic potential (vs. Hg/HgO) for the hydrogen electrode (Figure 2.1).

The potential at which current crosses zero is -0.915 V vs Hg/HgO. Thus, in this study the potential of Hg/HgO vs reversible hydrogen electrode is 0.915 V.

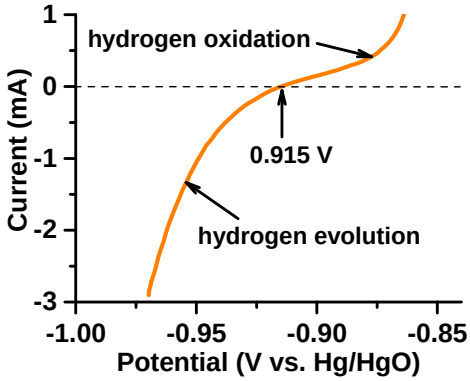

Figure 2.1. Calibration of reference electrode. Calibration curve for Hg/HgO electrode in 1M KOH. Copyright 2019, Springer Nature.

2.4. Results and Discussion

2.4.1. Theoretical Model

Inexpensive Fe and Co hybrids with inorganic species (such as P or O) can show good OER performance [17-19] in that the covalent strength of Fe/Co-X in a Fe/Co-X-Y linkage is controlled by the inductive effect.[18] Positive shift of the redox potential for transition metal oxide catalysts can lead to high catalytic effect.[20] In consideration of the inductive effect, we have considered various phosphorus oxides P_xO_y as a better alternative for P/O. Given that O is highly electronegative, substituting O with phosphate would be a good choice for OER. Thus, tuning the catalytic effect would be possible by substituting O with phosphate, and further fine-turning, by optimizing the Fe/Co ratio. In many cases, Fe and Co behave similarly with similar ionization potentials E_{IP}(Fe/Co) = 7.87/7.86 eV, but they show a large difference in valence electron configurations $[Ar]3d^64s^2/[Ar]3d^74s^2$ and electron affinities E_{EA}(Fe/Co) = 0.15/0.66 eV. Therefore, their cations with varying Fe/Co ratio give different electrochemical properties with different induction effects. This led us to theoretically investigate the OER performance of stable cage structures of $Fe_mCo_{8-m}O_{12}$ (m=0,2,4,6,8) and $Fe_nCo_{4-n}(PO_4)_4$ (n=0-4) (Figure 2.2a) at varying compositions of Fe and Co (a few varying Fe/Co ratios of 4/0, 3/1, 2/2, 1/3, 0/4). DFT calculations were performed to understand their electronic structure (Figures 2.3-2.5) and *O/*OH free energies ($\Delta G_O/\Delta G_{OH}$) and theoretical overpotentials (η^{theory}) required for OER at various compositions (Table 2.4), where * denotes an active site. We found that the metal substrate of rGO, though significantly beneficial for durability and conductivity (Figure 2.6), does not give significant effects on electronic structures of $Fe_nCo_{4-n}(PO_4)_4$ (n=0-4). To study the catalytic effect, here we have focused on the most stable (010) surface of $Fe_nCo_{4-n}(PO_4)_4$ (Table 2.5) rather than $Fe_nCo_{4-n}(PO_4)_4$@rGO for the realistic model.

The optimal catalytic activity is found from the Fe/Co ratio of 3 for the $Fe_nCo_{4-n}(PO_4)_4$ models of clusters and (010) surfaces. For Fe/Co mixed metal phosphates, the η^{theory} at Fe sites is the smallest at n=3, i.e., $Fe_3Co(PO_4)_4$, while the η^{theory} of Co sites is not small, remaining almost same for n=0-4 (Table

2.4). In the $Fe_mCo_{8-m}O_{12}$ (m=0,2,4,6,8) model, the substitution effect of Co for Fe improves the η^{theory} at Fe sites but not at Co sites. Thus, in both models, a small amount of Co which substitutes Fe is effective on Fe sites but not so on Co sites, and the optimized Fe/Co ratio at Fe sites in $Fe_nCo_{4-n}(PO_4)_4$ is 3. The binding energies of intermediate states at Fe sites become weaker if they are surrounded by many Co atoms. As a result, those local Fe sites become less active. The Fe sites of $Fe_3Co(PO_4)_4$ are predicted to show excellent activity with η^{theory}=0.24 V. The Fe and Co sites are tri-coordinated in clusters and penta-coordinated in (010) surfaces. The binding energies of intermediate states become weaker on the penta-coordinated Fe sites constantly (by ~0.5 eV) than on the tri-coordinated Fe sites. Yet, their free energy changes between O-adsorption and OH-adsorption (ΔG_O-ΔG_{OH}) behave similarly except for this constant difference and so their overpotentials are similar in both models. It seems that the binding energies of all the intermediate states also become weaker at more coordinated sites on surfaces by almost same magnitude (~0.5 eV) than on clusters.

To sum-up, the electronic structure calculations reveal that the phosphate and the Fe/Co ratio (optimal value of 3/1) are important in tuning the redox potential. As compared to Fe_3CoO_6 (0001), the phosphate group in $Fe_3Co(PO_4)_4$ (010) lowers the metal oxide antibonding state and positively shifts the redox potential with the inductive effect (Figure 2.3). Since Co (which is slightly more electronegative than Fe) pulls down the metal oxide antibonding state energy levels and thereby positively shifts the redox potential (Figure 2.3), tuning the Fe/Co ratio can be exploited for better OER performance.

DFT calculations show that **1** exhibits the optimal ΔG_O-ΔG_{OH} free energy (Figure 2.2a). At the O-adsorbed metal sites of **1**, the bond strength between Fe/Co 3*d* and O 2*p* orbitals becomes weaker than at those of $Fe_6Co_2O_{12}$ (Figure 2.4). Thus, we investigate the energetics of all intermediates (OH, O, OOH adsorption) and evaluate the theoretical overpotentials for OER (η^{theory}) of catalysts of $FeCo_3(PO_4)_4$ (010) and clusters of $Fe_3Co(PO_4)_4$, $FeCo_3(PO_4)_4$, $Fe_6Co_2O_{12}$ and $Fe_2Co_6O_{12}$ (Figure 2.2). Iron-cobalt oxide clusters are also studied to understand their ratio effect on catalytic activity. We calculate η^{theory} for the $FeCo_3(PO_4)_4$ cluster and $FeCo_3(PO_4)_4$ (010) surface models and other cases with different Fe/Co ratios. The η^{theory} at Co site of $FeCo_3(PO_4)_4$ (010) is 0.49 V which is larger than the η^{theory} 0.24 V at Fe site of $Fe_3Co(PO_4)_4$. The Fe site in the $Fe_3Co(PO_4)_4$ (010) has a lower ΔG_2 value (1.47 V) than that of the Co site (1.76 V). The improvement in η^{theory} at the Fe-site in **1** over other considered composites is attributed to optimal ΔG_O-ΔG_{OH} by weakend *O binding and *OH binding at the Fe site, while the same change of *O and *OH binding at Co sites affect the OER reaction only moderately (Figure 2.2b, c, Figure 2.5 and Table 2.4). Overall, our computation shows that 1 reduces the energy barriers for every step, thereby lowering the free energies of each elementary reaction step (Figure 2.2b, c & Table 2.4).

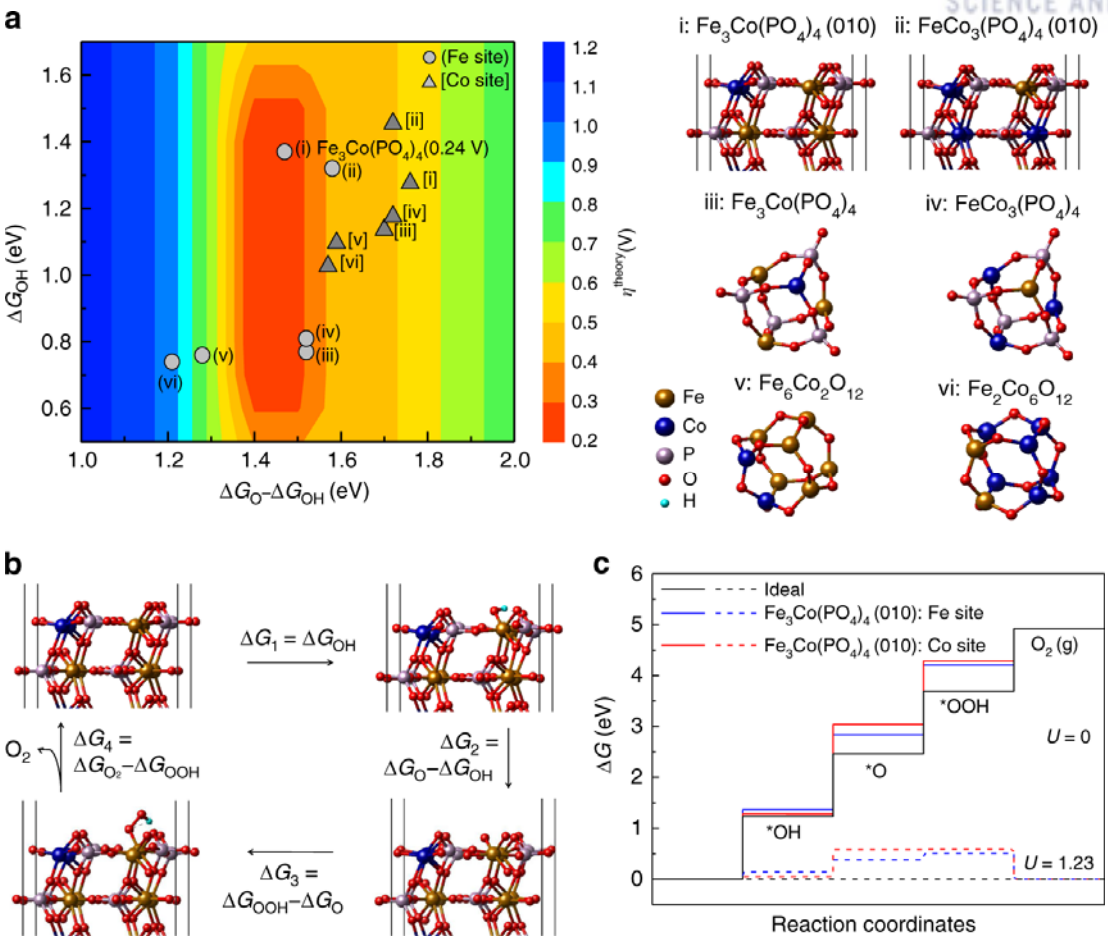

Figure 2.2. DFT-predicted structures, overpotentials, and free energy profiles. **(a)** 2D color-coded map of theoretical overpotential η^{theory} as function of free energies ΔG_O-ΔG_{OH} and ΔG_{OH} for various compositions (**i**: $Fe_3Co(PO_4)_4$ (010), **ii:** $FeCo_3(PO_4)_4$ (010), **iii**: $Fe_3Co(PO_4)_4$ cluster, **iv**: $FeCo_3(PO_4)_4$ cluster, **v**: $Fe_6Co_2O_{12}$ cluster, **vi**: $Fe_2Co_6O_{12}$ cluster) at Fe (gray circle) and Co (dark gray triangle) active sites. **(b)** Optimized geometries of the *O, *OH, and *OOH intermediates on the Fe sites of $Fe_3Co(PO_4)_4$ (010) (Table 2.4). **(c)** Free energy profiles of OER at zero and equilibrium (1.23 V) potentials for Fe and Co sites of $Fe_3Co(PO_4)_4$ (010). OER typically undergoes a four-electron step process in alkali media. In an ideal case, the free energy changes by 1.23 V at each step (black line). The conversion of *OH to *O is the rate-determining step on both Fe site (ΔG_1=0.24 V) and Co site (ΔG_2=0.53 V). Copyright 2019, Springer Nature.

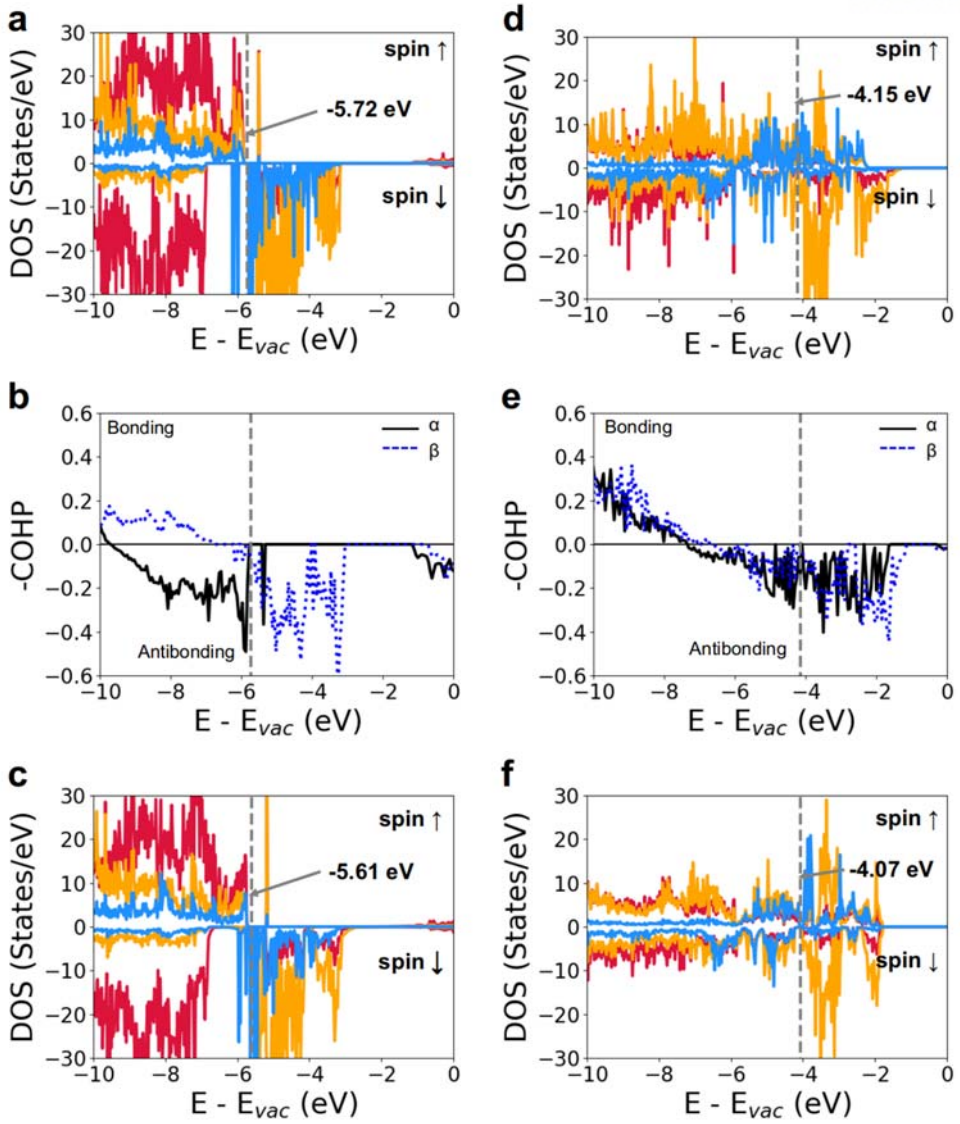

Figure 2.3. Electronic structures of $Fe_3Co(PO_4)_4$ (010) and Fe_3CoO_6 (0001). **(a, d)** Partial density of states (PDOS) and (b, e) crystal orbital Hamilton population (COHP) of M-O (M=Fe, Co) bonds in $Fe_3Co(PO_4)_4$ (010) (a, b) and Fe_3CoO_6 (0001) (d, e) with respect to energy (versus vacuum), which clearly demonstrate the effect of phosphate substitution. Because of the stabilization of M-O antibonding states, there exists a pronounced energy downshift of $Fe_3Co(PO_4)_4$(010) as compared to Fe_3CoO_6(0001). The effect of reduced graphene oxide (rGO) on electronic properties of both surfaces is small based on similar PDOS of (c) $Fe_3Co(PO_4)_4$(010)/rGO and (f) Fe_3CoO_6(0001)/rGO with PDOS of **(a)** and **(d)**, respectively. Fe: orange, Co: sky-blue, O: red. Copyright 2019, Springer Nature.

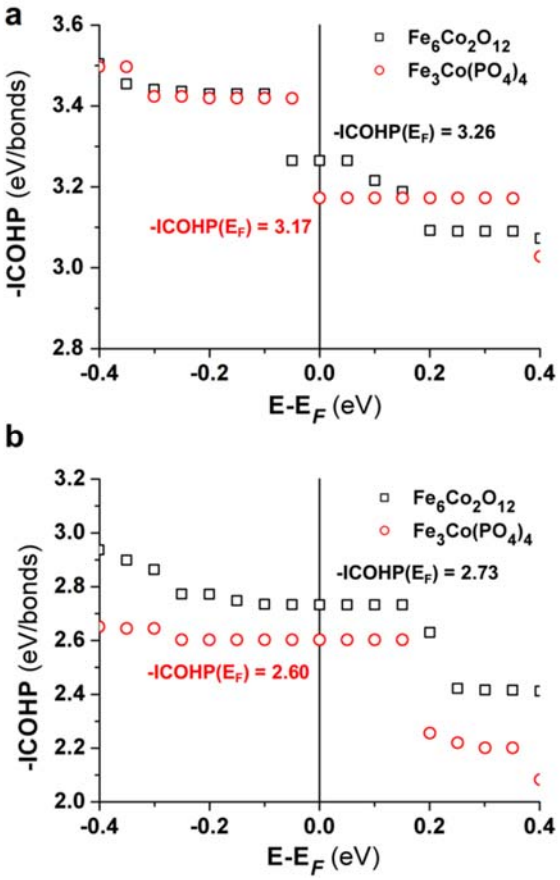

Figure 2.4. Integrated crystal orbital Hamilton population (ICOHP) of $Fe_3Co(PO_4)_4$ and $Fe_6Co_2O_{12}$ for **(a)** Fe-*O and **(b)** Co-*O. The ICOHP up to Fermi energy (ICOHP(E_F)) is related to bond strength (More positive -ICOHP implies stronger bond). In both Fe and Co sites, M-O (M=Fe, Co) of $Fe_3Co(PO_4)_4$ is weaker than that of $Fe_6Co_2O_{12}$. Copyright 2019, Springer Nature.

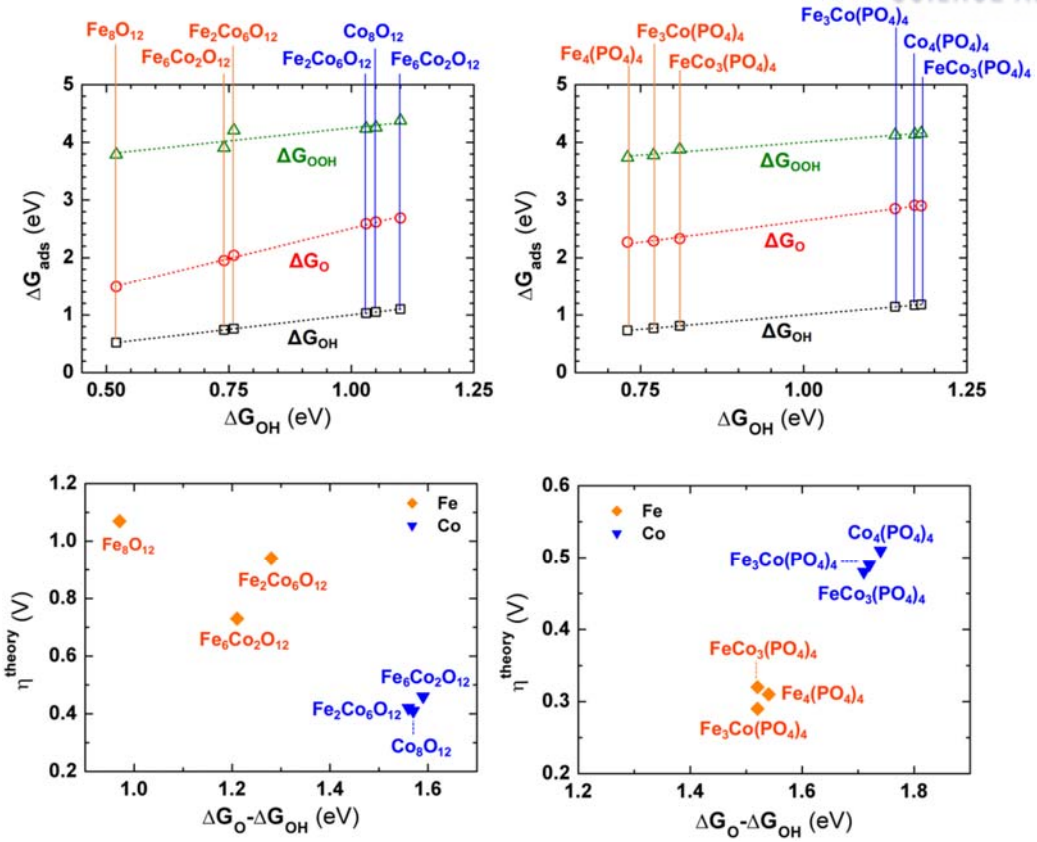

Figure 2.5. Adsorption free energies for OER intermediates versus ΔG_{OH} and theoretical overpotential (η^{theory}) versus ΔG_O-ΔG_{OH}. Adsorption Free energies of *O, *OH and *OOH (ΔG_O, ΔG_{OH} and ΔG_{OOH}, respectively) and η^{theory} at Fe-sites (orange) and Co-sites (blue) of Fe_8O_{12}, $Fe_6Co_2O_{12}$, $Fe_2Co_6O_{12}$, Co_8O_{12}, $Fe_4(PO_4)_4$, $Fe_3Co(PO_4)_4$, $FeCo_3(PO_4)_4$, and $Co_4(PO_4)_4$ clusters are plotted as a function of ΔG_{OH} and ΔG_O-ΔG_{OH}, respectively. Copyright 2019, Springer Nature.

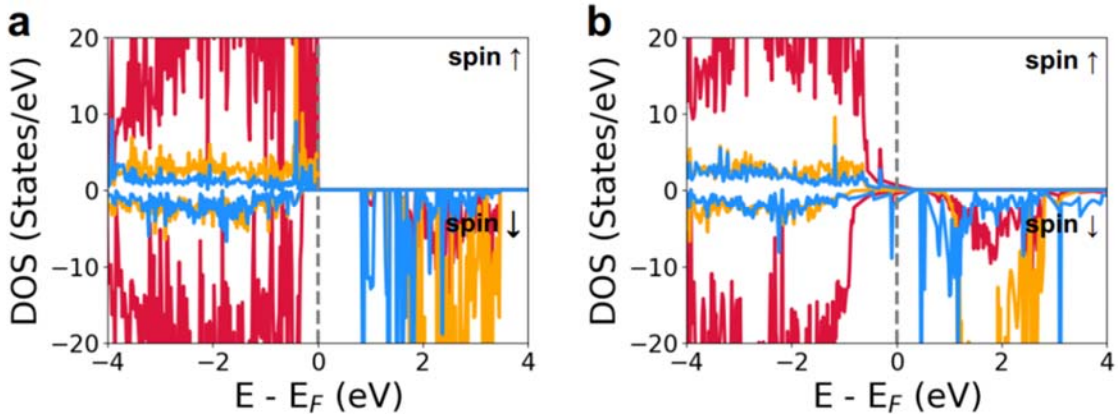

Figure 2.6. Partial density of states (PDOS) of **(a)** $Fe_3Co(PO_4)_4(010)$ and **(b)** $Fe_3Co_3(PO_4)_4(010)$/rGO using PBE+U (U_{eff} (Fe) = 4 eV, U_{eff} (Co) = 3.3 eV). The rGO support makes metal phosphates conductive. Fe: orange, Co: skyblue, O: red. Copyright 2019, Springer Nature.

Table 2.4. DFT-predicted Gibbs free energies for OER steps (intermediate states) and overpotential (η^{theory}) at Fe and Co sites of various composites (see the scheme in computational method). Copyright 2019, Springer Nature.

Materials (Site)	ΔG_1 (eV) (ΔG_{OH})	ΔG_2 (eV) (ΔG_O)	ΔG_3 (eV) (ΔG_{OOH})	ΔG_4 (eV)	η^{theory} (V)
$Fe_4(PO_4)_4$ (010) (Fe)	1.28 (1.28)	1.48 (2.76)	1.39 (4.15)	0.77	0.25
$Fe_3Co(PO_4)_4$ (010) (Fe)	1.37 (1.37)	1.47 (2.84)	1.36 (4.20)	0.72	0.24
$Fe_2Co_2(PO_4)_4$ (010) (Fe)	1.33 (1.33)	1.54 (2.87)	1.33 (4.20)	0.72	0.31
$FeCo_3(PO_4)_4$ (010) (Fe)	1.32 (1.32)	1.58 (2.90)	1.27 (4.17)	0.75	0.35
$Fe_3Co(PO_4)_4$ (010) (Co)	1.28 (1.28)	1.76 (3.04)	1.24 (4.28)	0.64	0.53
$Fe_2Co_2(PO_4)_4$ (010) (Co)	1.28 (1.28)	1.74 (3.02)	1.47 (4.49)	0.43	0.51
$FeCo_3(PO_4)_4$ (010) (Co)	1.46 (1.46)	1.72 (3.18)	1.16 (4.34)	0.58	0.49
$Fe_4(PO_4)_4$ (Fe)	0.73 (0.73)	1.54 (2.27)	1.47 (3.74)	1.18	0.31
$Fe_3Co(PO_4)_4$ (Fe)	0.77 (0.77)	1.52 (2.29)	1.49 (3.78)	1.14	0.29
$Fe_2Co_2(PO_4)_4$ (Fe)	0.79 (0.79)	1.52 (2.31)	1.54 (3.85)	1.07	0.31
$FeCo_3(PO_4)_4$ (Fe)	0.81 (0.81)	1.52 (2.33)	1.55 (3.88)	1.04	0.32
$Fe_3Co(PO_4)_4$ (Co)	1.14 (1.14)	1.71 (2.85)	1.28 (4.13)	0.79	0.48
$Fe_2Co_2(PO_4)_4$ (Co)	1.15 (1.15)	1.73 (2.88)	1.25 (4.13)	0.79	0.50
$FeCo_3(PO_4)_4$ (Co)	1.18 (1.18)	1.72 (2.90)	1.26 (4.16)	0.76	0.49
$Co_4(PO_4)_4$ (Fe)	1.17 (1.17)	1.74 (2.91)	1.23 (4.14)	0.78	0.51
Fe_8O_{12} (Fe)	0.52 (0.52)	0.97 (1.49)	2.30 (3.79)	1.13	1.07
$Fe_6Co_2O_{12}$ (Fe)	0.70 (0.70)	1.25 (1.95)	1.96 (3.91)	1.01	0.73
$Fe_4Co_4O_{12}$ (Fe)	0.76 (0.76)	1.21 (1.97)	2.13 (4.10)	0.82	0.90
$Fe_2Co_6O_{12}$ (Fe)	0.76 (0.76)	1.28 (2.04)	2.17 (4.21)	0.71	0.94
$Fe_6Co_2O_{12}$ (Co)	1.10 (1.10)	1.59 (2.69)	1.69 (4.38)	0.54	0.46
$Fe_4Co_4O_{12}$ (Co)	1.03 (1.03)	1.61 (2.64)	1.60 (4.24)	0.68	0.38
$Fe_2Co_6O_{12}$ (Co)	1.03 (1.03)	1.56 (2.59)	1.65 (4.24)	0.68	0.42
Co_8O_{12} (Co)	1.05 (1.05)	1.57 (2.62)	1.64 (4.26)	0.66	0.41

Table 2.5. Surface energies (γ) of $Fe_3Co(PO_4)_4$. $\gamma = (E_{surf} - n \times E_{bulk})/2A$ where E_{surf} is total energy of each surface including n formula units, E_{bulk} is total energy per formula unit of $Fe_3Co(PO_4)_4$, and A is surface area. Miller index is based on the $Fe_3Co(PO_4)_4$ bulk unit cell. Copyright 2019, Springer Nature.

Surface	(010)	(100)	(101)	(111)	(001)	(110)
γ ($J \cdot m^{-2}$)	0.36	0.63	0.64	0.84	0.93	1.04

2.4.2. Catalyst synthesis

In light of above findings, we synthesized three catalysts of [**1:** ($Fe_3Co(PO_4)_4$@rGO), **2:** ($Fe_{1\text{-}1.33}Co(PO_4)_2$@rGO) (or $FeCo(PO_4)_2$@rGO), **3:** ($Fe_{1.5\text{-}2}Co(PO_4)_3$@rGO) (or $Fe_2Co(PO_4)_3$@rGO)] with a one-pot temperature-programmed carbonization process (Figure 2.7a, Methods). Since **1** shows the best activity, we will focus our discussion on **1**, unless otherwise specified.

2.4.3. Scanning and transmission electron microscopy analysis

Catalyst 1: The scanning electron microscopy (SEM) and low-resolution transmission electron microscopy (TEM) images of **1** show that $Fe_3Co(PO_4)_4$ nanoparticles (NPs) are uniformly distributed on the rGO surface with diameters 50-70 nm (Figure 2.7b). The high-resolution TEM (HRTEM) and fast-Fourier-transform (FFT) images reveal that the $Fe_3Co(PO_4)_4$ NPs are crystalline (Figure 2.7c). The HRTEM images show *d*-spacing values of 2.98 Å, corresponding to the {020} planes for the $Fe_3Co(PO_4)_4$ crystal. Plane defects and atomic dislocations (yellow dots in Figure 2.7c) enhance the specific area and the electrocatalytic site for further boosting the OER activity. In addition, high-angle annular-dark-field scanning-TEM energy-dispersive spectroscopy (HAADF-STEM-EDS) mapping was used to examine the elements distribution in $Fe_3Co(PO_4)_4$@rGO (Figure 2.7d). Composition line-scan profiles across a NP of 1 shows that Fe/Co/P elements are distributed throughout the NP (Figure 2.7e).

Catalyst 2 & 3: The SEM and TEM images show that nanoparticles (NPs) in both catalysts **2** and **3** are uniformly distributed on the rGO surface (Figures 2.8a & 2.9a). From the TEM images, we note that the diameters of NPs increase with increasing cobalt content in the $Fe_xCo_y(PO_4)_{x+y}$@rGO (Figures 2.8a & 2.9a). The HR-TEM images demonstrate that both NPs are crystalline (Figures 2.8b & 2.9b). Furthermore, the HRTEM image of catalyst **2** shows the d-spacing of ~0.221 nm (Figure 2.8b), while in catalyst **3** the d-spacing is ~0.298 nm (Figure 2.9b). The elements distribution in catalyst **2** and **3** are examined by high-angle annular-dark-field scanning-TEM energy-dispersive spectroscopy (HAADF-STEM-EDS), which show that the NPs in both catalysts are composed of Fe, Co and P supported on carbon (Figures 2.8c & 2.9c).

2.4.4. X-ray diffraction (XRD) analysis

Catalyst 1: The X-ray diffraction (XRD) patterns of **1** show the peaks at 20.3°, 30.3°, 48.52° and 52.1° (marked as "▼") corresponding to {101}, {020}, {220}, and {$22\bar{2}$} crystal planes, respectively, for a monoclinic $Fe_3Co(PO_4)_4$ crystal (space group: Pm) (Figures 2.7 f & 2.10). Additionally, the {020} peak has the maximum intensity, indicating that the c-axis [010] is the growth direction of $Fe_3Co(PO_4)_4$ crystal. Both theoretical and experimental patterns are quite similar; however, few peaks slightly blue-shifted in experiment, indicating the volume expansion with increased lattice spacing (due to phosphate intercalation) and crystal defects/dislocations (due to strain effect during the metal cations formation). These observations are in good agreement with the HRTEM results as discussed earlier. The expanded curves of $Fe_3Co(PO_4)_4$@rGO show a broad band at 26.3° (marked as "♦") corresponding to the (002) plane of rGO, indicating the successful reduction of GO and formation of graphitic structures with interlayer spacing of 0.34 nm.[21-23] A few small unmatched diffraction peaks, such as 35-39°, 41-42°, 55-60°, and 63-80°, are not clear to us because there can be so many possible structures in small quantities, but may be resulted from a by-product adduct $Fe_{4.1}Co_{2.9}(PO_4)_6$, mono-metallic iron or cobalt phosphate during the one-pot temperature-programmed carbonization process (Figure 2.10). However, it is clear that they are not a significant issue because all experimental results are well explained by our theoretical models.

Catalyst 2-5: The powder X-ray diffraction (XRD) patterns of as-synthesized catalysts **2**, **3**, **4** and **5** are characterized, which confirms the formation of crystalline phase (Figure 2.11). The XRD peaks (except one peak at 32.8^0) of catalyst **4** match with the standard PDF card of $Fe_2P_2O_7$@rGO (JCPDS 01-076-1762). The peak at 32.8^0 matches with the PDF card of Fe_2PO_5 (JCPDS 00-036-0084). The XRD pattern of catalyst **5** shows a mixture of $CoFe_2O_4$ and Fe_2O_3, in good agreement with the standard data (JCPDS 01-079-1744 for $CoFe_2O_4$ and 01-079-1744 for Fe_2O_3). Consequently, XRD patterns of **2-5** indicate the formation of desired products with the highest degree of crystallinity.

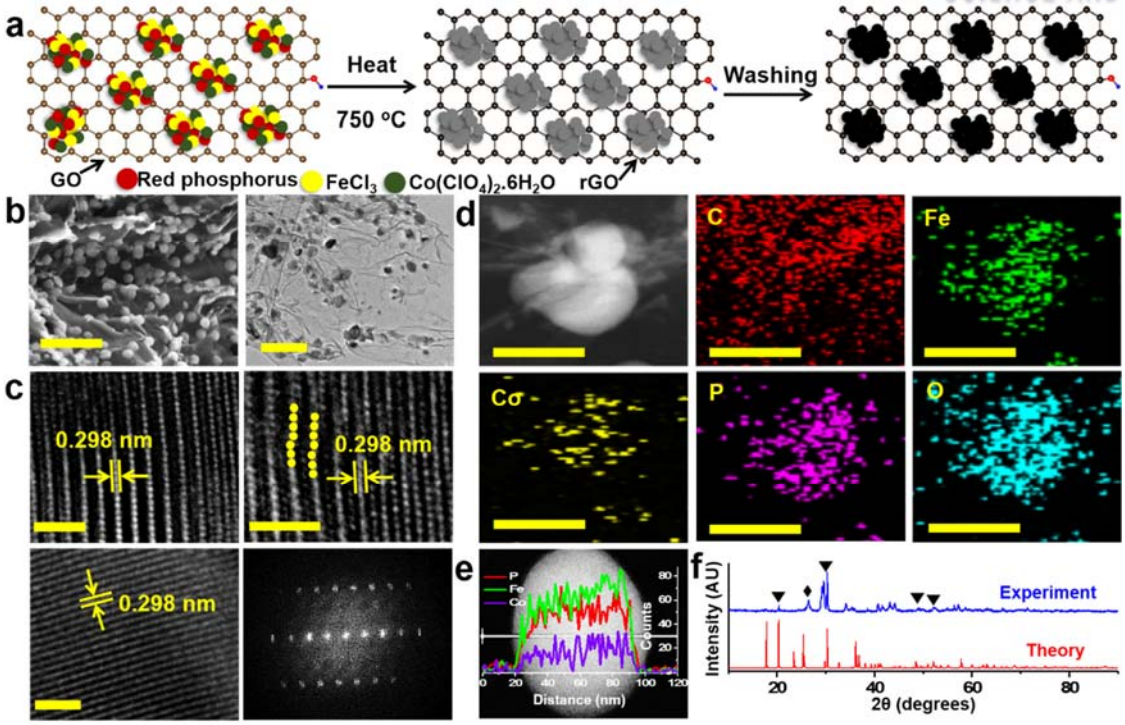

Figure 2.7. Preparation route, structural and compositional characterizations of $Fe_3Co(PO_4)_4$@rGO (**1**). **(a)** Synthesis procedure: First, mix the sample of graphene oxide, red phosphorus, $FeCl_3$, and $Co(ClO_4)_2 \cdot 6H_2O$, and then heat. Second, leach with acid, wash with DI water and dry in oven. **(b)** Scanning (left) and transmission (right) electron micrographs. Scale bars, 200 nm. **(c)** Representative high-resolution transmission electron microscopy (HRTEM) images for different positions of single-particle (yellow dots denote atomic dislocations). Fast Fourier transform (FFT) image is on right-bottom panel. Scale bars, 2 nm. **(d)** High-angle annular dark field-scanning transmission electron microscope (HAADF–STEM) image and their corresponding individual element maps of C, Fe, Co, P, and O in a part of **1**. **(e)** HAADF–STEM image with the overlapping image showing the corresponding EDS line scan profiles. Scale bars, 50 nm. **(f)** X-ray diffraction pattern, which confirms the formation of $Fe_3Co(PO_4)_4$ in **1**. The peak marked by black diamond denotes the rGO peak. Additional small unmatched peaks may be resulted from the by-product adduct of $Fe_{4.1}Co_{2.9}(PO_4)_6$ and mono-metallic iron or cobalt phosphate (Figure 2.10). Copyright 2019, Springer Nature.

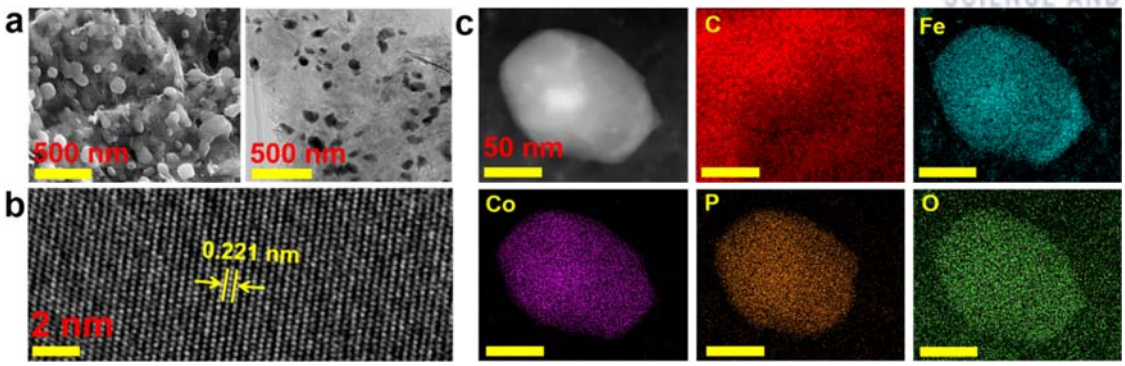

Figure 2.8. Structural and compositional characterizations of $FeCo(PO_4)_2$@rGO (**2**). **(a)** Scanning (left) and transmission (right) electron micrographs. SEM and TEM images show that the diameters of NPs are in the range of 70–130 nm **(b)** HRTEM image of single-particle. **(c)** HAADF–STEM image and their corresponding individual element maps of C, Fe, Co, P, and O. Copyright 2019, Springer Nature.

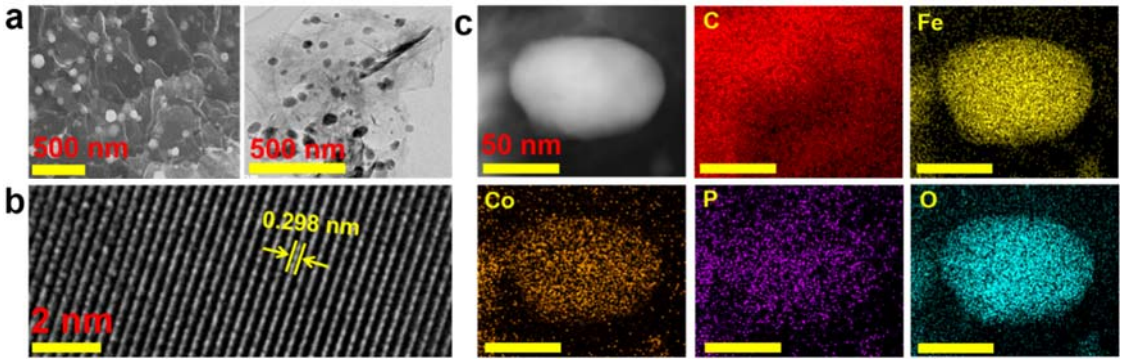

Figure 2.9. Structural and compositional characterizations of $Fe_2Co(PO_4)_3$@rGO (**3**). **(a)** Scanning (left) and transmission (right) electron micrographs. SEM and TEM images show that the diameters of NPs are in the range of 60–95 nm **(b)** HRTEM image of single-particle. **(c)** (HAADF–STEM) image and their corresponding individual element maps of C, Fe, Co, P, and O. Copyright 2019, Springer Nature.

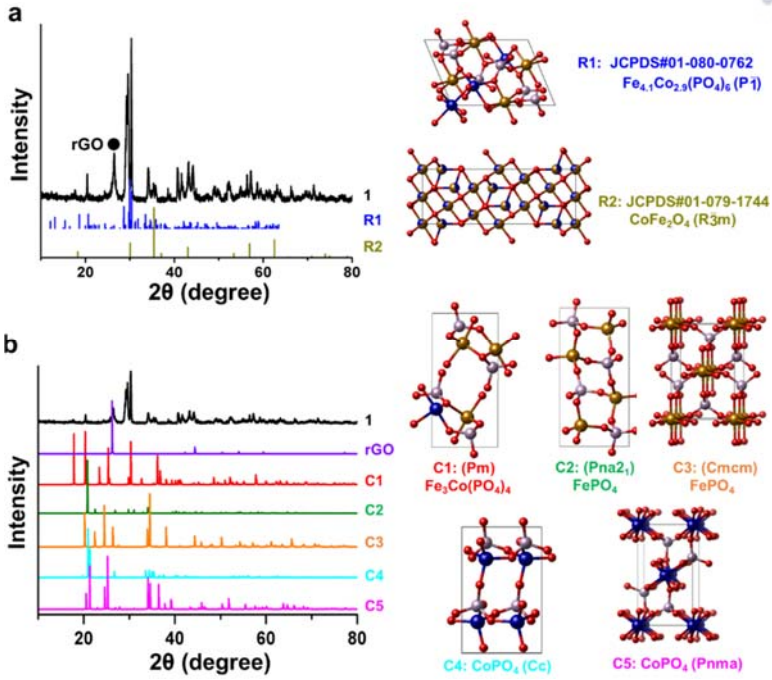

Figure 2.10. XRD characterization for **1** [$(Fe_3Co(PO_4)_4$@rGO] compared with the experimental XRD spectra [obtained from crystal structures. $Fe_{4.1}Co_{2.9}(PO_4)_4$ and $CoFe_2O_4$] and the calculated XRD spectra [based on different metal phosphates crystal structures]: **(a)** Comparison of the experimental XRD spectra of **1**. **(b)** Comparison of the experimental XRD spectra of **1** with the calculated XRD spectra (C1-C5) based on DFT-predicted various metal phosphates crystal structures. The XRD spectra of **1** are similar mainly to those of C1: $Fe_3Co(PO_4)_4$ (Pm) and partly to those of C_3: $FePO_4$ (Cm). Copyright 2019, Springer Nature.

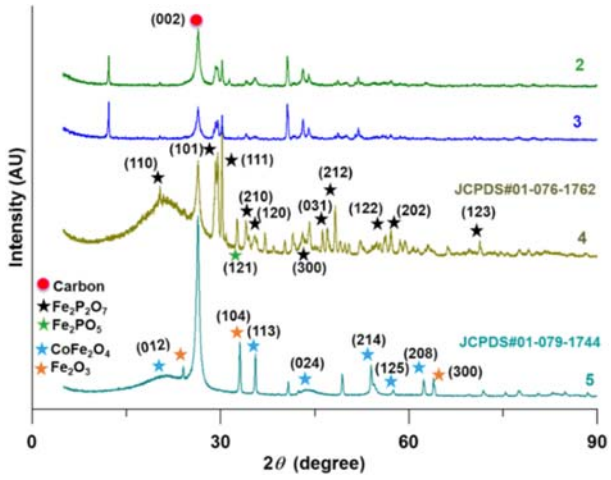

Figure 2.11. X−ray diffraction (XRD) characterization. XRD patterns for catalysts of **2**: $FeCo(PO_4)_2$@rGO, **3**: $Fe_2Co(PO_4)_3$@rGO, **4:** $(Fe_2P_2O_7)$@rGO, and **5**:$(CoFe_2O_4$ $)(Fe_2O_3)$@rGO.

2.4.5. X-ray absorption fine structure analysis

We conducted Fourier transform X-ray absorption fine structure (FT–EXAFS) analysis which provided the chemical state and coordination environments.[24-25] The energies of both XANES Fe K-edges and Co K-edges of **1** and $FeCo(PO_4)_2$@rGO (**2**) are positively shifted compared with those of Fe/Co foils (Figure 2.12a, d), suggesting the oxidized states of Fe/Co. The FT-EXAFS data of Fe and Co in **1** and **2** exhibit similar peak patterns, but the peak intensities and positions are slightly changed due to their different compositions. Meanwhile, Fe and Co foils show different peak positions for Fe–Fe and Co–Co bonds (Figure 2.12b, e). We analyzed the EXAFS curve of **1** using least-square fit for first- and second-shells. (Figures 2.12c and 2.13a) show that the major peaks at 2.0 Å (coordination number (CN): 4.1) and 2.2 Å (CN: 1.9) reflect Fe=O and Fe–O bond distances while the minor peak reflects the overlapped peaks at Fe···P distances (via O) of 2.9/3.1/3.3 Å (CN: 1.6/1/2.4, respectively) (Table 2.6). Similarly, Figures 2.12f and 2.13b show peaks at 2.0 Å (CN: 2) and 2.4 Å (CN: 4) for Co=O and Co–O bond distances while a major peak at 2.8 Å (CN: 5) for the Co···P distance via O (Table 2.7).

We calculated theoretical Fe/Co K-edge EXAFS of $Fe_3Co(PO_4)_4$ using the FDMX package.[26-27] These theoretical FT-EXAFS spectra of the Co and Fe atoms are similar to the experimental FT-EXAFS spectra of **1** in r-space (Figure 2.14). It seems that the difference between Fe and Co K-edge EXAFS of **1** arises from different Fe-P distances at each Fe sites in the crystal (Tables 2.6 and 2.7). To confirm this, we calculated EXAFS of pure $Fe_4(PO_4)_4$ and $Co_4(PO_4)_4$, where the Co K-edge FT-EXAFS spectra of $Co_4(PO_4)_4$ are similar to the Fe K-edge FT-EXAFS in r-space. This indicates that Co atoms well replace Fe sites in the $Fe_3Co(PO_4)_4$ lattice.

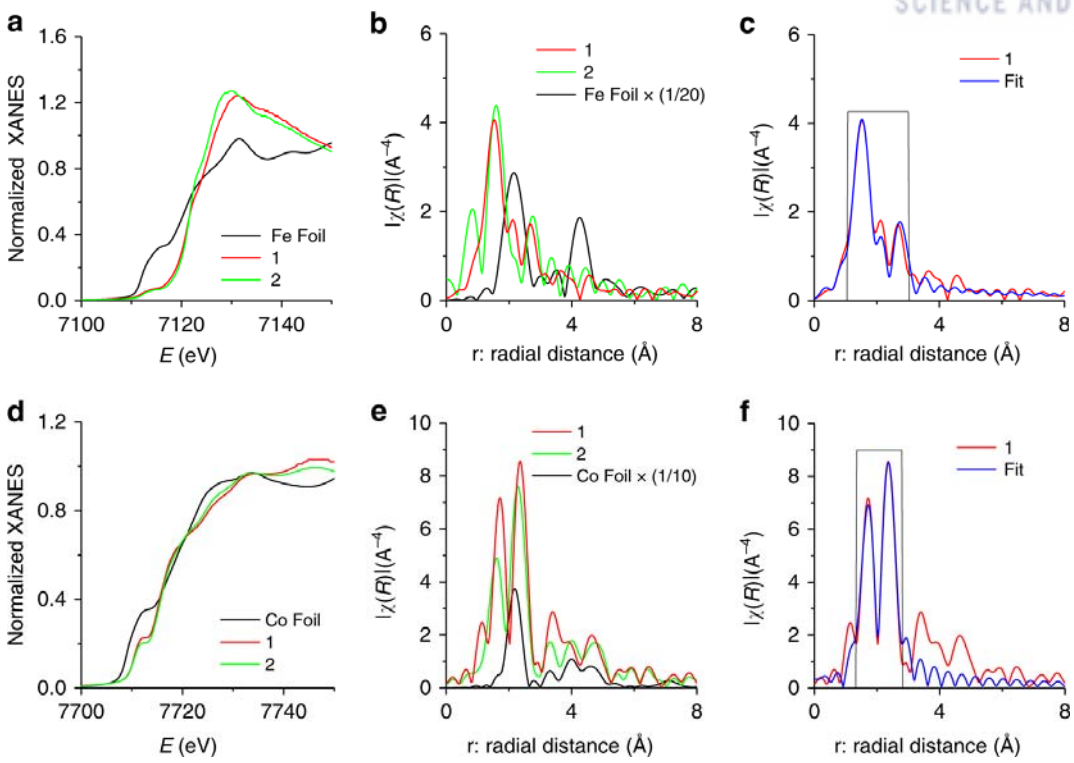

Figure 2.12. X-ray absorption spectra. **(a-c)** Fe K-edge. **(d-f)** Co K-edge. (a,d) XANES spectra for Fe K- and Co-K edges. (b,e) Fourier transform (FT) of the EXAFS spectra in real space at Fe K- and Co K-edges. (c,f) FT-EXAFS spectra in r-space and the corresponding least-squares fit (black rectangular line) for 1st and 2nd shells. **1**: $Fe_3Co(PO_4)_4$@rGO; **2**: $FeCo(PO_4)_2$@rGO. Copyright 2019, Springer Nature.

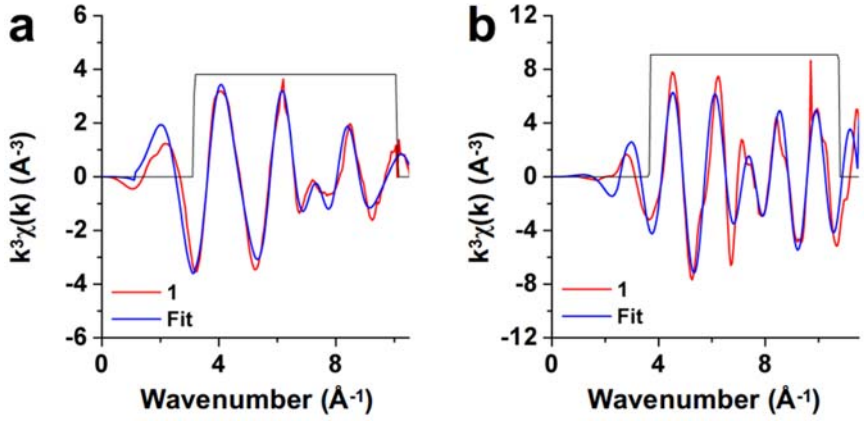

Figure 2.13. EXAFS χ(k) signals in k-space and the corresponding least-squares fit (black solid line) for 1st shell. **(a)** Fe and **(b)** Co. **1**: $Fe_3Co(PO_4)_4$@rGO. Copyright 2019, Springer Nature.

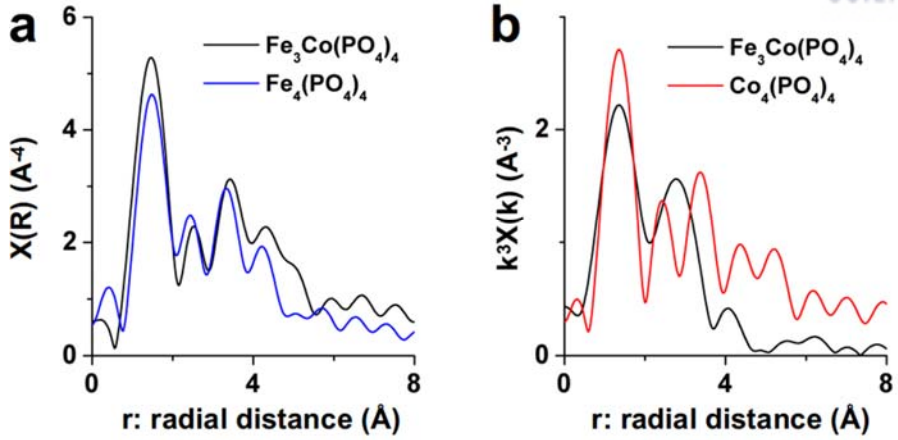

Figure 2.14. Calculated FT-EXAFS spectra in r-space of $Fe_3Co(PO_4)_4$ crystal structure compared with $Fe_4(PO_4)_4$ and $Co_4(PO_4)_4$. **(a)** Fe K-edge XAFS and **(b)** Co site K-edge XAFS are calculated using FDMX[26-27] with a full-potential finite difference method (FDM). Both Fe K-edge XAFS of $Fe_4(PO_4)_4$ and Co site K-edge XAFS of $Co_4(PO_4)_4$ are similar. Though Fe K-edge XAFS of $Fe_3Co(PO_4)_4$ is similar to that of $Fe_4(PO_4)_4$, the Co K-edge XAFS of $Fe_3Co(PO_4)_4$ is significantly different from that of $Co_4(PO_4)_4$, because the former has no neighboring Co atoms, while $Co_4(PO_4)_4$ has four neighboring Co atoms. Copyright 2019, Springer Nature.

Table 2.6. Curve-fitting analysis for Fe K-edge EXAFS of $Fe_3Co(PO_4)_4$@rGO before and after OER test (R-factor=0.0082): Fe K-edge EXAFS curve fitting parameters (R: Bond distance, CN: Coordination number, σ^2: Debye-Waller factor, ΔE_0: energy shift). Copyright 2019, Springer Nature.

Before OER test

Path	R(Å)	CN (atoms)	σ^2 (Å^2)	ΔE_o
Fe-O	2.02 ± 0.03	4.1	0.010 ± 0.002	4.98 ± 2.52
Fe-O	2.23 ± 0.03	1.9	0.010 ± 0.002	4.98 ± 2.52
Fe-P	2.88 ± 0.06	1.6	0.010 ± 0.004	4.98 ± 2.52
Fe-P	3.11 ± 0.18	1.0	0.010 ± 0.004	4.98 ± 2.52
Fe-P	3.31 ± 0.07	2.4	0.010 ± 0.004	4.98 ± 2.52

After OER test

Path	R(Å)	CN (atoms)	σ^2 (Å^2)	ΔE_o
Fe-O	2.00 ± 0.02	4.8	0.012 ± 0.001	4.08 ± 2.65
Fe-O	2.21 ± 0.02	1.2	0.012 ± 0.001	4.08 ± 2.65
Fe-P	2.75 ± 0.04	1.3	0.006 ± 0.003	4.08 ± 2.65
Fe-P	2.94 ± 0.11	1.0	0.006 ± 0.003	4.08 ± 2.65
Fe-P	3.19 ± 0.03	2.7	0.006 ± 0.003	4.08 ± 2.65

Table 2.7. Curve-fitting analysis for Co K-edge EXAFS of $Fe_3Co(PO_4)_4$@rGO before and after OER test (R-factor before OER=0.0025, R-factor after OER=0.0041): Co K-edge EXAFS curve fitting parameters (R: Bond distance, CN: Coordination number, σ^2: Debye-Waller factor, ΔE_0: energy shift). Copyright 2019, Springer Nature.

Before OER test

Path	R(Å)	CN (atoms)	σ^2 (Å^2)	ΔE_o
Co-O	1.98 ± 0.01	2	0.0058 ± 0.0008	-2.56 ± 1.07
Co-O	2.39 ± 0.01	4	0.0058 ± 0.0008	-2.56 ± 1.07
Co-P	2.81 ± 0.01	5	0.0039 ± 0.0005	-2.56 ± 1.07

After OER test

Path	R(Å)	CN (atoms)	σ^2 (Å^2)	ΔE_o
Co-O	1.94 ± 0.01	2	0.006 ± 0.001	-7.34 ± 1.37
Co-O	2.35 ± 0.01	4	0.006 ± 0.001	-7.34 ± 1.37
Co-P	2.79 ± 0.01	5	0.007 ± 0.001	-7.34 ± 1.37

2.4.6. X-ray photoelectron spectroscopy analysis

The core-level P-2p X-ray photoelectron spectroscopy (XPS) shows two major peaks at binding energies of 133.3±0.1 and 134.2±0.1 eV, corresponding to the $2p_{3/2}$ and $2p_{1/2}$ core levels of central phosphorus atoms in phosphate species[28], which is characteristic of the tetrahedral (PO_4)-group[29] (Figure 2.15a). Furthermore, the O-1s XPS spectra show two peaks at 531.4 and 532.5 eV, assigned to phosphate species[30] (Figure 2.15b). The atomic ratio of Fe/Co are 3/1 or 3.1/1, as measured by inductively-coupled-plasma atomic-emission-spectroscopy (ICP-AES) (Table 2.1). Also XPS analysis provides the atomic percentage near sample surface. As compared with ICP-AES bulk sample analysis, the XPS surface analysis increases the $Fe(PO_4)$ content, while the atomic content of P (or PO_4) is almost the sum of Co and Fe atomic contents, indicating the charges of Co and Fe are +3 (Table 2.2). The content of O is slightly larger than four times of the content of P due to environmental oxygen. An extra content of $Fe(PO_4)$, as noted from XPS over ICP-AES could be present on the surface more than in bulk. However, the XPS data are not so reliable for accurate composition analysis as compared with ICP-AES. The Fe/Co metals composition ratio from ICP-AES is more reliable. Overall, the elemental composition turns out to be **1:** $Fe_3Co(PO_4)_4$@rGO (Fe/Co=3), **2**: $FeCo(PO_4)_2$@rGO ($Fe_4Co_3(PO_4)_7$@rGO) (Fe/Co=1-1.33) and **3**: $Fe_2Co(PO_4)_3$@rGO (or $Fe_3Co_2(PO_4)_5$@rGO) (Fe/Co=1.5-2). To facilitate our discussion, **2** and **3** will be simply denoted as **2**: $FeCo(PO_4)_2$@rGO and **3**: $Fe_2Co(PO_4)_3$@rGO in consideration with the experimental component analysis.

Core-level XPS Spectra of C, Co on Fe in catalysts 1-4: The core-level XPS spectrum of C 1s in catalyst **1** shows the main strong and sharp peak at 284.6 eV corresponds to graphitic carbon, while the peak located at 285.8 eV is assigned to C-O/C-P (Figure 2.16a).[31] The spectrum of Co 2p in catalyst **1** displays the core-level XPS peaks at 782.3 eV (2p3/2) and 797.4 eV (2p1/2) with satellite peaks at 786.6, 790.7, and 803 eV corresponding to the Co^{2+} state (Figure 2.16b).[32] The Fe 2p spectrum in catalyst **1** exhibits peaks of two different spin-orbits. The peaks located at binding energies of 713.2 and 725.3 eV with shakeup satellites (718.8 and 728 eV) are attributed to $2p_{3/2}$ and the $2p_{1/2}$ of Fe^{3+}, while the peak located at binding energy of 711.6 eV with satellite peak of 715.3 eV correspond to Fe^{2+} state (Figure 2.16c).[33-35] The peaks position in the core-level XPS spectra of C, P, O, Co and Fe in catalysts 2-4 are almost similar to that of catalyst **1**(Figures 2.17-2.19).

Core-level XPS spectra of 5: The XPS spectrum of C 1s in catalyst **5** shows the peak of graphitic carbon and C-O at binding energies of 284.4 and 285.8, respectively (Figure 2.20a).[31] The high resolution XPS spectrum of oxygen shows three peaks at binding energies of 529.6, 531.6, and 532.9 eV, which can be assigned to metal-oxygen bond, metal-hydroxides, and adsorbed oxygen species (Figure 2.20b).[36-37] The XPS spectrum of Co 2p displays core-level peaks at binding energies of 780.9 eV (2p3/2) and 795.6 eV (2p1/2) with satellite peaks at 784.1, 787.5, and 790.8, eV corresponding to the Co^{2+} species in $(CoFe_2)O_4$ (Figure 2.20c).[38-39] The high resolution XPS spectrum of Fe 2p in $(CoFe_2)O_4$ exhibits peaks of two different spin-orbits. The peaks at binding energies of 710.1 and 723.9 eV corresponding to Fe_3O_4, while the peak located at binding energy of 712 eV with satellite peaks of 718.7 and 726.2 eV corresponds to Fe^{3+} state (Figure 2.20d). [34-35, 40]

Core-level XPS spectra of Catalysts 6-9: The figures 2.21-2.24 show the core-level XPS spectra of C 1s, P 2p, O 1s, Co 2p and Fe 2p of catalysts **6-9**. In all these catalysts **6-9**, the C Is have the peaks of graphitic carbon (284.3-284.5 eV) and C-O/C-P (285.3 or 285.6 eV) (Figures 2.21a-4.24a).[31] Similarly, the XPS spectra of O 1s in catalysts **6-9** show the peaks at binding energies which can be assigned to phosphate group (Figures 2.21c-4.24c).[41] The core-level XPS spectra of P 2p, Co 2p and Fe 2p of catalysts **7-9** have almost similar binding energy to that of catalyst **1** in which the XPS spectra of P 2p show the typical peaks of phosphate species at binding energies of 133.1-133.3 eV and 134-34.2 eV (Figures 2.22b-2.24b).[41] The binding energies of Co and Fe spectra (Figures 2.22d, e – 2.24d, e**)** show that Co and Fe in catalysts **7-9** have similar cationic states to that of catalyst **1**. However, in catalyst **6** we note that the core-level XPS spectra of P 2p, Co 2p and Fe 2p have some different peaks compared to catalyst **1**. For example, the core-level XPS spectrum of P 2p in catalyst **6** shows two different states of peaks (Figure 2.21b), one can be assigned to phosphide (unresolved doublet centered at 129.6 eV)[42] and the other to phosphate (resolved doublet centered at 133.1 eV and 134 eV).[41] The high-resolution XPS spectrum of Co 2p in catalyst **6** shows two pairs of peaks (Figure 2.21d). The peaks located at binding energies of 778.9 and 794.3 eV are assigned to metallic Co in CoP[25], while the peaks at binding

energies of 782.4 and 799.2 eV with shakeup satellites (787.6 and 804.4 eV) correspond to cationic cobalt in metal phosphate.[32] Similarly, the core-level XPS of Fe 2p in catalyst **6** shows zero valence state peaks at binding energies of 707.2 and 720 eV[25] and cationic state peaks at binding energies of 711.8, 714.3 and 725.1 eV with shakeup satellite peaks at 716.6 and 728.7 eV, which are attributed to metal phosphide and metal phosphate, respectively (Figure 2.21e).

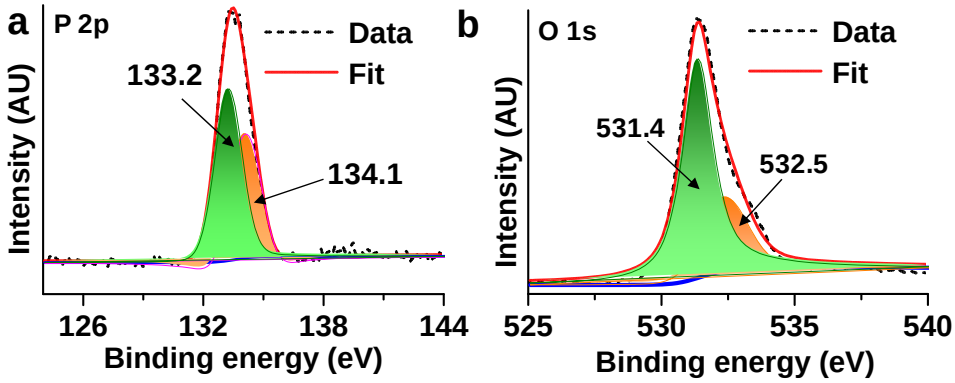

Figure 2.15. X-ray Photoelectron Spectroscopy (XPS) core-level spectra of **1** before stability tests. **(a)** P_{2p}, and **(b)** O_{1s}, Copyright 2019, Springer Nature.

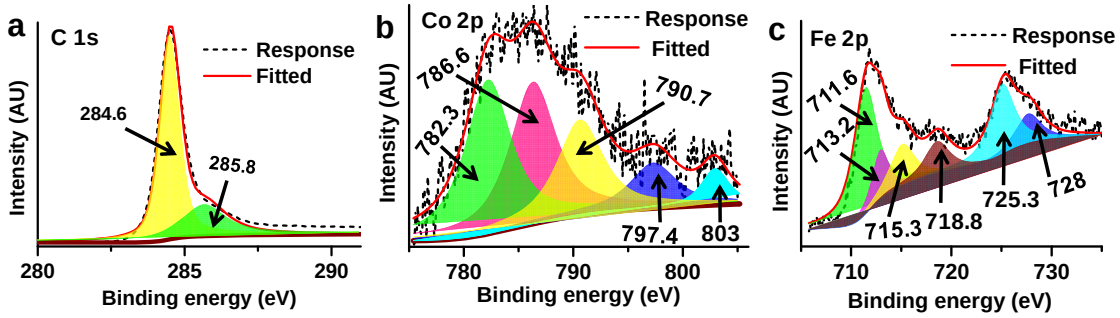

Figure 2.16. XPS core-level spectra of **1** before stability tests. **(a)** C 1s; **(b)** Co 2p; **(c)** Fe 2p. Copyright 2019, Springer Nature.

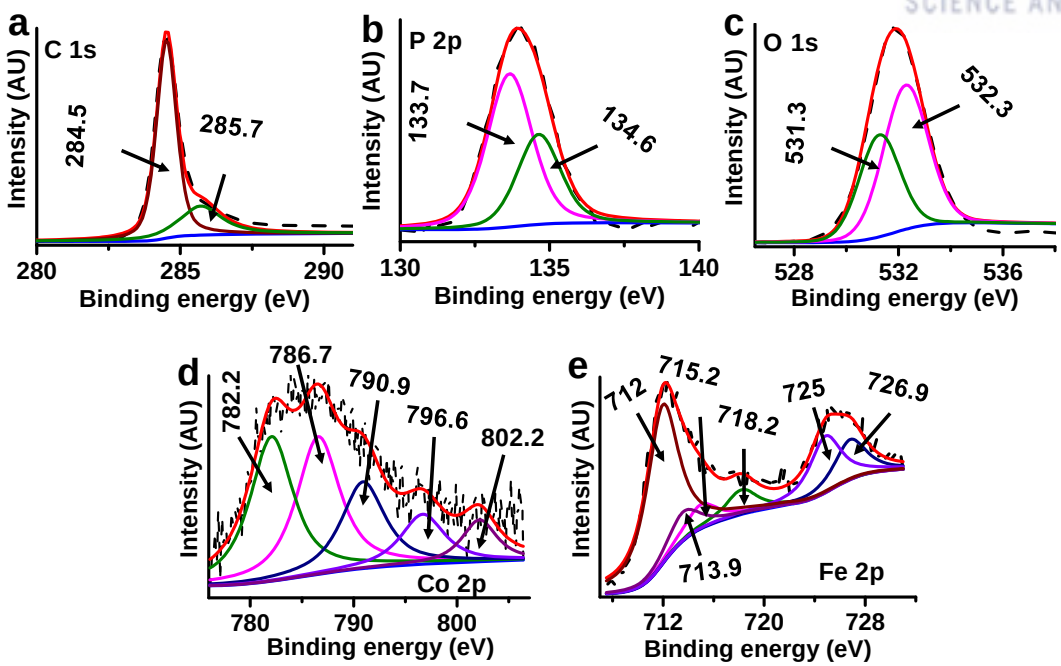

Figure 2.17. XPS core-level spectra of catalyst **2**. **(a)** C 1s; **(b)** P 2p; **(c)** O 1s; **(d)** Co 2p; **e,** Fe 2p.

Copyright 2019, Springer Nature.

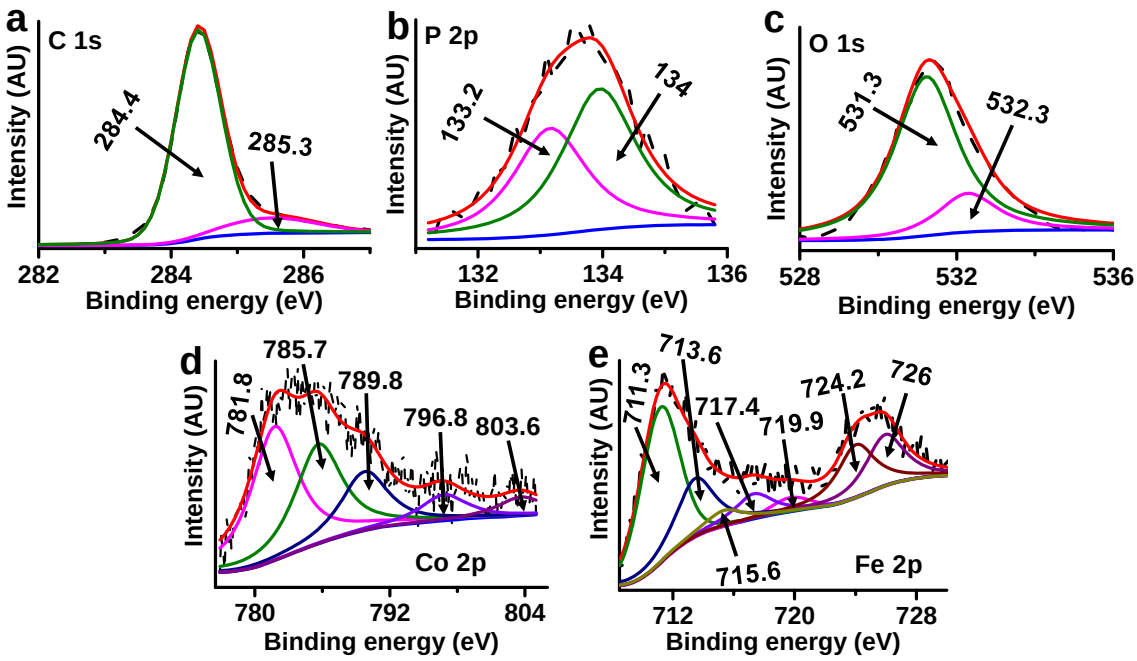

Figure 2.18. XPS core-level spectra of catalyst **3**. **(a)** C 1s; **(b)** P 2p; **(c)** O 1s; **(d)** Co 2p; **e,** Fe 2p.

Copyright 2019, Springer Nature.

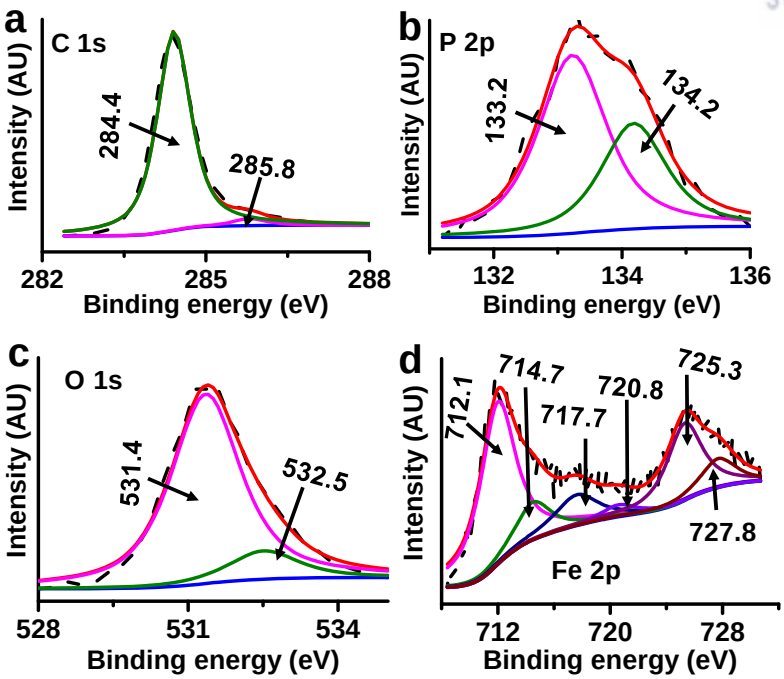

Figure 2.19. XPS core-level spectra of catalyst **4**. (**a**) C 1s; (**b**) P 2p; (**c**) O 1s; (**d**) Fe 2p. Copyright 2019, Springer Nature.

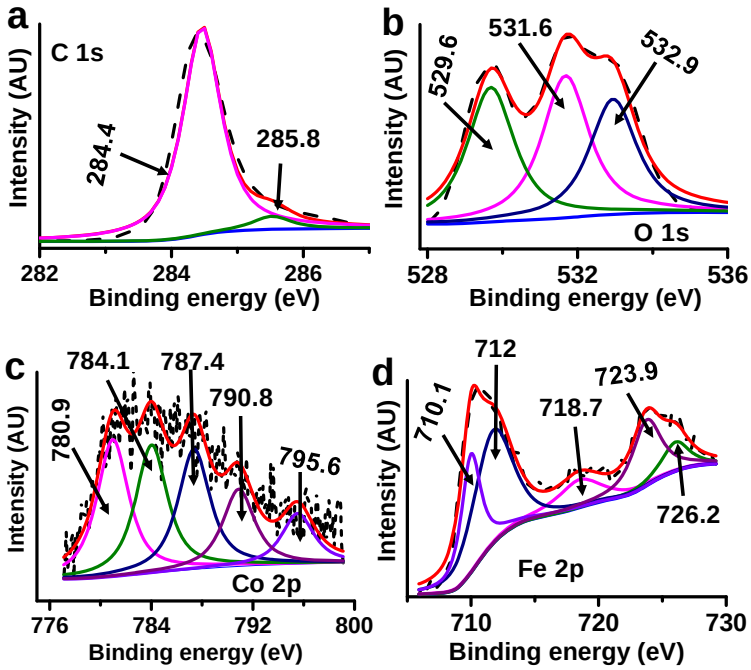

Figure 2.20. XPS core-level spectra of catalyst **5**. **(a)** C 1s; **(b)** O 1s; **(c)** Co 2p; **(d)** Fe 2p. Copyright 2019, Springer Nature.

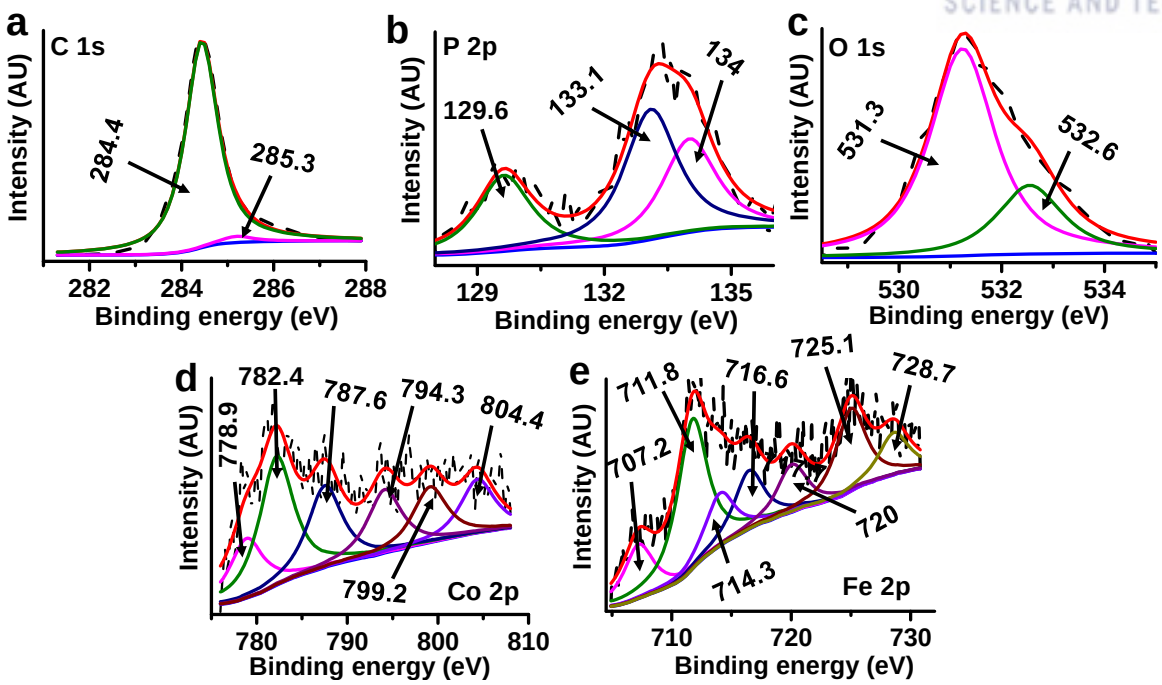

Figure 2.21. XPS core-level spectra of catalyst **6**. **(a)**C 1s; **(b)** P 2p; **(c)** O 1s; **(d)** Co 2p; **(e)** Fe 2p. Copyright 2019, Springer Nature.

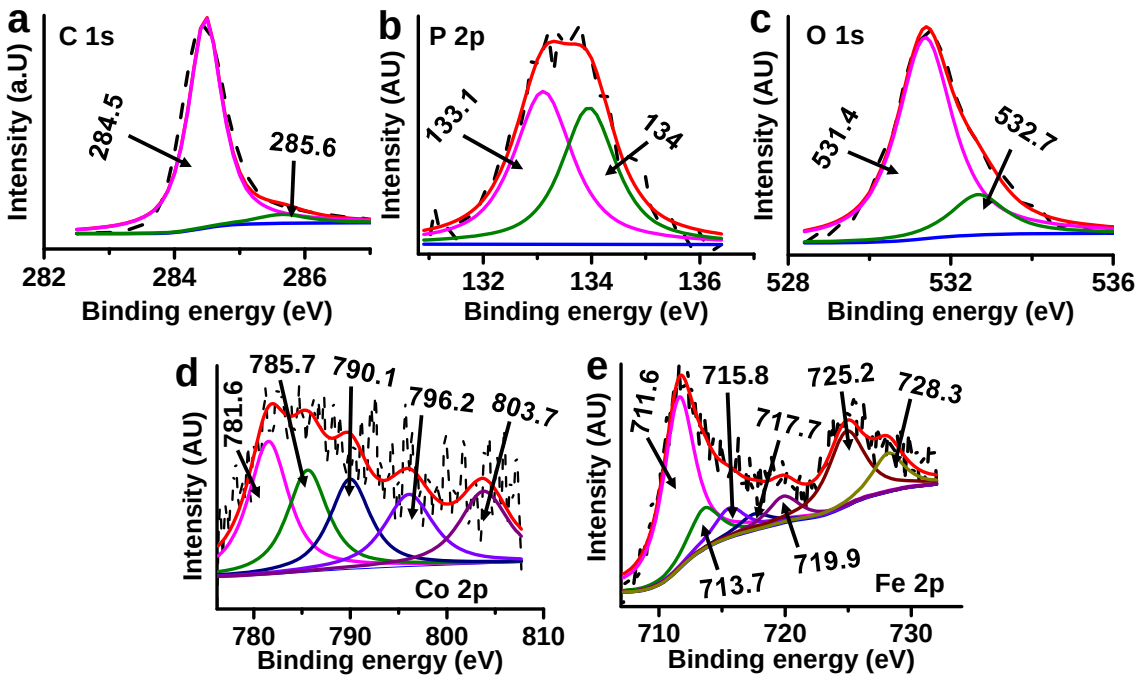

Figure 2.22. XPS core-level spectra of catalyst **7**. **(a)** C 1s; **(b)** P 2p; **(c)** O 1s; **(d)** Co 2p; **e,** Fe 2p. Copyright 2019, Springer Nature.

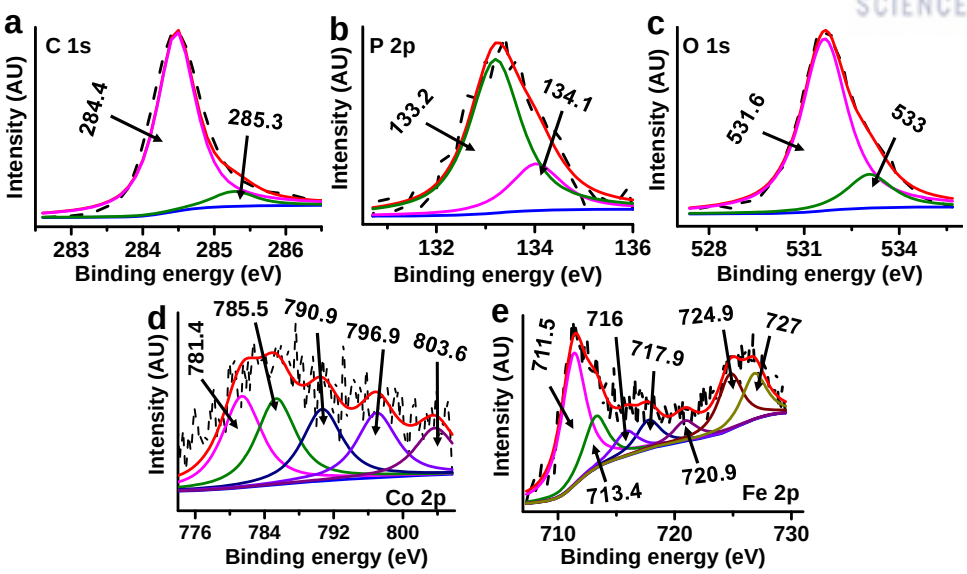

Figure 2.23. XPS core-level spectra of catalyst **8**. **(a)** C 1s; **(b)** P 2p; **(c)** O 1s; **(d)** Co 2p; **(e)** Fe 2p. Copyright 2019, Springer Nature.

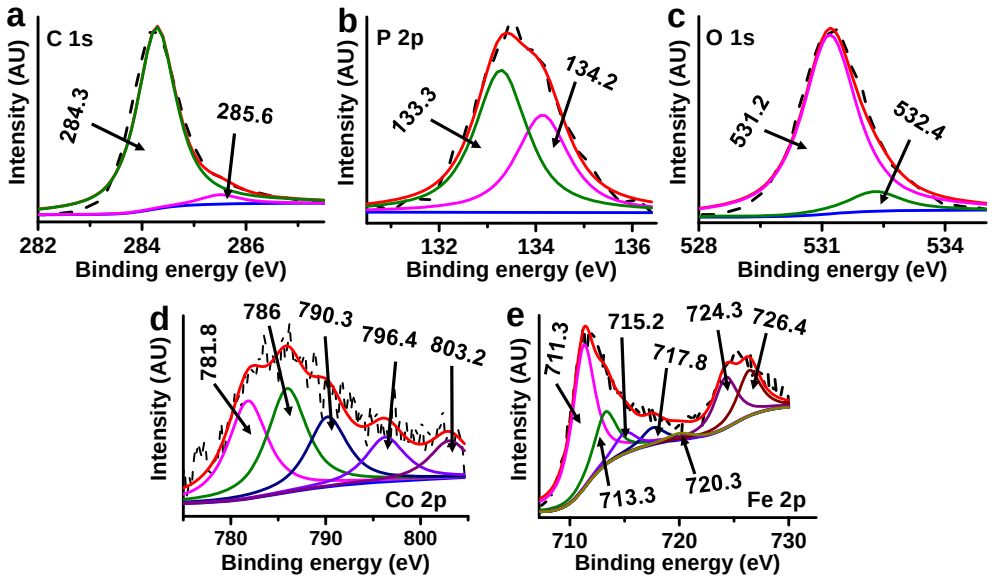

Figure 2.24. XPS core-level spectra of catalyst **9**. **(a)** C 1s; **(b)** P 2p; **(c)** O 1s; **(d)** Co 2p; **(e)** Fe 2p. Copyright 2019, Springer Nature.

2.4.7. Electrochemical performance

We performed electrochemical measurements to check the catalytic activities of catalysts **1-9** and commercial 20 wt% Ir/C for OER in 1M KOH electrolyte (Figures 2.25a and 2.26-2.28). The OER activity of these electrocatalysts are influenced by the amount of Fe or Co in the presence of phosphate, and the best activity is achieved for **1**. **1** exhibits very small overpotential of ~237 mV to afford a current

density of 100 mA cm^{-2}, lower than catalysts **2-9** and commercial Ir/C (Figure 2.25a, Figures 2.26-2.28). The benchmark Ir/C catalyst displayed a current density of 100 mA cm^{-2} at 303 mV (Figure 2.25a).

The TOF is calculated to be 0.54 s^{-1} at an overpotential of 237 mV, indicating a highly active catalyst, 7.6 times that of Ir/C 0.071 s^{-1} (details in Methods) which further confirms the outstanding OER performance of **1**. The Tafel slope is 57 mV $decade^{-1}$ (Figure 2.25b), smaller than that of Ir/C (117 mV $decade^{-1}$). The small overpotential at Fe sites of **1** is the key factor for the superior OER activity of **1**. For achieving this optimal overpotential, other environmental factors have also been utilized as follows. The large Brunauer-Emmett-Teller (BET) surface area (238 m^2/g) (Figure 2.29) with average pore size 4.3 nm promotes the contact between **1** and electrolyte, thereby helping in the optimal OER activity. The very low charge-transfer resistance (0.29 Ω on NF substrate, 7.5 Ω on GCE substrate) promotes electron transport, thereby leading to faster kinetics (Figure 2.30a, b). The electrochemical double-layer capacitance (C_{dl}=0.0162 F), which is directly correlated to the catalyst's active surface area, is very large, 8.1-fold the C_{dl} of Ir/C (0.002 F) (Figure 2.31). The defects/dislocations (strain effect)[43-44] of Fe and Co atoms in crystal help in improving the performance of active sites.

After initial and 5000 CV cycles, accelerated degradation test of **1** indicates the excellent durability as demonstrated by the near overlay of OER curves (Figure 2.25c). No significant changes in TEM/TEM-EDX, HRTEM, hard/soft-XAS, XPS, and Raman spectra (except for minor increase in FeO_x/FeOOH and CoO_x/CoOOH[45-46], which would not be so active like Fe sites of **1**, Figure 2.32) were observed before and after the test, indicating that **1** is quite durable (Figures 2.33-2.38). The stability of this catalyst was further assessed by chronoamperometry. **1** exhibited outstanding stability with no changes in current density of ~10 - 11 mA cm^{-2} (70 h on NF and 55h on GCE) and ~210 mA cm^{-2} (for 45 h on NF) ((Figure 2.25d and Figure 2.39). The high stability and durability of nanocrystal in **1** is ascribed to the graphene support (which is very stable in alkaline and acid media) and the strong coordination between Fe/Co and PO_4. Initially and 54h after stability test, the Faradaic efficiency (after 1h test) is ~98 and ~96 % in alkaline electrolyte, respectively (Methods).

To evaluate the real application, an overall water splitting cell was fabricated in which 1M/6M KOH was used as electrolyte and **1** served as the anode with 20 wt% Pt/C catalyst as the cathode. It required ~1.45 V in 1M KOH (1.39 V in 6M KOH) to facilitate overall water splitting at a current density of 10 mA cm^{-2} (Figure 2.25e and Figure 2.40), which is the lowest voltage, much lower than that of the benchmark combination (1.53 V; commercial Pt/C and Ir/C catalysts). It required nominal voltage of 1.4 V to drive overall water splitting (Figure 2.40).

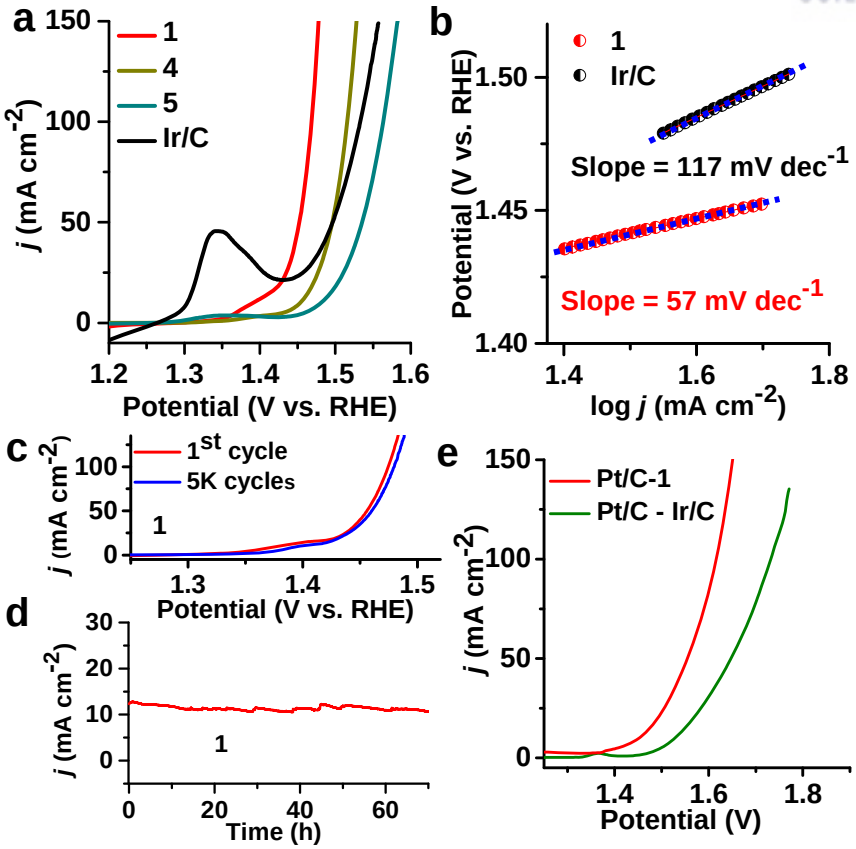

Figure 2.25. Electrochemical performance of electrocatalysts toward OER and whole cells water splitting. **(a)** Linear sweep voltammograms (LSV) curves measured in 1M KOH at a scan rate of 5 mV s^{-1}. **(b)** Tafel slope. **(c)** LSVs recorded at a scan rate of 5 mV s^{-1} during the OER before and after continuous polarization of the electrode in 1M KOH for 5000 cycles. **(d)** Chronoamperometry curves recorded in 1M KOH for 70 h. **(e)** Current density of Pt/C-**1** versus Pt/C-Ir/C for overall water splitting in 1M KOH. **1:** $Fe_3Co(PO_4)_4$@rGO, **4:** $Fe_2P_2O_7$)@rGO, **5:** ($CoFe_2O_4$)(Fe_2O_3)@rGO. Copyright 2019, Springer Nature.

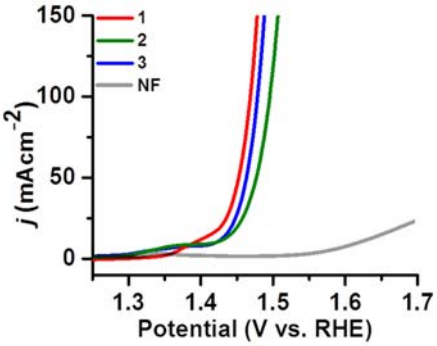

Figure 2.26. OER performance. **1:**($Fe_3Co(PO_4)_4$@rGO)@NF, **2:**($FeCo(PO_4)_2$@rGO)@NF, **3:**($Fe_2Co(PO_4)_3$@rGO)@NF and **NF** in 1M KOH aqueous solution. NF: Nickel foam. Copyright 2019, Springer Nature.

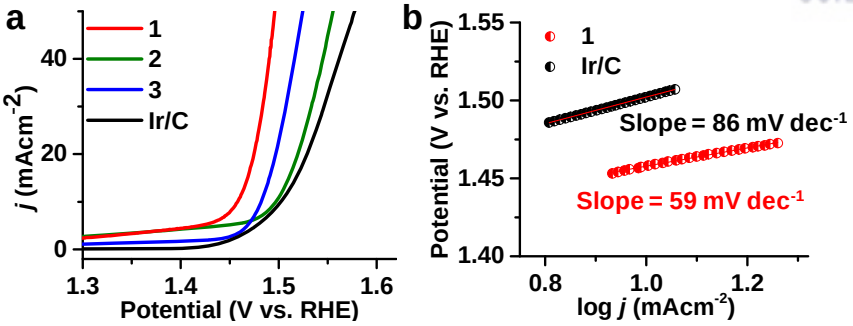

Figure 2.27. OER performance and Tafel slope. **(a)** **1:**($Fe_3Co(PO_4)_4$@rGO) @GCE, **2:**($FeCo(PO_4)_2$@rGO)@GCE, **3:**($Fe_2Co(PO_4)_3$@rGO)@GCE, and Ir/C@GCE in 1M KOH aqueous solution. GCE: Glassy carbon electrode. **(b)** OER Tafel plots of **1** and Ir/C catalysts derived from **a**. Copyright 2019, Springer Nature.

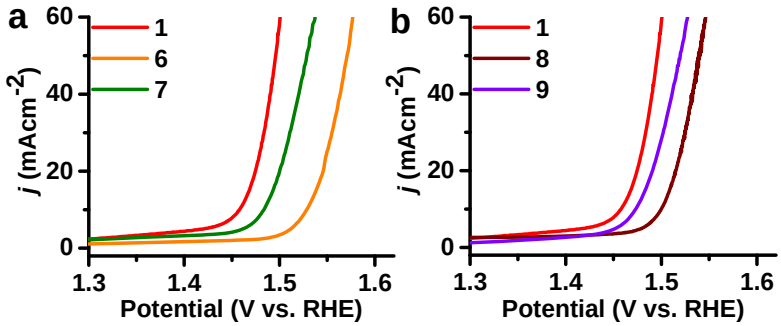

Figure 2.28. Effect of GO and red phosphorous on the OER performance. **(a)** effect of GO amounts on the OER performance. **(b)** effect of red phosphorous amounts on the OER performance. Copyright 2019, Springer Nature.

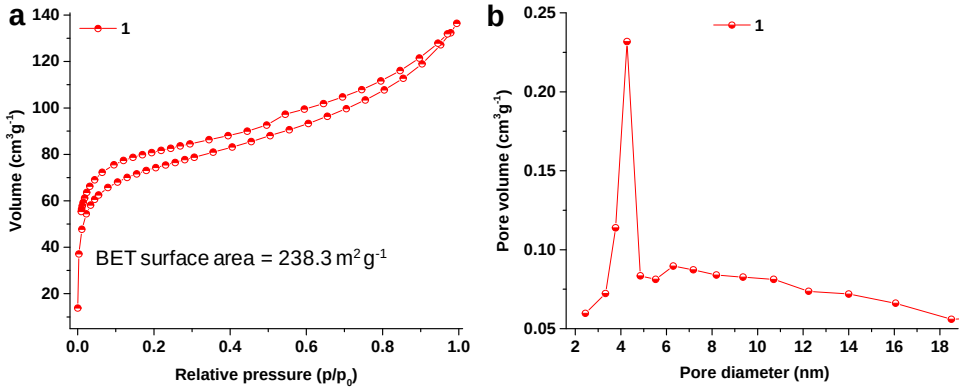

Figure 2.29. BET surface area analysis and pore size distribution. **(a)** N_2 adsorption-desorption isotherm. **(b)** pore size distribution from Barret–Joyner–Halenda (BJH) calculation. Copyright 2019, Springer Nature.

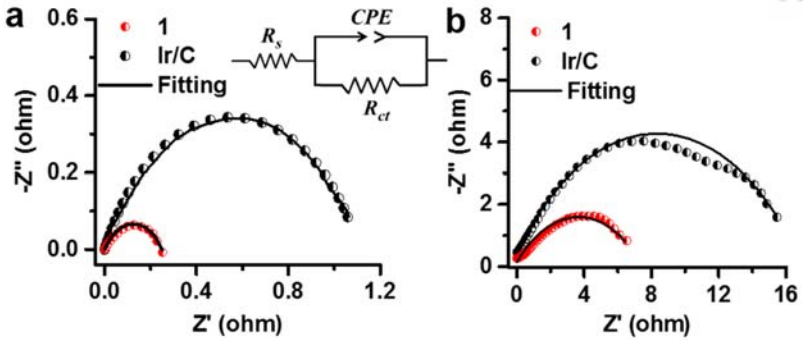

Figure 2.30. Impedance measurements. EIS Nyquist plots of **1** and Ir/C on nickel foam **(a)** and 1 and Ir/C on GCE substrate. **(b)** In the Nyquist plots, an imaginary part (–*Z*'') and a real part (*Z*') of characteristic curves are plotted as *y* axis and *x* axis, respectively. The inset is the fitting equivalent circuit for the impedance spectra. Copyright 2019, Springer Nature.

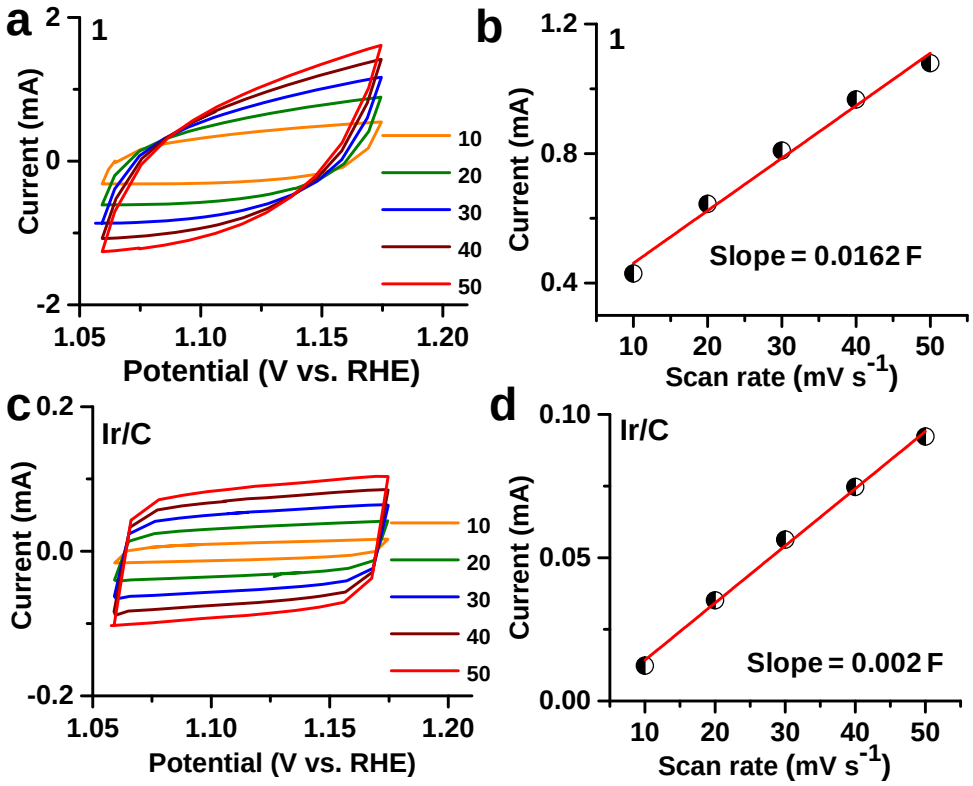

Figure 2.31. Double layer capacitance measurements. Cyclic voltammograms of **(a) 1** and **(c) Ir/C** which were recorded at different scan rates in the voltage window of 1.059 to 1.174 V versus RHE. **(b)** Scan rate dependence of the current densities of **1** and **(d) Ir/C**at 1.125 V versus RHE. Copyright 2019, Springer Nature.

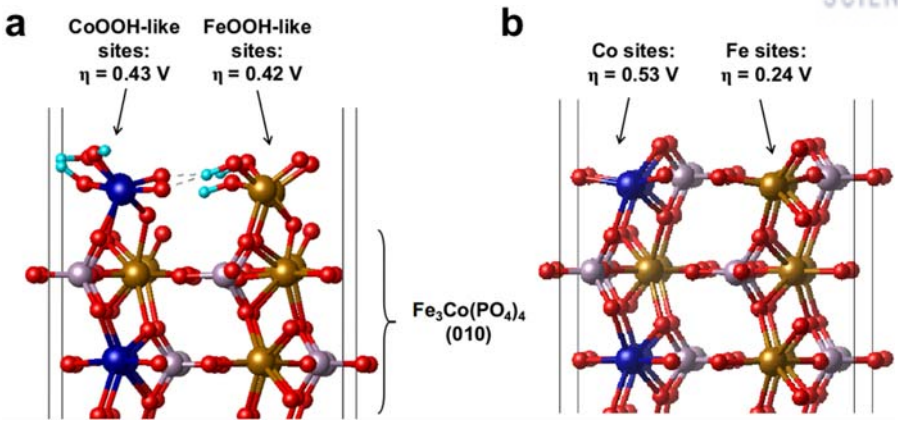

Figure 2.32. Structure and OER activity of **(a)** FeOOH- and CoOOH-like sites on top of $Fe_3Co(PO_4)_4$ (010) and **(b)** Fe and Co sites of $Fe_3Co(PO_4)_4$ (010). Fe: orange, Co: blue, O: red, H: cyan. Copyright 2019, Springer Nature.

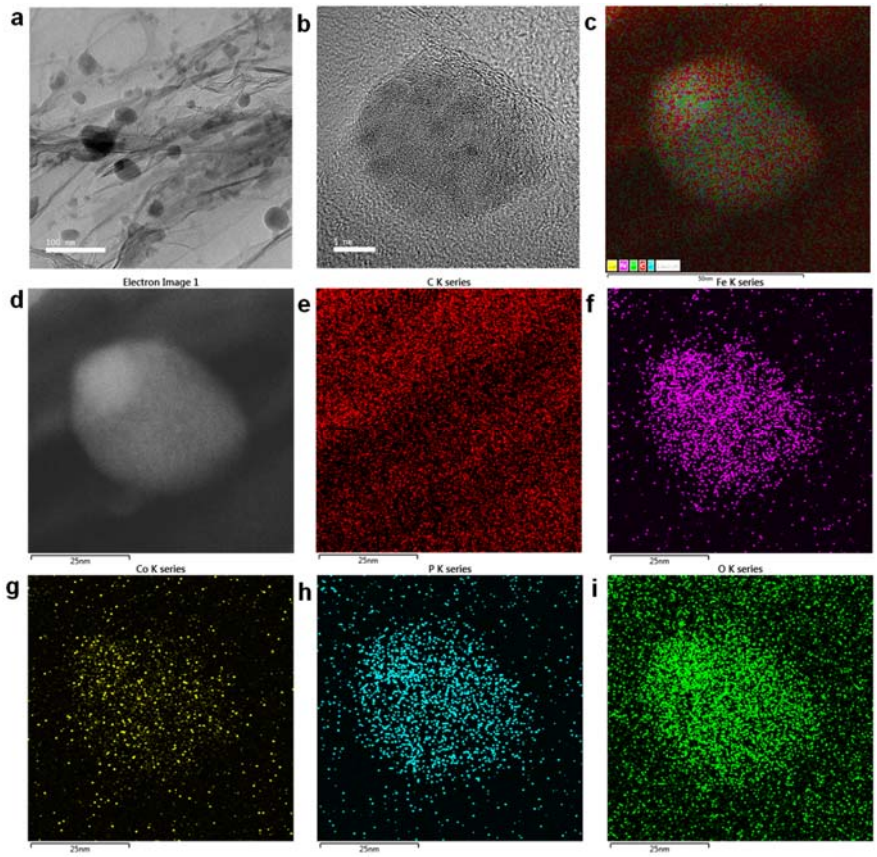

Figure 2.33. Microstructural characterization after 5k CV cycles test. **(a)** Low-magnification and **(b)** High magnification TEM images**. (c)** Overlapping image (**d-i)** STEM-HAADF image and elemental maps of C (e), Fe (f), Co (g), P (h), and O (i). Copyright 2019, Springer Nature.

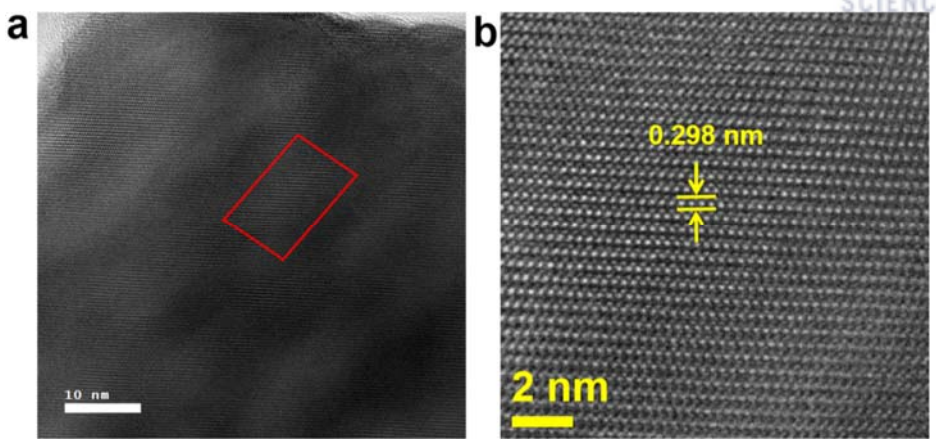

Figure 2.34. HRTEM images of **1** after 5k CV cycles test. **(a)** HRTEM image and (**b)** Magnified HRTEM image taken from the selected area in **a**. Copyright 2019, Springer Nature.

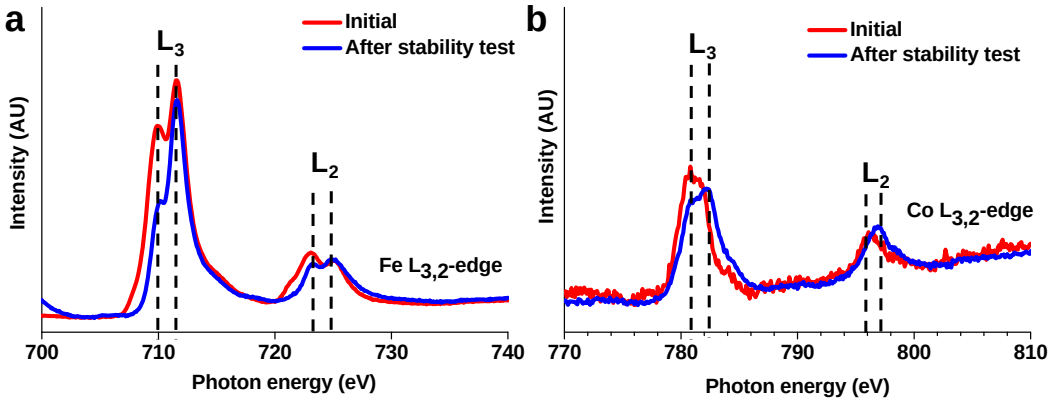

Figure 2.35. Comparison of XAS spectra of **1** before and after stability test. **(a)** Fe $L_{3,2}$-edge and (**b)** Co $L_{3,2}$-edge. After a 5000-cycle test, the Fe $L_{3,2}$-edge XAS spectra for **1** indicates that the positions of the L_3 and L_2 peaks are almost same for both Fe and Co, suggesting that not only Fe^{2+} and Fe^{3+} states but also Co^{2+} and Co^{3+} states kept almost same during the cycling. Nevertheless, though very small, $L_{3,2}$-edge XAS spectra shifted very slightly to higher energy, indicating that Fe/Co is very slightly oxidized during the OER stability test. As a result, FeO_x/CoO_x or FeOOH/CoOOH could be slightly formed during the OER process as the reviewer pointed out. However, CoOOH is expected to be a less active site because of its higher overpotential than RuO_2 (which has a much lower activity than ours)[47] and its less inductive effect of P towards Co sites in our catalyst. Phosphate sites are not active, as the reviewer addressed. However, metal sites are active. The DFT calculations demonstrate that the Fe-sites of $Fe_3Co(PO_4)_4$ are active sites with overpotential 0.24 V in excellent agreement with the experiment. Copyright 2019, Springer Nature.

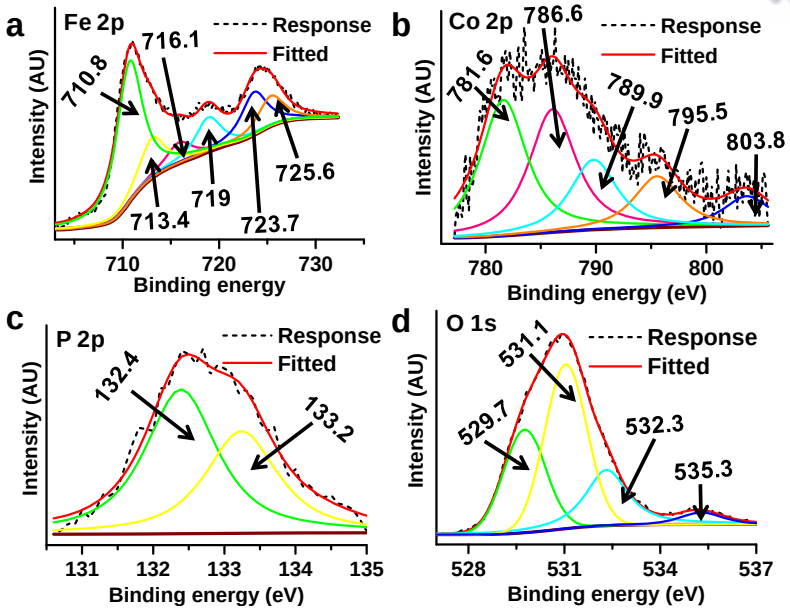

Figure 2.36. XPS core-level spectra of **1** after 5kCV cycles stability test. **(a)** Fe 2p; **(b)** Co 2p; **(c)** P 2p; **(d)** O 1s. Post-mortem analysis to investigate the surface reaction effect during the OER process shows insignificant change in peak positions of Fe, Co, P, and O. However, O 1s shows the two characteristic peak at 529.7 and 535.3 eV, which are attributed to O^{2-} ions of the lattice oxygen[48] and surface hydroxyl/water moiety[49], respectively. Copyright 2019, Springer Nature.

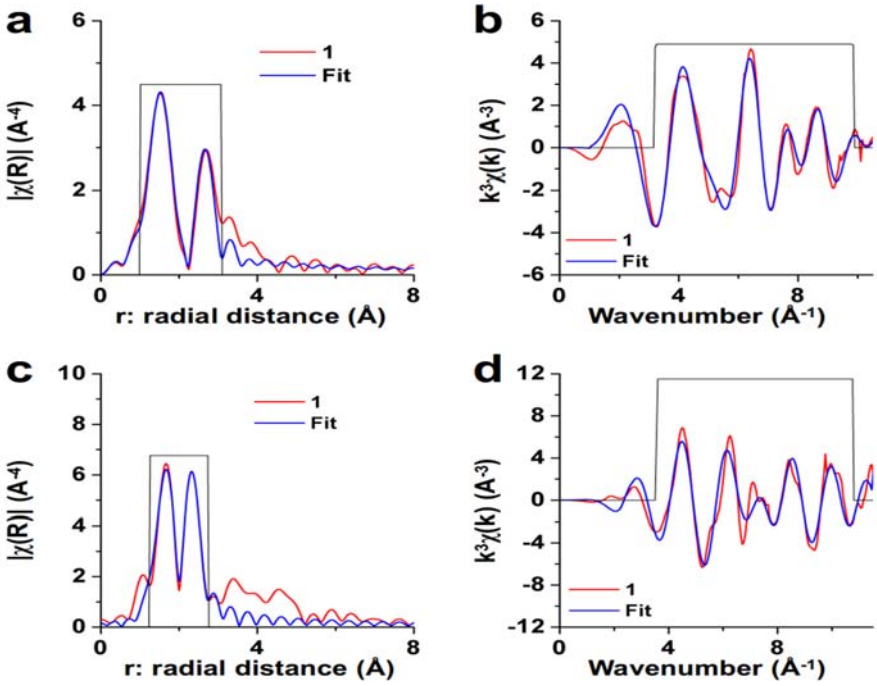

Figure 2.37. Curve-fitting analysis for **(a, b)** Fe-K edge and **(c, d)** Co K-edge EXAFS of $Fe_3Co(PO_4)_4$@rGO after OER test. **(a, c)** FT-EXAFS spectra in r-space and the corresponding least-squares fit for 1st and 2nd shells. **(b, d)** k^3 weighted EXAFS χ(k) in k-space and the corresponding least-squares fit for 1st and 2nd shells. Copyright 2019, Springer Nature.

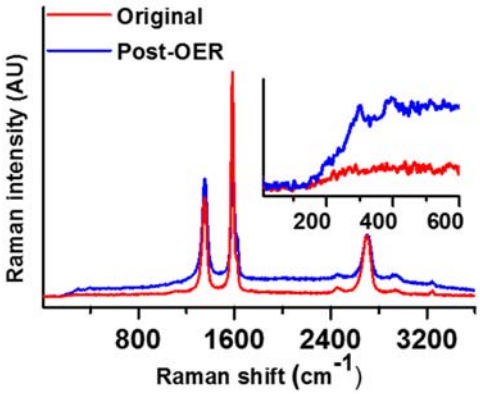

Figure 2.38. Raman analysis. Raman spectra of **1** before and after 5000 CV cycles stability test. Two small peak at 300 and 400 cm^{-1} were observed after OER stability, indicating the partly oxidization of Fe or Co on the $Fe_3Co(PO_4)_4$ surface. Copyright 2019, Springer Nature.

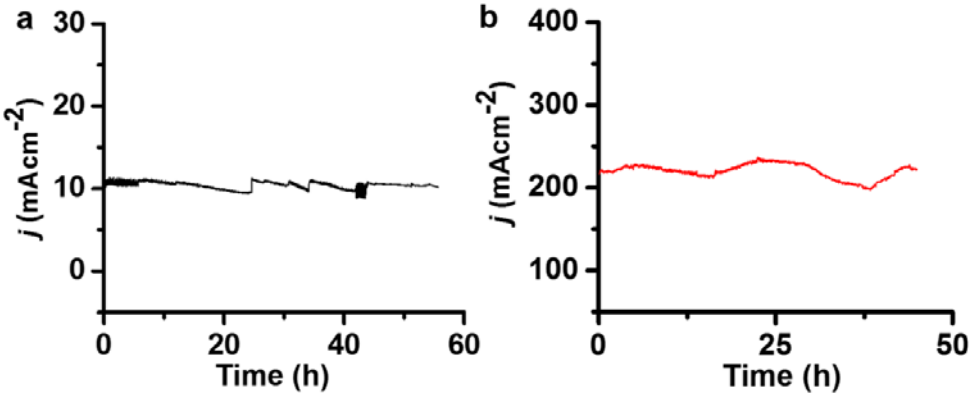

Figure 2.39. Chronoamperometric tests. **(a)** Stability test of Fe_3Co $(PO_4)_4$@rGO_catalysts loaded on glassy carbon electrode in 1M KOH. **(b**) Stability test of $Fe_3Co(PO_4)_4$@rGO catalysts loaded on nickel foam in 1M KOH at high current density. (the area of nickel foam for this stability test was $1cm^2$). Copyright 2019, Springer Nature.

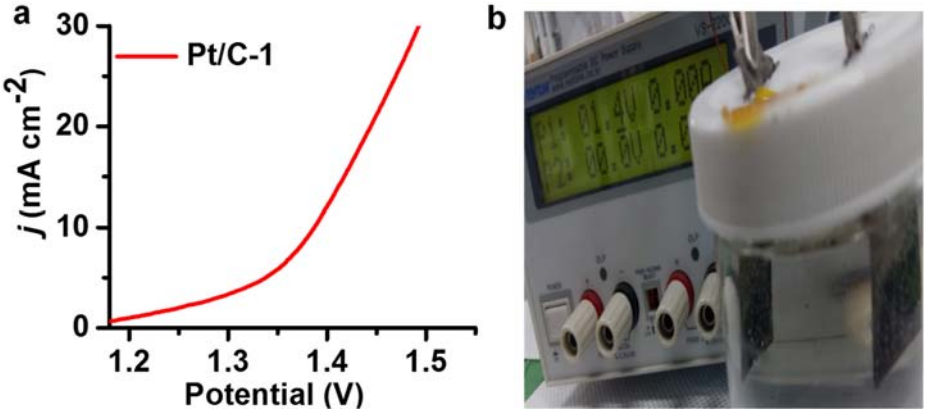

Figure 2.40. Whole water splitting. **(a)** Current density of Pt/C-**1** for overall water splitting in 6M KOH solution. The catalyst loading at cathode and anode was 5 mg cm^{-2}. **(b)** Photographic image of alkaline water splitting at 1.4 V in a two-electrode configuration for overall water splitting in 6M KOH solution, indicating the oxygen and hydrogen bubbles generation. Copyright 2019, Springer Nature.

2.5. Conclusion

In summary, we synthesized **1** and systematically evaluated their OER catalytic activities in alkaline conditions. This hybrid exhibited excellent OER catalytic activities (very low overpotential of 237 mV at high current density 100 mA cm^{-2}) and outstanding stabilities, which is superior to that of the benchmark Ir/C. The remarkable performance is attributed to the PO_4 groups which reduce free energy barrier for OER at Fe and Co sites and increase mass/charge transfer arising from defects/dislocation in the PO_4 induced mix-phase. As a full water splitting, we fabricated an electrolyzer with this hybrid catalyst in alkaline condition which afforded a current density of 10 mA cm^{-2} with ~1.45 V in 1M KOH (~1.39 V in 6M KOH). This work demonstrates the potential of large-scale structure-engineering towards low-cost, earth-abundant and high-performance water splitting for energy applications.

2.6. Reference

1. Park, J.; et al., Hollow nanoparticles as emerging electrocatalysts for renewable energy conversion reactions. *Chem. Soc. Rev.* **2018,** *47* (22), 8173-8202.
2. Roy, C.; et al., Impact of nanoparticle size and lattice oxygen on water oxidation on NiFeOxHy. *Nat. Catal.* **2018,** *1* (11), 820-829.
3. Guan, J.; et al., Water oxidation on a mononuclear manganese heterogeneous catalyst. *Nat. Catal.* **2018,** *1* (11), 870-877.
4. Tiwari, J. N.; et al., Multicomponent electrocatalyst with ultralow Pt loading and high hydrogen evolution activity. *Nat. Energy* **2018,** *3* (9), 773-782.
5. Hunter, B. M.; Gray, H. B.; Müller, A. M., Earth-Abundant Heterogeneous Water Oxidation Catalysts. *Chem. Rev.* **2016,** *116* (22), 14120-14136.
6. Tiwari, J. N.; et al., High-Performance Hydrogen Evolution by Ru Single Atoms and Nitrided-Ru Nanoparticles Implanted on N-Doped Graphitic Sheet. *Adv. Energy Mater.* **2019,** *0* (0), 1900931.
7. Suen, N.-T.; et al., Electrocatalysis for the oxygen evolution reaction: recent development and future perspectives. *Chem. Soc. Rev.* **2017,** *46* (2), 337-365.
8. Luo, J.; et al., Water photolysis at 12.3% efficiency via perovskite photovoltaics and Earth-abundant catalysts. *Science* **2014,** *345* (6204), 1593.
9. Vij, V.; et al., Nickel-Based Electrocatalysts for Energy-Related Applications: Oxygen Reduction, Oxygen Evolution, and Hydrogen Evolution Reactions. *ACS Catal.* **2017,** *7* (10), 7196-7225.
10. Fan, K.; et al., Nickel–vanadium monolayer double hydroxide for efficient electrochemical water oxidation. *Nat. Commun.* **2016,** *7*, 11981.
11. Sultan, S.; et al., Single Atoms and Clusters Based Nanomaterials for Hydrogen Evolution, Oxygen Evolution Reactions, and Full Water Splitting. *Adv. Energy Mater.* **2019,** *9* (22), 1900624.
12. Seh, Z. W.; et al., Combining theory and experiment in electrocatalysis: Insights into materials design. *Science* **2017,** *355* (6321), eaad4998.
13. Zhang, B.; et al., Homogeneously dispersed multimetal oxygen-evolving catalysts. *Science* **2016,** *352* (6283), 333.

14. Jiang, J.; et al., Highly active and durable electrocatalytic water oxidation by a NiB0.45/NiOx core-shell heterostructured nanoparticulate film. *Nano Energy* **2017,** *38*, 175-184.
15. Ravel, B.; Newville, M., ATHENA, ARTEMIS, HEPHAESTUS: data analysis for X-ray absorption spectroscopy using IFEFFIT. *J. Synchrotron Radiat.* **2005,** *12* (4), 537-541.
16. Ng, J. W. D.; et al., Gold-supported cerium-doped NiOx catalysts for water oxidation. *Nat. Energy* **2016,** *1* (5), 16053.
17. Kanan, M. W.; Nocera, D. G., In Situ Formation of an Oxygen-Evolving Catalyst in Neutral Water Containing Phosphate and Co^{+2}. *Science* **2008,** *321* (5892), 1072.
18. Yuan, C.-Z.; et al., Cobalt phosphate nanoparticles decorated with nitrogen-doped carbon layers as highly active and stable electrocatalysts for the oxygen evolution reaction. *J. Mater. Chem.A* **2016,** *4* (21), 8155-8160.
19. Liu, K.; et al., High-Performance Transition Metal Phosphide Alloy Catalyst for Oxygen Evolution Reaction. *ACS Nano* **2018,** *12* (1), 158-167.
20. Padhi, A. K.; et al., Effect of Structure on the Fe^{3+}/Fe^{2+} Redox Couple in Iron Phosphates. *J. Electrochem. Soc.* **1997,** *144* (5), 1609-1613.
21. Wen, Y.; et al., Expanded graphite as superior anode for sodium-ion batteries. *Nat. Commun.* **2014,** *5*, 4033.
22. Tiwari, J. N.; et al., High-Affinity-Assisted Nanoscale Alloys as Remarkable Bifunctional Catalyst for Alcohol Oxidation and Oxygen Reduction Reactions. *ACS Nano* **2017,** *11* (8), 7729-7735.
23. Georgakilas, V.; Perman, J. A.; Tucek, J.; Zboril, R., Broad Family of Carbon Nanoallotropes: Classification, Chemistry, and Applications of Fullerenes, Carbon Dots, Nanotubes, Graphene, Nanodiamonds, and Combined Superstructures. *Chem. Rev.* **2015,** *115* (11), 4744-4822.
24. Fei, H.; et al., General synthesis and definitive structural identification of MN_4C_4 single-atom catalysts with tunable electrocatalytic activities. *Nat. Catal.* **2018,** *1* (1), 63-72.
25. Sultan, S.; et al., Highly Efficient Oxygen Reduction Reaction Activity of Graphitic Tube Encapsulating Nitrided Co_xFe_y Alloy. *Adv. Energy Mater.* **2018,** *8* (25), 1801002.
26. Bunău, O.; Joly, Y., Self-consistent aspects of x-ray absorption calculations. *J. Phys. Condens. Matter* **2009,** *21* (34), 345501.
27. Bourke, J. D.; Chantler, C. T.; Joly, Y., FDMX: extended X-ray absorption fine structure calculations using the finite difference method. *J. Synchrotron Radiat.* **2016,** *23* (2), 551-559.
28. Cobo, S.; et al., A Janus cobalt-based catalytic material for electro-splitting of water. *Nat. Mater.* **2012,** *11*, 802.
29. Liu, W.; et al., A highly active and stable hydrogen evolution catalyst based on pyrite-structured cobalt phosphosulfide. *Nat. Commun.* **2016,** *7*, 10771.
30. Jiao, L.; Zhou, Y.-X.; Jiang, H.-L., Metal–organic framework-based CoP/reduced graphene oxide: high-performance bifunctional electrocatalyst for overall water splitting. *Chem. Sci.* **2016,** *7* (3), 1690-1695.
31. Ma, J.; et al., Polyaniline Derived N-Doped Carbon-Coated Cobalt Phosphide Nanoparticles Deposited on N-Doped Graphene as an Efficient Electrocatalyst for Hydrogen Evolution Reaction. *Small* **2017,** *14* (2), 1702895.
32. Chang, J.; Xiao, Y.; Xiao, M.; Ge, J.; Liu, C.; Xing, W., Surface Oxidized Cobalt-Phosphide Nanorods As an Advanced Oxygen Evolution Catalyst in Alkaline Solution. *ACS Catal.* **2015,** *5* (11), 6874-6878.
33. Qi, H.; Qian, C.; Liu, J., Synthesis of Uniform Double-Walled Carbon Nanotubes Using Iron Disilicide as Catalyst. *Nano Lett.* **2007,** *7* (8), 2417-2421.

34. Liu, M.; et al., Fe2P/reduced graphene oxide/Fe2P sandwich-structured nanowall arrays: a high-performance non-noble-metal electrocatalyst for hydrogen evolution. *J. Mater. Chem.A* **2017,** *5* (18), 8608-8615.
35. Zhang, Y.; Wang, W.; Li, P.; Fu, Y.; Ma, X., A simple solvothermal route to synthesize graphene-modified LiFePO4 cathode for high power lithium ion batteries. *J. Power Sources* **2012,** *210*, 47-53.
36. Nardi, K. L.; Yang, N.; Dickens, C. F.; Strickler, A. L.; Bent, S. F., Creating Highly Active Atomic Layer Deposited NiO Electrocatalysts for the Oxygen Evolution Reaction. *Adv. Energy Mater.* **2015,** *5* (17), 1500412.
37. Gao, W.; Xia, Z.; Cao, F.; Ho, J. C.; Jiang, Z.; Qu, Y., Comprehensive Understanding of the Spatial Configurations of CeO2 in NiO for the Electrocatalytic Oxygen Evolution Reaction: Embedded or Surface-Loaded. *Adv. Funct. Mater.* **2018,** *28* (11), 1706056.
38. Ye, C.; et al., One-step CVD synthesis of carbon framework wrapped Co_2P as a flexible electrocatalyst for efficient hydrogen evolution. *J. Mater. Chem.A* **2017,** *5* (17), 7791-7795.
39. Chen, P.; et al., Enhanced Catalytic Activity in Nitrogen-Anion Modified Metallic Cobalt Disulfide Porous Nanowire Arrays for Hydrogen Evolution. *ACS Catal.* **2017,** *7* (11), 7405-7411.
40. Zeng, X.; et al., Single-Atom to Single-Atom Grafting of Pt1 onto Fe-N4 Center: Pt1@Fe-N-C Multifunctional Electrocatalyst with Significantly Enhanced Properties. *Adv. Energy Mater.* **2017,** *8* (1), 1701345.
41. Huang, J.; et al., A New Member of Electrocatalysts Based on Nickel Metaphosphate Nanocrystals for Efficient Water Oxidation. *Adv. Mater.* **2017,** *30* (5), 1705045.
42. Li, D.; Baydoun, H.; Kulikowski, B.; Brock, S. L., Boosting the Catalytic Performance of Iron Phosphide Nanorods for the Oxygen Evolution Reaction by Incorporation of Manganese. *Chem. Mater.* **2017,** *29* (7), 3048-3054.
43. Hou, Y.; et al., Chorkendorff, I., Bioinspired molecular co-catalysts bonded to a silicon photocathode for solar hydrogen evolution. *Nat. Mater.* **2011,** *10*, 434.
44. Stevens, M. B.; Trang, C. D. M.; Enman, L. J.; Deng, J.; Boettcher, S. W., Reactive Fe-Sites in Ni/Fe (Oxy)hydroxide Are Responsible for Exceptional Oxygen Electrocatalysis Activity. *J. Am. Chem. Soc.* **2017,** *139* (33), 11361-11364.
45. Zhang, G.; et al., Highly Active and Stable Catalysts of Phytic Acid-Derivative Transition Metal Phosphides for Full Water Splitting. *J. Am. Chem. Soc.* **2016,** *138* (44), 14686-14693.
46. Pan, Y.; et al., Core–Shell ZIF-8@ZIF-67-Derived CoP Nanoparticle-Embedded N-Doped Carbon Nanotube Hollow Polyhedron for Efficient Overall Water Splitting. *J. Am. Chem. Soc.* **2018,** *140* (7), 2610-2618.
47. Bajdich, M.; et al., Theoretical Investigation of the Activity of Cobalt Oxides for the Electrochemical Oxidation of Water. *J. Am. Chem. Soc.* **2013,** *135* (36), 13521-13530.
48. Zhang, Y.; Savara, A.; Mullins, D. R., Ambient-Pressure XPS Studies of Reactions of Alcohols on SrTiO3(100). *J. Phys. Chem. C* **2017,** *121* (42), 23436-23445.
49. Kumar, R. A.; Babu, K. S.; Dasgupta, A.; Ramaseshan, R., Enhancing the dual magnetic and optical properties of co-doped cerium oxide nanostructures. *RSC Adv.* **2015,** *5* (125), 103465-103473.

Chapter 3

Multicomponent electrocatalyst with ultralow Pt loading and high hydrogen evolution activity

3.1. Abstract

Platinum is the most effective electrocatalyst for the hydrogen evolution reaction in acidic solutions, but its high cost limits its wide application. Therefore, it is desirable to design catalysts that only require minimal amounts of Pt to function, but that are still highly active. Here we report hydrogen production in acidic water using a multicomponent catalyst with an ultralow Pt loading (1.4 μg per electrode area (cm^2)) supported on melamine-derived graphitic tubes (GTs) that encapsulate a FeCo alloy and have Cu deposited on the inside tube walls. With a 1/80th Pt loading of a commercial 20% Pt/C catalyst, in 0.5 M H_2SO_4 the catalyst achieves a current density of 10 mA cm^{-2} at an overpotential of 18 mV, and shows a turnover frequency of 7.22 s^{-1} (96 times higher than that of the Pt/C catalyst) and long-term durability (10,000 cycles). We propose that a synergistic effect between the Pt clusters and single Pt atoms embedded in the GTs enhances the catalytic activity.

3.2. Introduction

Hydrogen has been considered as an alternative to fossil fuels because it could provide a clean renewable energy system without the associated emissions that arise from the combustion of coal, oil and natural gas.[1] Among the various methods available, hydrogen production through acidic water electrolysis shows a much higher hydrogen purity (>99.995%), faster kinetics and a higher energy efficiency[1-4] than that through alkaline water electrolysis.[2-7] Pt has been the universal choice for the acidic hydrogen evolution reaction (HER), because Pt displays a much lower overpotential and higher current density than other materials.[8-10] For cost efficiency, the development of non-precious materials[11-15] has also been in progress, but yet Pt is still the universal choice. Also, milligram Pt loadings for a high HER activity are being developed,[16-18] but an ~1μg loading for inexpensive and highly efficient hydrogen production has not yet been realized. Herein we adopt an atomic-scale engineering strategy for Pt-based catalysts with the controlled deposition of Cu, Fe and Co atoms onto/into graphitic tubes (GTs). This has led us to develop the HER catalyst in which GTs encapsulate FeCo alloy nanoparticles (NPs) with an ultrathin Cu layer inside the tube wall and have single Pt atoms embedded at the GT outer-layer and nanosized Pt clusters on the tube surface. The catalyst with only 1.4μg of Pt (per electrode area (cm^2)) loading is found to exhibit a superior HER activity with a very high turnover frequency (TOF) and both a small overpotential and stability.

3.3. Experimental Section

3.3.1. Chemicals

Melamine (99%), iron(iii) chloride (reagent grade, 97%), cobalt(ii) perchlorate hexahydrate, copper(i) chloride (reagent grade, 97 %), Nafon (5wt%) and perchloric acid were purchased from Sigma-Aldrich. Benchmark 20wt% Pt/C (commercial) catalyst and 20wt% Ir/C (commercial) were purchased from Johnson Matthey and Premetek, respectively. All the chemicals were of analytical grade and used as received without further purification, unless otherwise specified.

3.3.2. Synthetic procedure of GT-1, GT-2, GT-3, GT-4 and GT-5

In a typical synthesis, different weight ratios of the precursors (cobalt perchlorate hexahydrate: iron chloride: copper chloride) were used with 1.0 g of melamine. The precursor's weight ratios for alloys 1, 2 and 3 were 0.3:0.1:0.1 g, 0.1:0.2:0.1 g and 0.1:0.1:0.2 g, respectively. Then, all resulting mixtures were poured into 40 ml of distilled water and sonicated for 12 h to obtain the homogeneous mixture, dried at 70 °C and ground thoroughly. The ground powder was heated at 750 °C for 3 h with a temperature ramping rate of 5 °C min^{-1} in the presence of N_2 atmosphere. Finally, the obtained products were immersed in 0.1M $HClO_4$ for 12 h, filtered and washed with ethanol, and then dried at 70 °C. For the synthesis of GT-4 (0.3:0.1:0.0 g), the whole procedure was the same as that for GT-1 but in the absence of the copper precursor. For the synthesis of GT-5, the whole procedure was the same as that for GT-4, but the ratio was 0.1:0.2:0.0 g.

3.3.3. Electrochemical Pt deposition

The Pt loadings on the synthesized GT-1, GT-2, GT-3, GT-4, GT-5, carbon black and GT samples were carried out with a three-electrode system using a VSP instrument (Bio-Logic Science Instruments). The working electrode was a glassy carbon electrode (GCE, geometric area of 0.196 cm^2). A Pt wire and SCE served as the counter and reference electrodes, respectively. The synthesized GT-n (n=1- 4) samples were attached to the GCE: 10 mg of each sample and 80 µl of 5 wt% Nafion solution were dispersed in 1120 µl of a water/ethanol (1:3 v/v) mixed solvent and sonicated for 30 min, and then 6.6 µl of the homogeneous ink was dropped onto the GCE (0.28 mg cm^{-2}). The dried hybrid catalysts/GCE were used as working electrodes. For the platinum source, 10 ml of a chloroplatinic acid aqueous solution (1mg ml^{-1}) was poured into 60 ml of a 0.1M HClO4 electrolyte. The deposition process was carried out by 15 CV cycles with a voltage range from + 0.3 to -0.3 V (vs the reversible hydrogen electrode (RHE)) at a scan rate of 100 mVs^{-1} (Figure 3.1). During the Pt deposition by CV cycles, the Pt and hydrogen were attached cathodically first and then a few Pt atoms were dissolved anodically, which enabled Pt-size control.

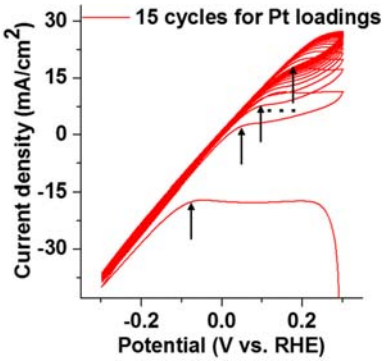

Figure 3.1. Cyclic voltammetry (CV) for Pt deposition on the catalyst surface. The arrow represents the CV curve shifts with respect to Pt loadings. Scan rate 100 mV/s. Copyright 2018, Springer Nature.

3.3.4. Electrochemical device fabrication

Two separate electrodes were prepared to demonstrate the acidic water splitting. For the anode, a commercial 20 wt% Ir/C was coated on graphite paper (2 cm×2 cm) via a drop-casting method. The mass loading of the Ir/C catalyst was ~280 μg cm^{-2}, which was controlled by selecting the proper amount of Ir/C catalyst ink by pipette. Catalyst inks were prepared by mixing 10 mg of Ir/C catalysts with 1120 μl of water/ethanol (1:3 v/v) and 80 μl of 5 wt% Nafion solution. The catalyst inks were sonicated in a hypersonicator for 60 min to make the homogeneous ink. For the cathode, the GT-1 catalyst ink was coated on graphite paper (2 cm×2 cm) via the drop-casting method. Catalyst inks were prepared by a method similar to that for Ir/C. Then, 134.4 μl of the homogeneous ink was dropped and dispersed onto the graphite paper (0.28 mg cm^{-2}). Pt was then electrodeposited on the GT-1/graphite substrate by 15 CV cycles. After that, both electrodes were dried in a vacuum oven and then integrated into a two-electrode set-up.

3.3.5. Electrochemical testing

The same three-electrode system was used for HER activity and durability measurements. For the HER, graphite rods were used instead of Pt wires as a counter electrode. The linear sweep voltammogram tests were performed at a scan rate of 2 mVs^{-1}, which were measured in the range of 0.1 to −0.6 V vs saturated calomel electrode (SCE) in H_2-saturated 0.1M $HClO_4$ electrolyte. The durability tests were carried out by repeating the potential scan from 0.1 to -0.5 V (vs SCE) at a sweep rate of 100 mVs^{-1} with 10,000 CV cycles. Chronoamperometric characterization was carried out in H_2-saturated 0.1M $HClO_4$ solution at a potential of −0.402 V (vs SCE) for 6 h. The working electrode was rotated at 1500 revolutions per minute to remove the H_2 bubbles produced at the surface of the catalyst. For the durability test, the catalyst on the working electrode was coated with a 0.2 wt% Nafion solution. All the potentials were determined with respect to RHE using the equation 3.1:

$$E(RHE) = E(SCE) + 0.241V + 0.0591pH \quad (3.1)$$

The Tafel slopes were determined by fitting the linear portion of the plot starting from the onset potential (to the endpoint which does not significantly deviate from the slope line). The Tafel slopes were calculated by fitting to the Tafel equation 3.2:

$$\eta = b j \log c \qquad 3.2$$

$$j_0 = e^{(-2.303\frac{c}{b})} \qquad 3.3$$

where b is the Tafel slope, j is the current density and c is the intercept relative to j_0. The exchange current density (j_0) value is calculated by the formula 3.3:

The EIS measurements were performed over a frequency range of 1Hz to ~250 kHz at a 5 mV perturbation amplitude. Nyquist plots of the catalysts in 0.1M $HClO_4$ solution were obtained at a potential of −0.301 V (vs SCE). The spectra were plotted after solution resistance subtraction.

3.3.6. TOF calculation

The TOF per metal (Pt-based) site in the Pt-GT-1 catalyst for the HER is calculated by the equation 3.4:

$$\text{TOF} = \frac{\text{Total number of hydrogen turnover /geometric area (cm}^2\text{)}}{\text{Number of active sites/ geometric area (cm}^2\text{)}} \qquad (3.4)$$

The total number of hydrogen turnovers was calculated from the current density using the formula:[19-20]

$$\text{Number of hydrogen} = \left(j\frac{\text{mA}}{\text{cm}^2}\right)\left(\frac{1\frac{\text{C}}{\text{S}}}{1000\ \text{mA}}\right)\left(\frac{1\ \text{mole}\ e^-}{96485.3\text{C}}\right)\left(\frac{1\ \text{mole}\ \text{H}_2}{2\ \text{mole}\ \text{e}^-}\right)\left(\frac{6.022\ \text{x}\ 10^{23}\ \text{molecules}\ \text{H}_2}{1\ \text{mole}\ \text{H}_2}\right)$$

$$= 3.12\ \text{x}\ 10^{15}\left(\frac{\text{H}_2/\text{s}}{\text{cm}^2}\right)\ \text{per}\left(\frac{\text{mA}}{\text{cm}^2}\right)$$

The number of Pt metal ions was determined from the ICP-AES measurement (0.5 wt%).

Accordingly, the active site density based on bulk Pt is

$$\left(\frac{0.5\ \text{mg}}{100\ \text{mg}}\right)\text{x}\left(\frac{0.28\ \text{mg}}{\text{cm}^2}\right)\text{x}\left(\frac{1\ \text{mmole}}{195.1\ \text{mg}}\right)\text{x}\ 6.022\ \text{x}\ 10^{20}\left(\frac{\text{sites}}{\text{mmole}}\right) = 4.32\ \text{x}\ 10^{15}\ \text{sites/cm}^2$$

At an overpotential of 0.066 V, the HER current density is 10 mA/cm^2, and the Pt based TOF value of catalysts was calculated to be

$$\frac{3.12\ \text{x}\ 10^{15}\left(\frac{\text{H}_2/\text{s}}{\text{cm}^2}\right)\ \text{per}\left(\frac{\text{mA}}{\text{cm}^2}\right)\text{x}\ 10\left(\frac{\text{mA}}{\text{cm}^2}\right)}{4.32\ \text{x}\ 10^{15}\ \text{sites/cm}^2} = 7.22\ \text{s}^{-1}$$

3.3.7. Characterization

Field-emission SEM (FESEM) measurements were carried out on Nanonova 230 (FEI, USA). transmission electron microscopy (TEM) and high-resolution TEM (HRTEM) were performed on JEM-2100F with an acceleration voltage of 200 kV. TEM samples were prepared by placing a drop of the colloidal solution on a carbon-coated nickel grid and dried overnight at room temperature. To observe single Pt atoms on the GTs, high-angle annular-dark-field scanning-TEM (HAADF–STEM) images

(taken through the GT surface) were obtained using a C_s (image)-corrected TEM (FEI Titan^3 G2 60-300). The HAADF, with a scattering intensity roughly proportional to Z^2 in a Z-contrast image gives a strong bright signal for Pt (of high Z value), but not for C, N, Fe, Co and Cu (of low Z values). Thus, all the sub-nanometer-sized strong bright spots correspond to single Pt elements or Pt nanoclusters because such small bright spots can hardly come from C, N, Co, Fe and Cu. Then, if the surface is flat uniform graphene, the Pt images could be seen clearly. However, somewhat broad/smooth bright regions could appear due to the highly scattered electrons on rugged and non-uniform surfaces of thick carbon layers of the GT, which include N atoms and Pt atoms/clusters, in that the scattering electron intensity is proportional to the thickness of the sample or the number of element atoms as well as Z^2. Here HAADF–STEM was performed from 80 to 200 kV at various imaging conditions to observe clear Pt atoms on the GT surface. The optimal signal-to-noise ratio of Pt atoms was achieved using a probe convergent semi-angle of 26.6 mrad, condenser aperture of 70 mm, spot size 8 and camera length of 185 mm at 200 kV. Further electron energy loss spectroscopy (EELS) and Energy-dispersive X-ray spectroscopy (EDX) analyses were also made in STEM mode using a nanobeam. The Co, Fe and Cu elements are detectable in our EELS set-up, but they were not seen in our EELS measurements, which indicates their absence outside the GTs. The Pt elements were not observable from our EELS because the Pt energy-loss region is beyond our detection limit. The images of single Pt atoms and Pt clusters were clearly seen from HAADF–STEM, whereas the Pt clusters were confirmed from EDX. XRD measurements were performed on a D8 advance (Bruker). FT infrared spectroscopy (FT-IR) was measured on a 670-IR (Agilent) with an attenuated total reflection detector. Inductively coupled plasma–mass spectrometry (ICP–MS) was carried out on ELAN DRC-II (Perkin Elmer). X-ray photoelectron spectroscopy (XPS) was measured on K-alpha (Thermo Fisher). Confocal μ-Raman measurements were carried out on α300R (WITec). Brunauer–Emmett– Teller (BET) measurements were carried out on BELSORP-miniII (BEL Japan). X-ray absorption fine spectroscopy (EXAFS) data of the prepared catalysts were collected in the transmission mode using ionization detectors (Oxford) at the Pohang Accelerator Laboratory (PAL). The X-ray absorption spectra (XAS) for the Pt L edge, Fe K edge and Co K edge were acquired at room temperature using beamline 6D of PAL, where their X-ray energies from the EXAFS analysis were calibrated with Pt foil, Fe foil and Co foil, respectively. Background subtraction, normalizing and FT were done by standard procedures with ATHENA program. The extracted EXAFS signal, $\chi(r)$ and $k^3\chi(k)$ were analyzed for all three metals. The selected k ranges for Pt–GT-1, Pt foil and Pt–C in plotting the Pt L-edge graphs were 2.6–9, 2.5–18 and 3.0–12.6, respectively, and their selected r ranges were 1.8–5.5, 1.6–4.4 and 1.0–3.2, respectively. In the case of both the Fe and Co K edges, the k ranges were selected from 2 to 12 and the r ranges were from 1.7 to 2.8. The Artemis program was used for the EXAFS fitting.[21]

3.4. Results and Discussion

3.4.1. Catalyst synthesis

We synthesized GTs that encapsulate FeCo alloys with Cu deposited on the inner tube walls; then, hyperlow Pt loadings were deposited on the GT surfaces (Pt–GT–FeCo/Cu). First, to optimize the composition of the alloys, five different alloys n (n=1-5) were considered with weight ratios of $FeCl_3$: $Co(ClO_4)_2 \cdot 6H_2O$: CuCl being 0.1:0.3:0.1 g for alloy 1, 0.2:0.1:0.1 g for alloy 2, 0.1:0.1:0.2 g for alloy 3, 0.1:0.3:0.0 g for alloy 4 and 0.1:0.2:0.0 g for alloy 5. A mixture of melamine (1 g) with each FeCo/Cu alloy is used to form GT-n (n=1–5) through heating at 750 °C in N_2 gas atmosphere, followed by acid, ethanol and deionized (DI) water treatments of the product to leach away any accessible debris or species (Figure 3.2a, Methods, Figs 3.3-3.6 and Table 3.1). Second, Pt is electrochemically deposited on the hybrid surfaces of GT-n to form Pt–GT-n by cyclic voltammetry (CV) using $H_2PtCl_6 \cdot 6H_2O$–$HClO_4$ as an electrolyte solution (Figures 3.1 and 3.2a) and the characterization made (Figure 3.2b-j). During the cyclic process, CV acts as an alternating redox process, which involves both deposition and dissolution processes, both critical to the formation of Pt particles ($Pt^{2+} + 2e^- \rightarrow Pt^0$) on the hybrid materials. GT-1 and Pt–GT-1 were found to have the optimized Fe:Co:Cu ratio as they exhibited the best catalytic activity for the HER at around 15 CV cycles in an acidic electrolyte (0.1M HClO4). Therefore, these hybrids are further discussed in detail (Charge transfer, H-adsorption free energy, and theoretical understanding of the catalytic activity sections).

3.4.2. Scanning and transmission electron microscopy analysis

GT-1 and Pt-GT-1: The SEM image (Figure 3.2b) shows that GTs are formed with NPs after heating the mixed powder sample. The TEM image reveals that GTs have bamboo-like structures with encapsulated NPs (Figure 3.2c). The GT diameters have a wide distribution, but most of them range from 50 to 300 nm with the outer GT layer thickness of ~5–10 nm (Figure 3.2d). However, a significant amount of graphitic shells that comprised 1–3 layers are also present (Figure 3.2j). EDX elemental mapping indicates that the bamboo node-shape morphology composed of C and N is attributed to a polymerized carbon nitride formed after the melamine polymerization at 750 °C (Figure 3.3). The HRTEM images (Figure 3.2c, e) of the encapsulated alloy NPs reveal that the lattice spacing of the plane is 0.201nm, which agrees well with the spacing of the (110) planes of Fe_3Co_7 alloys (JCPDS 00-050-0795), and is further confirmed by a Fourier transform (FT) of the extended X-ray absorption fine structure (FT-EXAFS) and X-ray diffractometer (XRD) analyses (Figure 3.15a). In addition, the HRTEM image of the encapsulated NP's edge often shows the lattice plane with a spacing of 0.208 nm, which corresponds to that of the (100) plane of Cu without any Fe or Co (Figure 3.2 e). The line profiles for Co, Fe and Cu in the HAADF–STEM image (Figure 3.2f) show the population of each metal depending on position along the diameter. The stronger signal for Co than Fe indicates more Co atoms, and a faint Cu signal in the alloy reveals a tiny amount of Cu atoms, whereas a sharp thin peak signal for Cu on the inner wall of a GT indicates that the Cu NPs and/or layers are spread on some parts of the

inner tube wall, consistent with the HAADF–STEM, TEM and HRTEM images of Figure 1g–j. These thin Cu layers (which are highly conductive) play a role in the conduction enhancement (Table 3.2), because the absence of Cu is found to reduce the HER activity significantly. The HRTEM images show that the morphology of bamboo-like GTs is well maintained even after 15 CV cycles of Pt dosage on the leached products and the alloy NPs are inside GTs (Figure 3.2g-i). Pt NPs outside the GTs and Fe_3Co_7 NPs under the Cu layers inside the GTs are observed by HRTEM images (Figure 3.2h, i). The 0.227, 0.208 and 0.336nm spacing's observed in the HRTEM images of Pt–GT-1 correspond to Pt (111), Cu (100) and GT, respectively (Figure 3.2i).

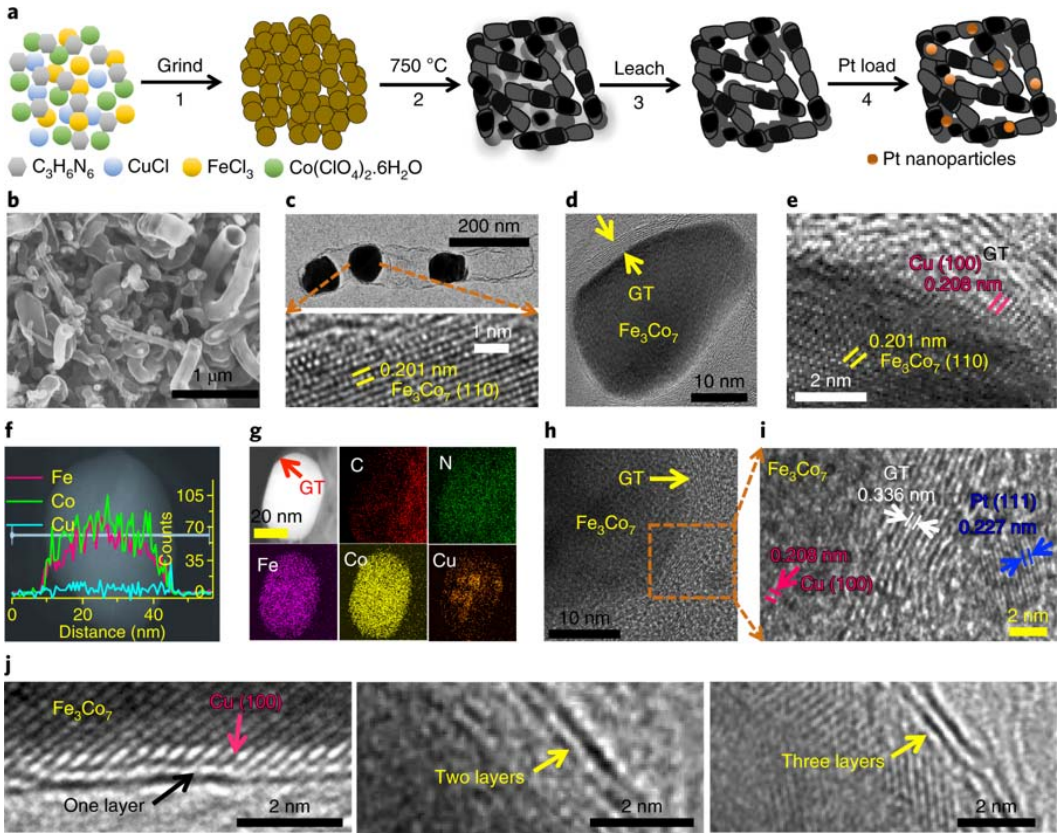

Figure 3.2. Synthetic procedure and physical characterization. **(a)** Synthetic procedure: **(1)** grind the sample of melamine, $FeCl_3$, $Co(ClO_4)_2{\cdot}6H_2O$ and CuCl, **(2)** heat**, (3)** leach with acid and wash with water and ethanol, and **(4)** load the Pt electrochemically. (**b**) SEM image of the leached sample of bamboo-node shaped GTs grown with the aid of the enclosed alloy NPs**. (c)** TEM images of a GT enclosing alloy NPs and HRTEM image of the alloy (corresponding to Fe_3Co_7 inside a GT. **(d)** TEM image of a cross section of a GT enclosing an alloy NP. **(e)** The HRTEM image shows the presence of Fe_3Co_7 and Cu inside the GT. **(f)** HAADF–STEM image and line scan profiles inside a GT of GT-1 (Cu peaks appear on the inside wall of the GT). **(g)** The HAADF image and individual element maps show a cross-section of the GT (inside of which a Fe_3Co_7 alloy NP is enclosed and Cu is spread on the inside wall) in the Pt–GT-1 catalyst. **(h, i)** TEM image of a Pt NP on a GT surface of Pt–GT-1 **(h)** and an enlarged HRTEM image (**i**) HRTEM images of one, two and three layers of GTs in Pt–GT-1 that are much less populated than multilayers. Copyright 2018 Springer Nature

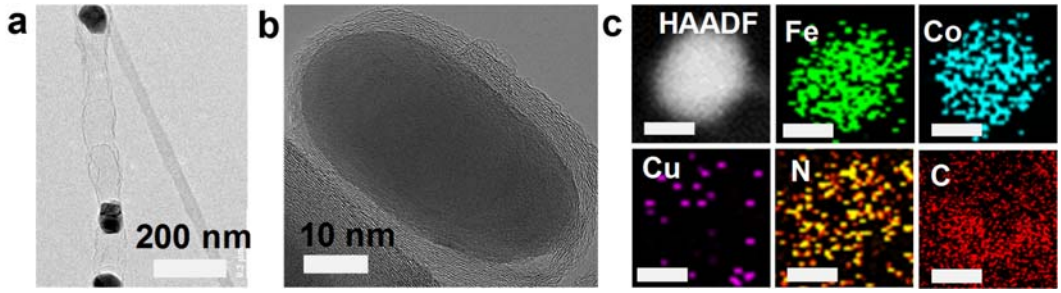

Figure 3.3. TEM images, HAADF-STEM and TEM-EDX mappings of GT-1. **(a)** TEM image, **(b)** HRTEM image and **(c)** HAADF-STEM image and individual element maps of Fe, Co, Cu, N and C in a part of the GT-1 catalyst. Scale bar 50 nm. Copyright 2018, Springer Nature.

GT-2 and GT-3: The SEM images display the tubular morphology of GT-2 and GT-3 samples (Figure 3.4a, b). These large and small GTs have diameters in a range of 50 nm to 400 nm. The TEM images of the tubular morphology of GT-2 and the tubular with sheet-like structures of GT-3 samples exhibited that the metal particles of varying sizes were encapsulated in GTs which look like bamboo structure (Figures 3.5a, b and 3.6a, d). HRTEM image of individual NP in GT-2 shows that the lattice spacing of the planes is ~0.202 nm, matching well with the interplanar spacing of Fe_7Co_3 (110) planes (JCPDS 00-048-1816; Figure 3.5b). According to line scans, the GT-2 hybrid exhibited a higher concentration of Fe atoms than Co and Cu atoms (Figure 3.5c, d). However, the concentration of Cu atoms is almost insignificant, indicating that Fe shows alloying with Co. The EDX mapping and HAADF-STEM image show the presence of Fe, Co, and Cu in GT-2, while most Cu atoms are the inside wall of GTs (Figure 3.5e). The line scan profile of GT-3 exhibited high concentrations of Fe and Co atoms, much higher than that of Cu atoms (Figure 3.6b, c), because most of Cu atoms are on nanosheets/GTs. These observations are consistent with EDX mapping and HAADF-STEM images. The elemental EDX mapping image of metal particles showed the presence of Cu, Fe, and Co in GT3 hybrid in which Cu NPs/layers are spread over the inner and outer walls of GTs (Figure 3.6e, f).

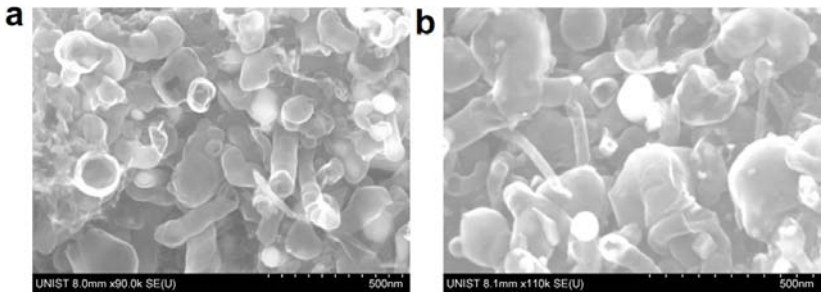

Figure 3.4. Plane-view SEM images. **(a)** GT-2 and **(b)** GT-3. Copyright 2018, Springer Nature.

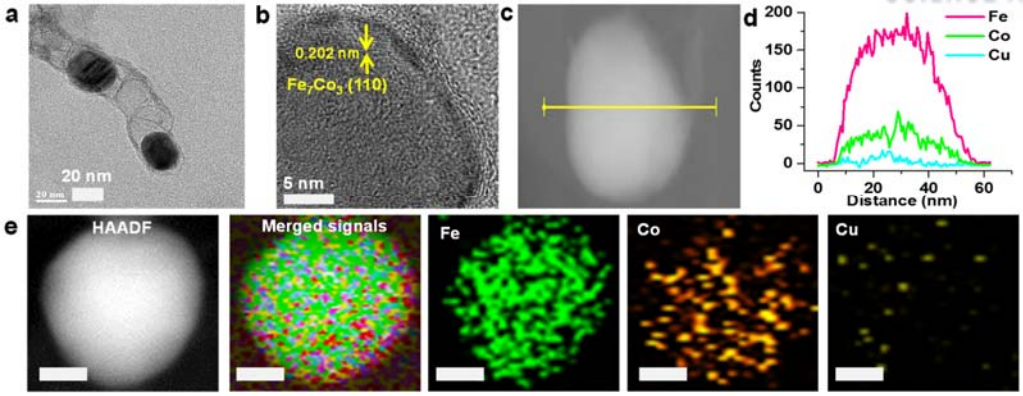

Figure 3.5. TEM images, EDX line scan, HAADF-STEM and TEM-EDX analysis of GT-2. **(a, b)** TEM, HRTEM images, and **(c)** STEM-HAADF image of GT-**2**. **(d)** line profiles image **(e)** HAADF–STEM image element maps of Fe, Co, and Cu in a part of the GT-**2** catalyst. Scale bar: 20 nm. Copyright 2018, Springer Nature.

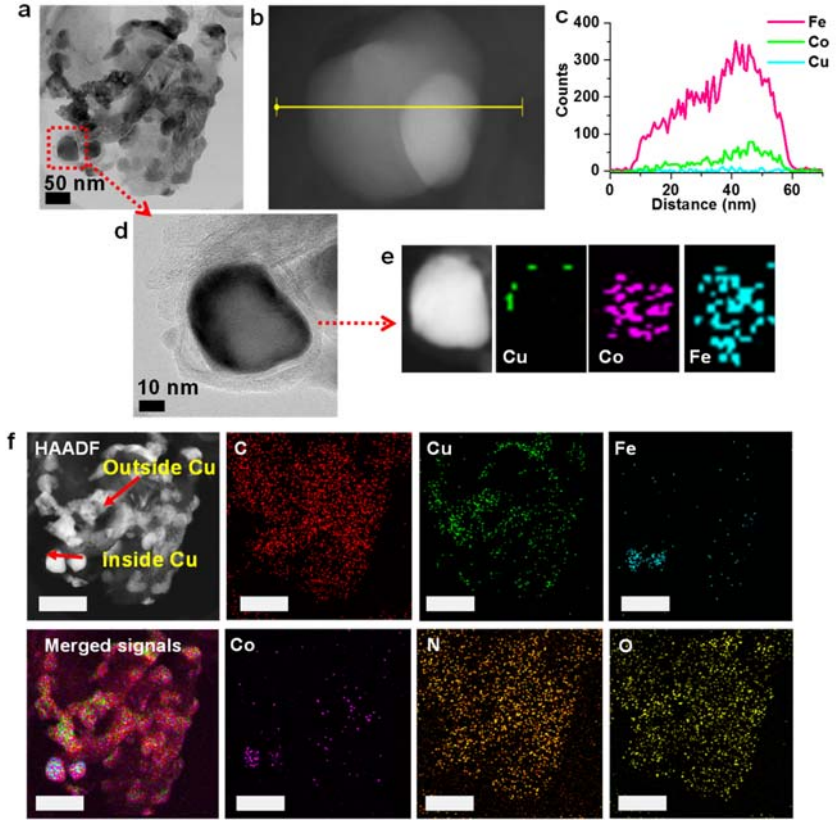

Figure 3.6 TEM images, EDX line scan, HAADF-STEM, and TEM-EDX analysis of GT-3. **(a)** TEM image and **(b)** STEM-HAADF image of GT-**3**. **(c)** Line profile of elemental compositions measured by EDX along the line shown on image **(b)** The line map curve shows the presence of Fe, Co and a trace amount of Cu atoms in a single NP inside the GT. **(b)** HRTEM image. (**e)** HAADF–STEM image element maps of the GT-**3** catalyst. **(f)** Large area HAADF–STEM image and the total and individual element maps of C, Fe, Co, Cu, N, and O in a part of the GT-**3** catalyst. Scale bar: 100 nm. Copyright 2018, Springer Nature.

Table 3.1. XPS composition analysis. Atomic percentage obtained from XPS analysis of catalysts. Copyright 2018, Springer Nature.

Catalyst	Fe (atomic %)	Co (atomic %))	Cu (atomic %)
GT-1	0.29	0.61	0.27
GT-2	0.69	0.30	0.32
GT-3	0.90	0.48	3.10

Table 3.2. Electrical conductivity. Conductivity of Cu, Co, and Fe metals at 20 ^{0}C. Copyright 2018, Springer Nature.

Metals	Cu	Co	Fe
Conductivity (S/m)	5.98×10^7	1.60×10^7	1.01×10^7

3.4.3. X-ray absorption fine structure analysis

X-ray absorption near edge structure (XANES) analyses were made for the hybrid materials, reference Pt foil and the Pt/C commercial catalyst (Figure 3.7). The EXAFS analysis shows a Pt–Pt contribution at a distance of 2.77 Å (Table 3.3). The coordination number (10.5), lower than that of bulk Pt (12.0), suggests small Pt NP or ultrathin layers. The significant peak at ~1.5 Å reflects Pt–N/C bond lengths that correspond to the calculated values of ~1.95 Å. The FT radial structure functions for Pt–GT-1 are explained with the EXAFS analysis (the corresponding atomic structure parameters are given in Tables 3.3 and 3.4).

The oscillating phase in the k-space of Pt NPs from Pt–GT-1 is different from those observed from Pt foil and Pt/C (Figure 3.8).[22] The FT-EXAFS spectra for Co, Fe and Cu K edges, before and after Pt loadings, display the intensity change in the EXAFS signals (Figure 3.9 and 3.10) due to the decrease of the metal coordination numbers, whereas the induced atomic relocation is caused by the minute dissolution of Co, Fe and Cu around the tube mouth during the electrochemical deposition of Pt. However, even these minutely dissoluted Co, Fe and Cu NPs outside the GTs are washed away in acid electrolytes, whereas the Co, Fe and Cu NPs inside the GTs are well preserved.

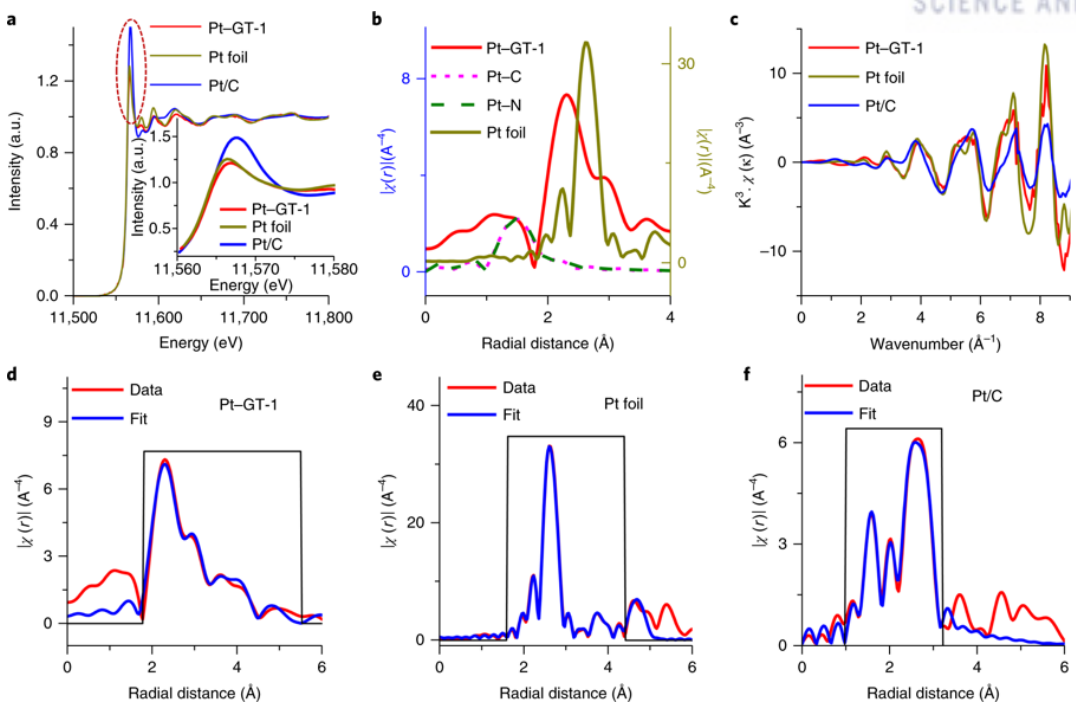

Figure 3.7. X-ray absorption spectra at the Pt L3 edge. **(a)** Normalized XANES spectra (a.u. arbitrary unit). **(b)** FT-EXAFS region for the local structure of Pt, which shows that the main Pt–Pt peak at 2.6 Å for Pt foil (which corresponds to a Pt–Pt distance of 2.76 Å by fitting the data in Artemis) splits into 2.3 and 2.9 Å for Pt–GT-1 (which corresponds to a Pt–Pt distance of 2.77 Å in Artemis), whereas the significant peak at ~1.5 Å reflects Pt–N/C bond lengths (~1.95 Å). **(c)** EXAFS $\chi(k)$ signals in k-space. **(d–f)** FT-EXAFS spectra in r-space and the corresponding least-squares fit (black solid line) for the first shell. The white-line intensity of the Pt L3 edge for Pt–GT-1 (inset in Figure 3.7a) closely resembles that for Pt foil[23-25], which indicates the metallic state of the Pt species in Pt–GT-1. The Pt/C exhibits a relatively strong white-line intensity, which shows a significant degree of Pt oxidation[26]. The peak around ~1.58 Å in Pt/C reflects Pt bonded to light elements (Pt–C/O), whereas the double peaks between 2 and 3 Å in all cases exhibit Pt–Pt scattering in the coordination sphere[27]. From the FT-EXAFS signals, the Pt–Pt bond distance for Pt–GT-**1** closely resembles that for Pt foil, but the Pt intensity for Pt–GT-**1** is lower than that for Pt foil, which indicates an increased disorder in the Pt–Pt bond length, but with the metallic Pt feature still maintained. Copyright 2018, Springer Nature.

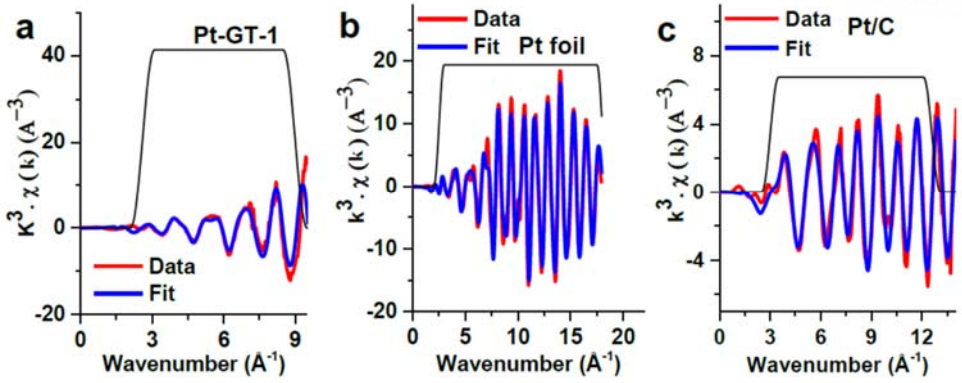

Figure 3.8. EXAFS χ(k) signals of Pt-GT-1, Pt foil and Pt/C. **(a-c)** EXAFS χ(k) signals in k-space and the corresponding least-squares fit (black solid line) for 1st shell. Copyright 2018, Springer Nature.

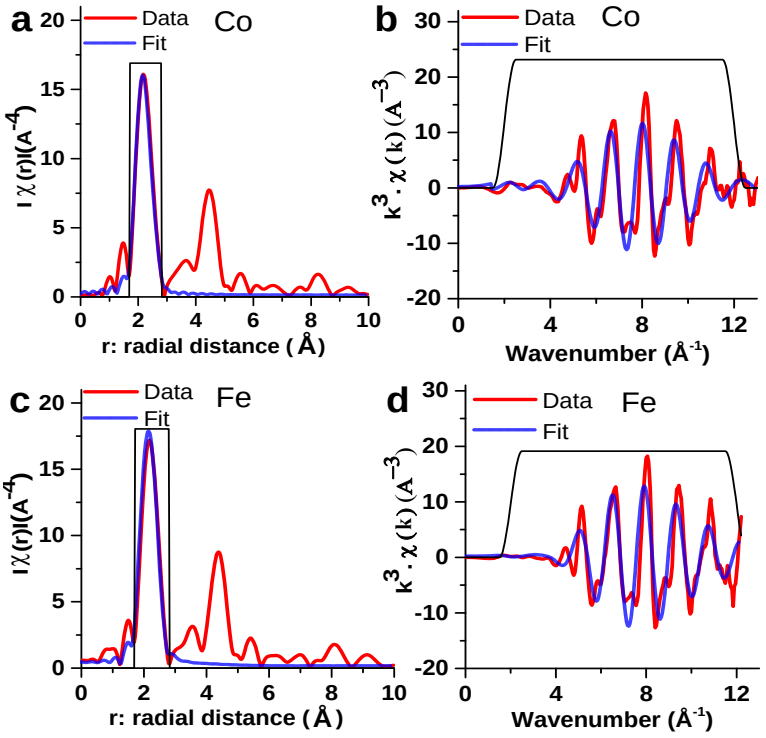

Figure 3.9. X-ray absorption studies of GT-1. **(a, c)** Fourier transform of the EXAFS spectra in r-space and the corresponding first-shell least-squares fit (black solid line) for the Co and Fe. **(b, d)** EXAFS χ(k) signals in k-space and the corresponding 1st shell least-squares fit (black solid line) for the Co and Fe. Fitted spectra using Fe_3Co_7 model confirmed the formation of Fe_3Co_7 alloy in GT-**1**. Copyright 2018, Springer Nature.

Table 3.3. Curve-fitting analysis for the Pt L_3-edge EXAFS of Pt-GT-1: Pt L_3-edge EXAFS curve fitting parameters (R: Bond distance, CN: Coordination numbers, σ^2: Debye–Waller factor). Copyright 2018, Springer Nature.

Sample	Path	R(Å)	CN (atoms)	σ^2 (Å^2)
Pt-GT-1	Pt-Pt	2.77	10.54	0.0054
	Pt-Pt	3.86	4.32	0.0029
Pt-Foil	Pt-Pt	2.76	12.0	0.0050
	Pt-O	3.91	6.0	0.0070
Pt-C	Pt-O	1.99	1.58	0.0057
	Pt-Pt	2.75	5.11	0.0064

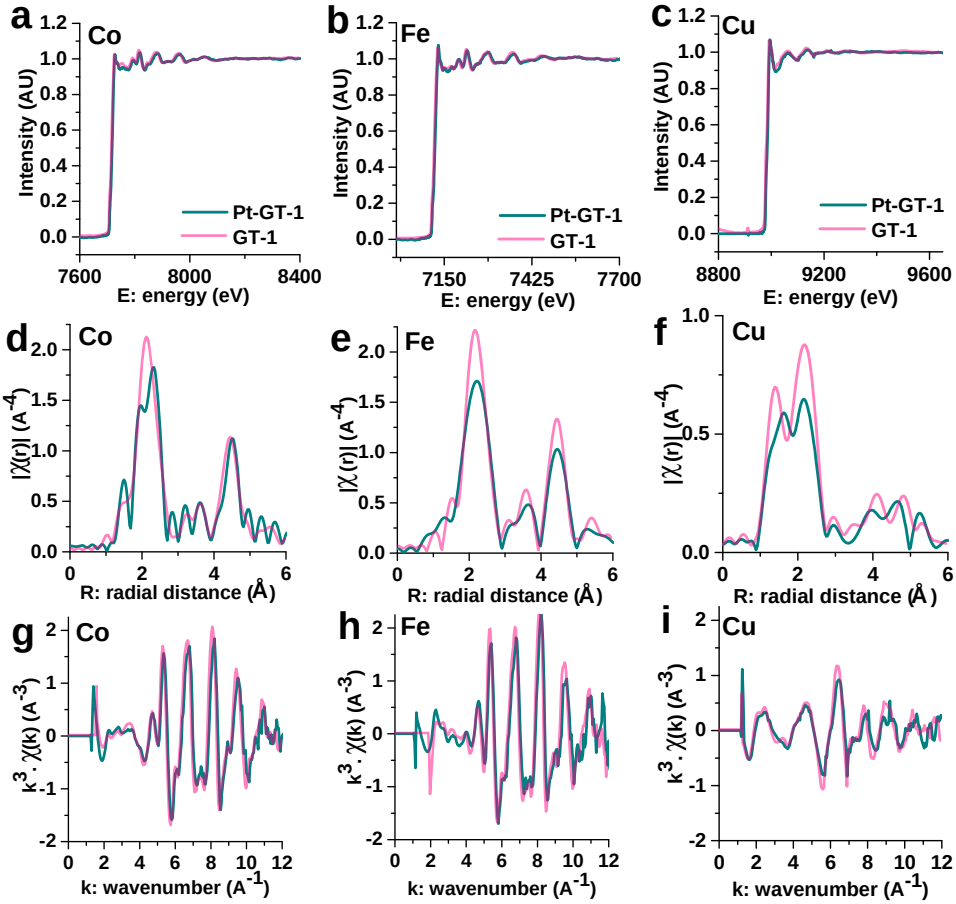

Figure 3.10. X-ray absorption studies of Pt-GT-1 and GT-1: **(a-c)** X-ray absorption near-edge structure (XANES) spectra at Co K-, Fe K-, and Cu K-edges. **(d-f)** Fourier transform of the EXAFS spectra in real space at Co K-, Fe K-, and Cu K-edges. **(g-i)** EXAFS χ(k) signals Co K-, Fe K-, and Cu K-edges. Copyright 2018, Springer Nature.

Table 3.4. Curve-fitting analysis for Fe and Co K-edge EXAFS of Pt-GT-1: Fe and Co K-edge EXAFS curve fitting parameters (R: Bond distance, CN: Coordination numbers, σ^2: Debye–Waller factor). Copyright 2018, Springer Nature.

Sample	Path	R(Å)	CN (atoms)	σ^2 (Å^2)
Pt-GT-1	Co-Co	2.45	4.12	0.0028
	Co-Co	2.78	5.17	0.0032
	Co-Fe	2.52	2.22	0.0032
	Fe-Co	2.45	5.60	0.0049
	Fe-Co	2.81	1.00	0.0030
	Fe-Fe	2.88	4.60	0.0037

3.4.4. X-ray photoelectron spectroscopy analysis

The XPS chemical composition analysis of the GT-1, GT-2, and GT-3 samples further indicates the presence of metal alloys inside GTs (Table 3.1). It is suggested that the different atomic concentrations of components are present in all samples. The GT-2 hybrid indicates the presence of a large amount of Fe atoms. Similarly, larger amounts of Co and Cu atoms exist in GT-1 and GT-3 hybrid catalysts.

XPS core-level spectra of GT-1/2/3: The core-level XPS spectra of C 1s is deconvoluted into three pairs of individual peaks at 284.8, 285.7, and 286.6 eV[28-29] (Figure 3.11a). The sharp peak at 284.8 eV is attributed to graphitic carbon adsorbed on the surface. Peaks at 285.7 and 286.6 eV are attributed to the presence of C–O bonds[28], and C≡N bonds (originated from gC_3N_4)[28]. The core-level Fe 2p spectra is deconvoluted into six peaks at 707.9, 711.4, 714.4, 721.1, 724.8, and 732.8 eV. The two major peaks at 714.4 and 732.8 eV are attributed to Fe with high valence state, called as Fe-N_x species[30] (Figure 3.1b). Meanwhile, two characteristic peaks located at 711.4 and 724.8 eV are ascribed to shake-up satellites[30] (Figure 3.1b). Additionally, the two peaks centered at 707.9 and 721.1 eV are attributed to metallic iron.[30-31] Similarly, Co 2p XPS spectrum shows that the Co 2p spectrum splits into six peaks at 779.3, 781.5, 785.2, 793.0, 795.7, and 802.5 eV. The two peaks at around 779.3 and 793.0 eV are in accordance with Co metal peaks[30, 32] (Figure 3.11c). The other two peaks at 785.2, and 802.5 eV are attributed to shake-up satellites[30, 32] (Figure 3.11c). The two peaks located at 781.5 and 795.7 eV correspond to ionic state[30, 32] arising from Co-N_x species (Figure 3.11c). It is clear that metallic Fe/Co and Fe-N_x/Co-N_x signals appeared in the Fe 2p and Co 2p spectra, respectively. However, the XRD spectrum showed no peak from metal oxides. Overall, the observed signals for Fe-N_x/Co-N_x arise from the unique host–guest electronic interaction between the inner metal/alloy cores and outer graphitic carbon shells. On the other hand, the Cu 2p core-level XPS peak is composed of four peaks at around 932.8, 934.9, 952.7 and 954.4 eV (Figure 3.11d). The two major peaks at 932.8 and 934.9 eV are attributed to metallic copper (Cu^0)[33-34] and oxidized Cu $2p_{3/2}$ (Cu^{2+}), respectively. There are two other peaks of Cu $2p_{1/2}$ and Cu $2p_{3/2}$ centered at 952.7 and 954.4 eV, respectively. Usually, monometallic Cu

is oxidized to Cu^{2+}; however, the absence of shake-up satellite peak for Cu^{2+} suggests that metallic Cu is spread over the Fe_3Co_7 alloy surface. The core-level XPS spectra of N 1s peaks are divided into two components: pyridinic-N (398.9 eV) and graphitic-N (401.2 eV) (Figure 3.11e). The peaks in core-level XPS spectra of C, N, Fe, Co and Cu in GT-2 and GT-3 are almost similar to that of GT-1 (figures 3.12 and 3.13)

XPS core-level spectra of Pt-GT-1: The core-level XPS spectra of C 1s are deconvoluted into two/three pairs of individual peaks at 284.6, 285.5, 286.8, 291.5 and 292.2 eV, respectively[28-29] (Figure 3.14a). The sharp peak at 284.6 eV is attributed to graphitic carbon adsorbed on the surface. Peaks at 285.5 and 286.6 eV are attributed to the presence of C– O bonds, C≡N bonds (originated from g-C_3N_4).[28] The characteristic peaks of C–F at 291.5 eV, and C–F_2 at 292.2 eV correspond to the chemical structure of Nafion. The core-level XPS spectrum of Pt 4f fits into two peaks: Pt $4f_{7/2}$ (~71.4 eV) and $4f_{5/2}$ (~74.6 eV), reflecting the metallic Pt characteristics (Figure 3.14b). The peaks in core-level XPS spectra of Fe, Co, Cu and N in Pt-GT-1 are almost similar to that of GT-1 (figures 3.14c-e)

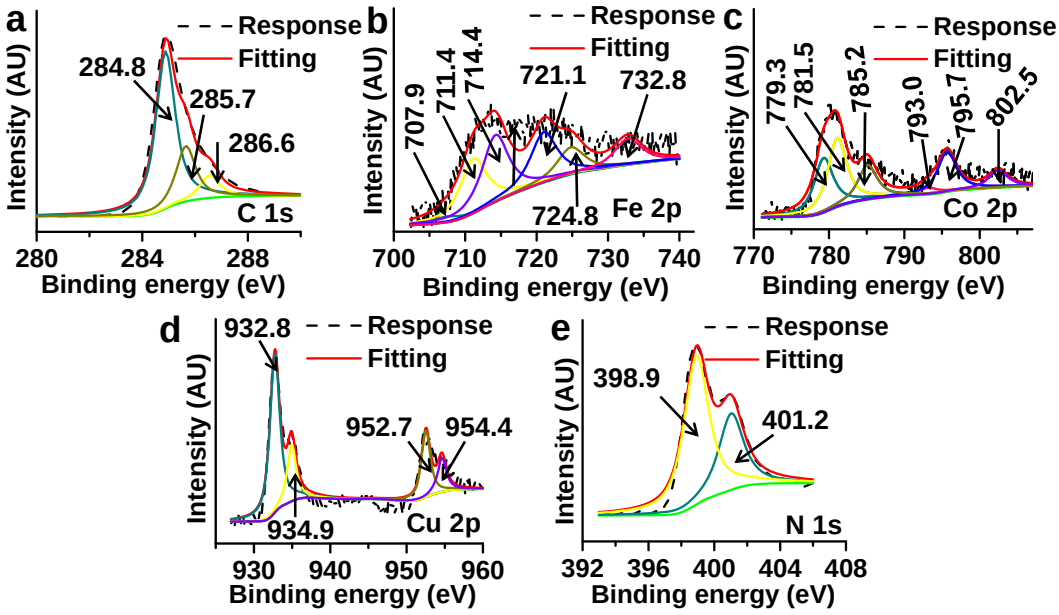

Figure 3.11. X-ray photoelectron spectroscopy analysis (XPS) of GT-1. The core-level XPS spectra for constituent elements: (**a)** C 1s, **(b)** Fe 2p, **(c)** Co 2p, **(d)** Cu 2p, **(e)** N 1s (AU = arbitrary units). Copyright 2018, Springer Nature.

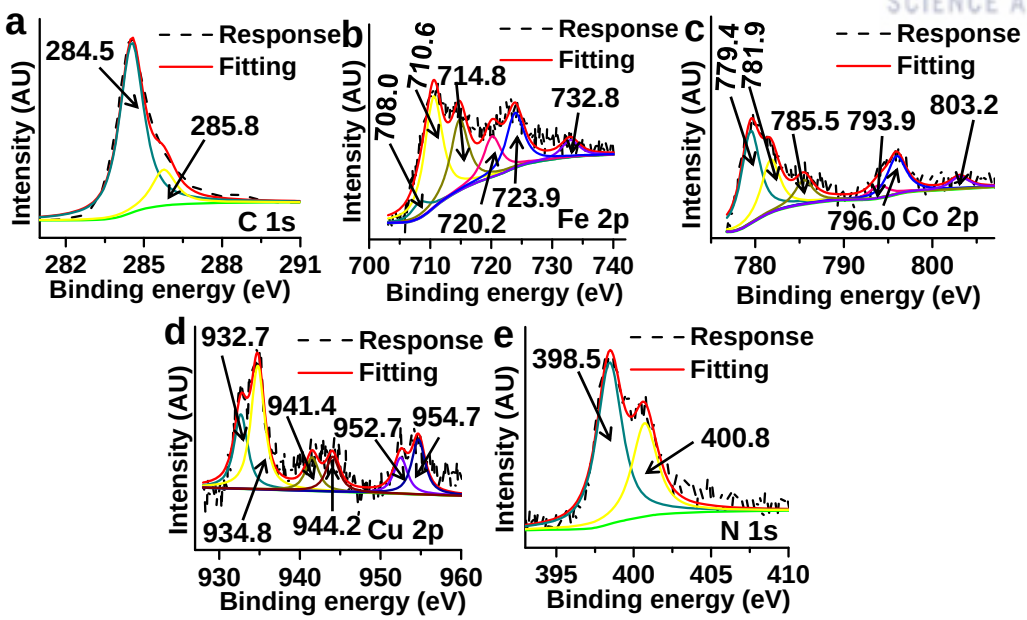

Figure 3.12. The core-level XPS spectra for constituent elements in GT-2. **(a)** C 1s, **(b)** Fe 2p, **(c)** Co 2p, **(d)** Cu 2p, **(e)** N 1s (AU = arbitrary units). Copyright 2018, Springer Nature.

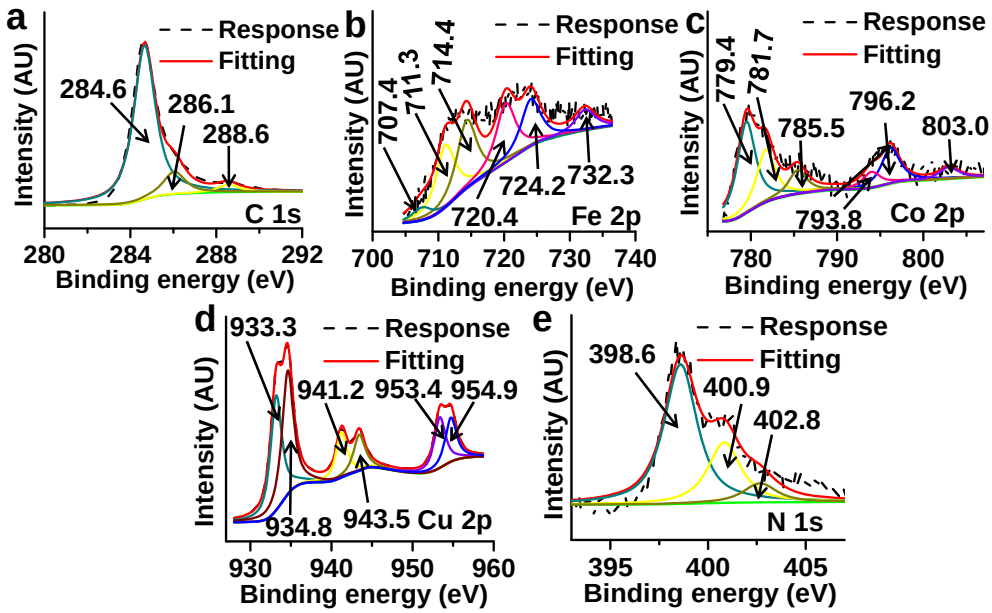

Figure 3.13. XPS of GT-3 The core-level XPS spectra for constituent elements in GT-3. **(a)** C 1s, **(b)** Fe 2p, **(c)** Co 2p, **(d)** Cu 2p, and **(e)** N 1s (a.u. = arbitrary units). Copyright 2018, Springer Nature.

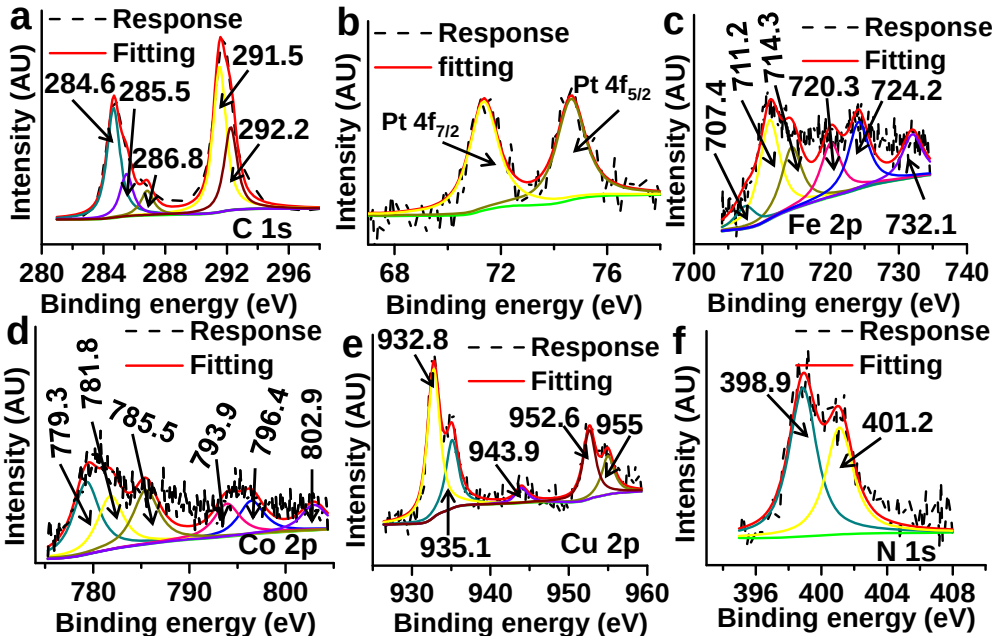

Figure 3.14. XPS spectra of Pt-GT-1**.** The core-level XPS spectra for constituent elements: **(a)** C 1s, **(b)** Pt 4f, **(c)** Fe 2p, **(d)** Co 2p, **(e)** Cu 2p, **(f)** N 1. Copyright 2018, Springer Nature.

3.4.5. XRD analysis for GT-1/2/3

The characterization of XRD shows the structural pattern of GT-1/2/3 samples (Figure 3.15a). Generally, the wide, weak and sharp diffraction peaks at $2\theta = 26.3^{o}$ are attributed to the (002) plane of crystalline graphite peak and correspond to an interlayer spacing of about 0.34 nm.[35-36] Sharp peak intensity for GT-1, GT-2 and GT-3 indicates a higher graphitization degree. Crystalline metallic phases of Fe, Co, and Cu can be found in all the samples (Figure 3.15a). The XRD pattern of GT-3 hybrid shows strong Cu peaks, indicating the formation of a non-alloyed state, which is confirmed by TEM-EDX mapping. The XRD results also showed the copper oxide signal, indicating that a significant amount of copper is deposited on the surface of GT-3. On the other hand, Fe and Co in all samples show the FeCo alloys peaks, suggesting the formation of metallic character of the pure FeCo alloys (without any metal oxide signal), which provides strong evidence that these NPs are encapsulated inside the GTs. Furthermore, Fe and Co in GT-1 indicates the presence of Fe_3Co_7 alloys, consistent with HRTERM lattice spacing and fitted Fourier transform EXAFS spectra (Figure 3.9). Similarly, GT-2 exhibits the formation of Fe_7Co_3 alloys. [Note: We also carried out the XRD analysis of Pt-GT-1 to Pt-GT-5, but a tiny amount of Pt gave no significant change in XRD patterns. Thus, these XRD spectra are not reported here].

3.4.6. Raman spectroscopy analysis

Raman spectroscopy is a direct and non-destructive technique for investigating defects and ordered/disordered structures of carbon, which we used for the study of the graphitized structure of GT. The GT-1, GT-2, and GT-3 samples exhibit a strong D-band (~1350 cm^{-1}) and G-band (~1585 cm^{-1}) corresponding to the disorder-induced phonon mode and the graphitized structure, respectively (Figure 3.15b). The wide and weak 2D band peak at 2685 cm^{-1} is used to confirm the presence of graphene-like sheets and it originates from a double resonance process that links phonons to the electronic band structure (Figure 3.15b).

3.4.7. FT-IR analysis

FT-IR was used to characterize the functional groups in the GT-1, GT-2, and GT-3 samples (Figure 3.15c). For the spectrum of all samples, the band covering the range of 3700-3300 and 2930 cm^{-1} corresponds to the O-H and C-H stretching, respectively. The FTIR spectra of all samples with main peaks at 1200 cm^{-1} is attributed to the C-OH bonds, while the absorption band at 1560 cm^{-1} is assigned to C=C bonds associated with the skeletal vibration of the graphitic sheets. FTIR absorption bands demonstrate the presence of graphitized structure in all samples, which is consistent with XRD spectra.

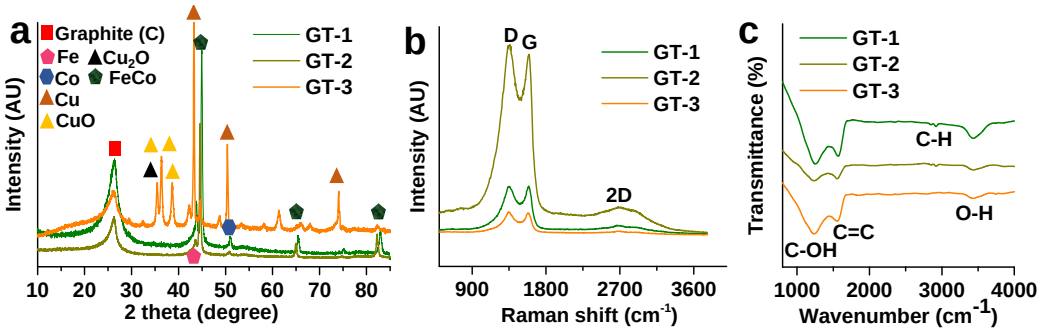

Figure 3.15. XRD, Raman, and FTIR analysis of GT-1, GT-2 and GT-3 at room temperature. **(a)** XRD. (**b)** Raman spectra. **(c)** FTIR spectra. Copyright 2018, Springer Nature.

3.4.8. BET surface area analysis

The Brunnauer-Emmett-Teller (BET) surface areas for GT-1, GT-2, and GT-3 samples are 219.8, 286.2, and 193.6 $m^2\ g^{-1}$, respectively (Figure 3.16). The change in surface area of GT-2 samples is due to the large size and diameter of GTs. However, in the case of GT-3 sample, most of surface area is covered by Cu particles coated on graphitic sheets and tubes, which reduce the surface area of hybrid. The general pattern of the N_2 sorption isotherms for GT-1, GT-2, and GT-3 samples indicates the existence of different pore sizes varying from micropores to mesopores (Figure 3.16). At low relative pressure area ($P/P_0 < 0.1$), these sample curves showed a drastic uptake, suggesting the presence of micropores. On the other hand, all samples exhibited the existence of mesopores, which is very useful for facile movement of electrolytes during HER measurements. The Barrett–Joyner–Halenda (BJH)

average pore size diameters of GT-1, GT-2, and GT-3 samples (Figure 3.16) derived from N2 adsorption show peaks around ~3.9, ~3.79, and ~4 nm, respectively, which are critical for HER activity.

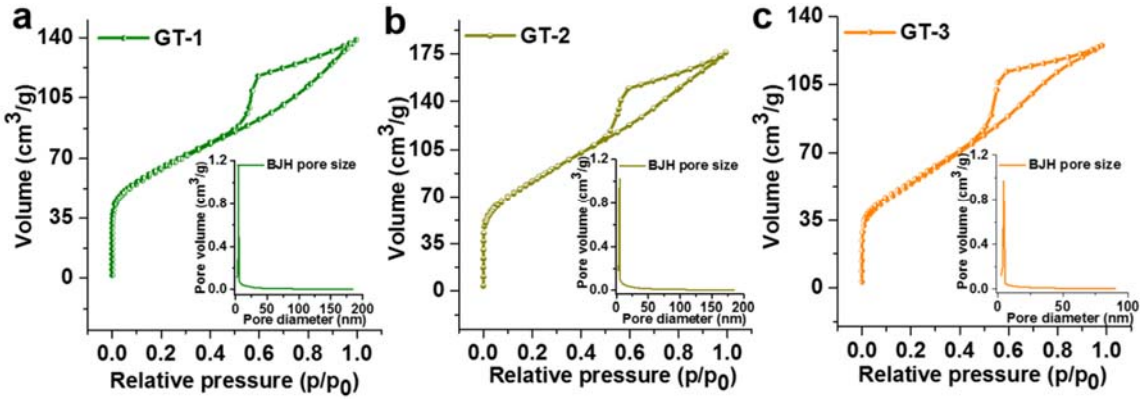

Figure 3.16. BET surface area. **(a-c)** Nitrogen adsorption–desorption isotherms of the as-prepared three samples. The inset in each figure represents the pore size distribution of each catalyst. Copyright 2018, Springer Nature.

3.4.9. Electrochemical analysis

A three-electrode system was used to evaluate the electrocatalytic HER activities of the hybrid catalysts in an acid electrolyte (Figure 3.17a-d). Among the designed catalysts, GT-1 shows the lowest overpotential and highest current density in the whole potential region (Figure 3.17a). Although we can consider three types of GTs (pristine GT (GTo), N-doped GT (GTN) and pyridinic-N-doped GT (GTp)), GTp is expected to be the dominant species because GTs are formed from melamine. Indeed, the XPS shows that the strong peak corresponds to GTp, a moderate peak to GTN and a very weak peak to GTo (Figure 3.11-3.13). Furthermore, GTp is found to give a much more favourable chemical activity than the other two. It is because the bamboo-shaped N-doped GT (6 Ω) is highly conductive with a very small resistance (much smaller than pristine single-wall carbon-nanotube (10 Ω) and the nodes (diaphragms) between two internodes are very thin with a few-layer thickness of the GTp. Hereafter, GTp is simply denoted as GT.

The loading of Pt on the surface of GT-1 is analyzed by ICP–MS, which shows that in Pt–GT-1 the loading of Pt is ~0.5 wt% (average of triplicate readings of three samples; Pt amount =1.40 ± 0.07 $\mu g cm^{-2}$) (Figure 3.17e). This tiny amount of Pt is deposited on the GT surface by the CV electrodeposition of Pt^{4+} cations from $H_2PtCl_6 \cdot 6H_2O$–$HClO_4$. As the Pt loading increases, the current density increases slowly towards the saturation value, but TOF decreases rapidly (Table 3.5). Then, the Tafel slope is minimized to 24 mV dec^{-1} at 15 CV cycles of Pt deposition on the catalytic surface (Figure 3.18). As Pt–GT-1 is the case that has the optimized Pt loading, adding more Pt by electrodeposition gives a significantly reduced catalytic activity in terms of TOF with an increased Tafel slope.

The catalytic activity for the HER was determined in an acidic electrolyte. Pt–GT-1 displays zero onset potential within the experimental limit (Figure 3.17b), a Tafel slope of 24 mV dec^{-1} **(**Figure 3.17 c), an exchange current density of 1.14 mA cm^{-2}, a high TOF (7.22 s^{-1}) and a very low overpotential (18 mV in 0.5 M H_2SO_4 and 66 mV in 0.1M $HClO_4$ for a scan rate of 2 mV s^{-1}) at 10 mA cm^{-2} (Figure 3.17 b, Figure 3.19 a, c). To the best of our knowledge, Pt–GT-1 shows higher activity than previously reported carbon-based metal and metal oxide electrocatalysts under similar conditions with the very small Tafel slope attributed to the rapid desorption of two hydrogen atoms to form H_2 gas.[37] According to the Butler–Volmer equation, H^+ discharges as an adsorbed hydrogen intermediate (H_{ads}) by coupling with an electron on the catalytic surface (the Volmer reaction, $* + H^+_{aq} + e^- \rightarrow H^*_{ads}$), where * denotes a catalytic active site, and then the reaction proceeds by a Tafel reaction ($2H^*_{ads} \rightarrow H_2 + 2^*$).[37-39]

The HER polarization curves of Pt–GT-1 display a minimal negative shift (0.028 V) after a 10,000 cycling test, which shows long term durability (Figure 3.17d). This electrocatalyst shows excellent stability in acid media with very slow attenuation for six hours at − 0.402 V versus SCE (Figure 3.17 g). Microscopy indicates that the surface texture and morphology of Pt–GT-1 remain intact after the stability test (Figure 3.20). The ICP–MS composition analysis does not exhibit substantial changes of Pt, Fe, Co and Cu (Figure 3.17e), which indicates that the FeCo/Cu components inside the GTs are well preserved. In contrast, all the FeCo/Cu components outside the GTs of Pt–GT-1 were already washed out in the synthesis process of electrodeposition of Pt into GT-1 in acid electrolyte, as evidenced from the HRTEM image of Pt–GT-1 (Figure 3.2g-i).

To demonstrate the scalability of the electrochemical device for industrial applications, we fabricated a two-electrode device by coating Pt–GT-1 and 20 wt% Ir/C on graphite and using them as the cathode and anode, respectively. The electrochemical device shows water splitting to produce hydrogen (cathode) and oxygen (anode) gases; a current density of 10 mA cm^{-2} was obtained at 1.69 V, which is 60 mV lower than that of commercial catalysts (1.75 V for 20 wt% Pt/Ir). The minimal voltage required to split water is only 1.5 V in acidic water for this set-up with a 1.4 μ g loading of Pt at the cathode (Figure 3.17f).

To examine the electrochemical oxygen evolution reaction (OER) catalytic activity, Ir/C benchmark ink was drop-casted onto GCE electrode. The as-prepared working electrode was tested in 0.1 M $HClO_4$ solution. Ir/C shows an OER process with an onset potential of 1.47 V and the benchmark current density (10 mA cm^{-2}) potential of Ir/C is ~1.62 V, which is responsible for increase in potential for overall water splitting (Figure 3.19b).

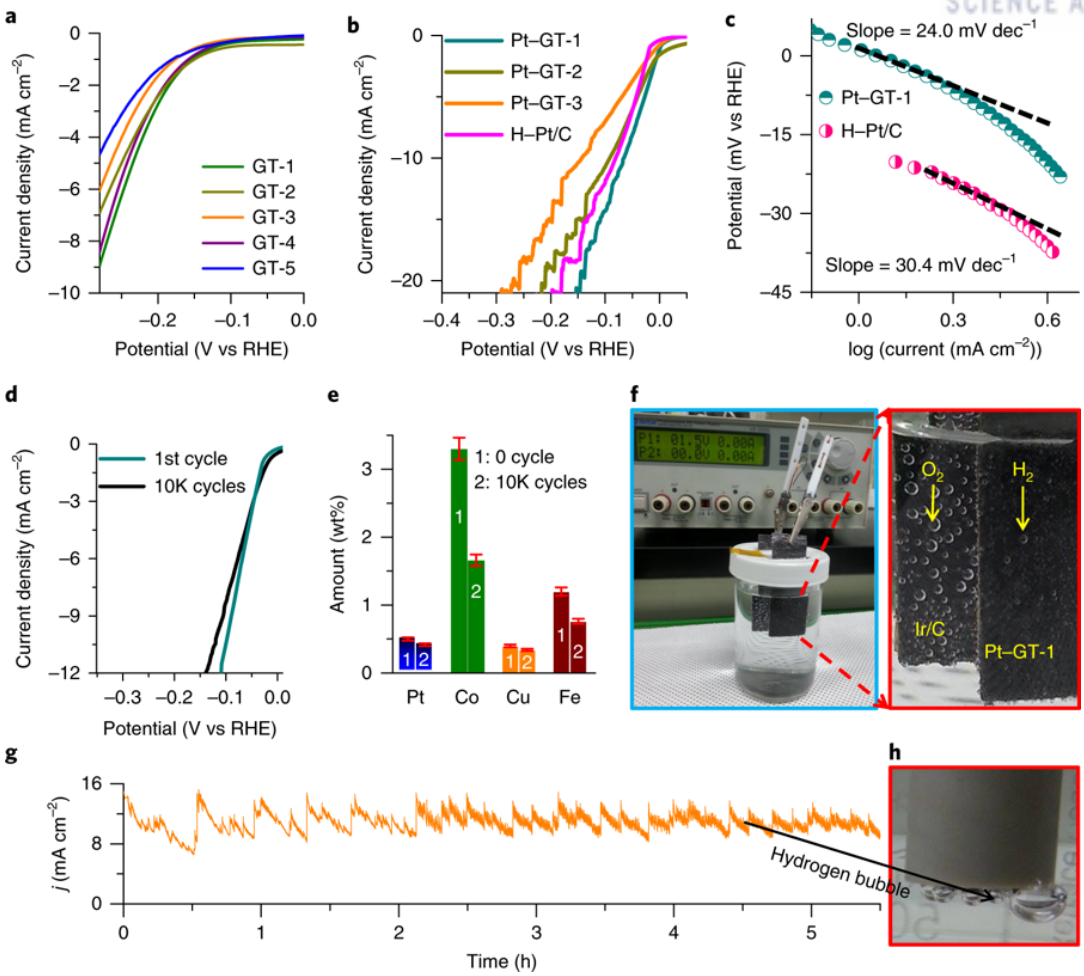

Figure 3.17. Electrochemical performance and demonstration of water-splitting device. **(a, b)** Polarization curves in the absence **(a)** and presence **(b)** of Pt loadings on electrocatalysts and in commercial high Pt (H–Pt)/C in 0.1M HClO4 at a scan rate of 2 mV s^{-1}. **(c)** Tafel plots. **(d)** Polarization curves before and after 10,000 CV scans. **(e)** ICP–AES analysis of the Pt–GT-1 electrocatalysts before (1) and after (2) 10,000 cycle stability tests (error bars denote s.d. based on three independent experiments). **(f)** The optical photograph of acidic water splitting at 1.5 V shows the oxygen and hydrogen bubble generation. Inset: close up of the electrodes. **(g, h)** Chronoamperometric response of the Pt–GT-1 electrocatalyst at an applied potential of − 0.402 V vs SCE. The fluctuation of current density (*j*) is observed due to continuous growth and the release of hydrogen bubbles at catalysts surfaces, as shown in the photograph in **h**. Copyright 2018, Springer Nature.

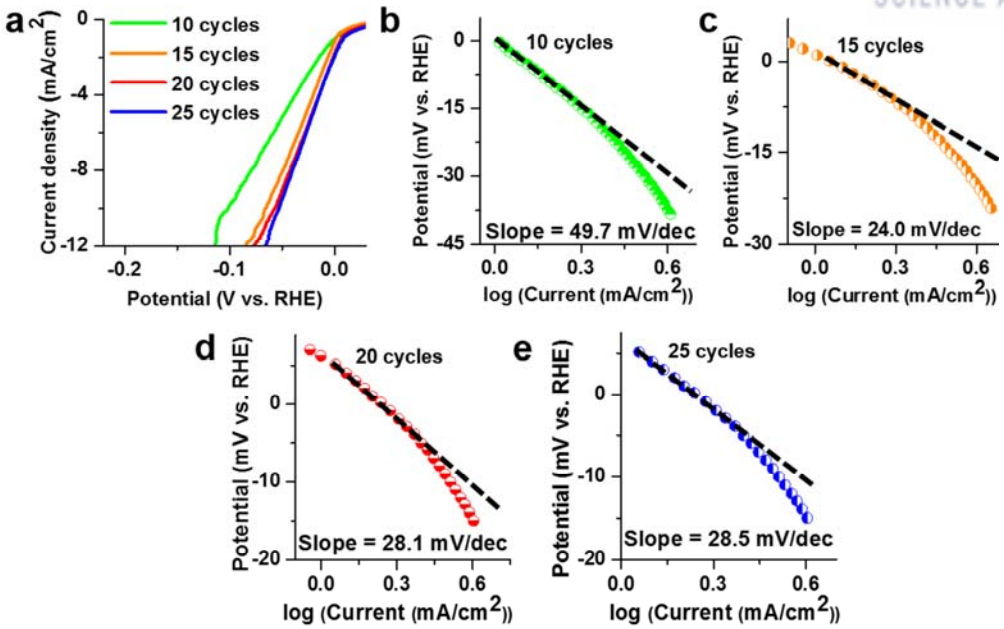

Figure 3.18. Different cyclic voltammetry (CV) cycles for Pt deposition on the catalyst surface for hydrogen evolution reaction (HER) test. **(a)** Scan rate 100 mV/s. The linear sweep voltammetry results show that the HER activity is only slightly changed after 15 cycles. (**b-e)** Tafel slopes for the materials after 10, 15, 20, and 25 CV cycles of Pt deposition on GT-**1**. Copyright 2018, Springer Nature.

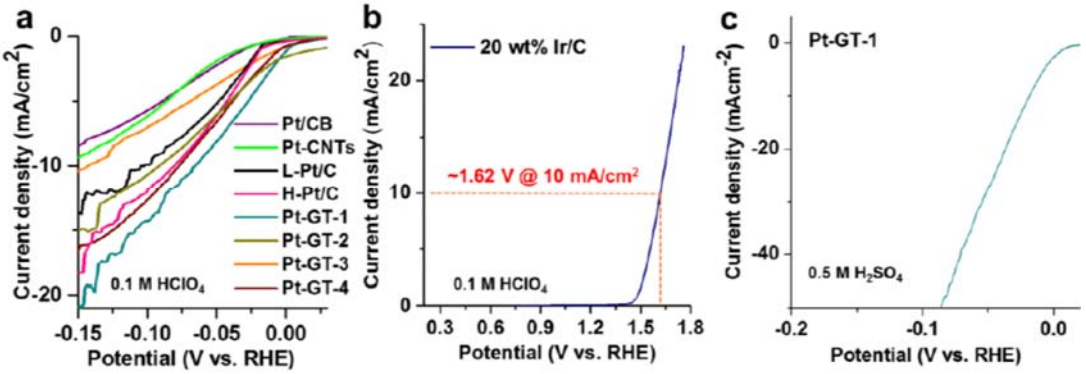

Figure 3.19. Hydrogen evolution reaction (HER) and oxygen evolution reaction (OER) activities. **(a)** Comparison of HER activities; H-Pt/C and L-Pt/C represent high and low amount of Pt loadings on working electrode (CB = carbon black; CNTs = carbon nanotubes). (**b)** OER activity of Ir/C in half cell test, which is used for electrochemical device fabrication. Copyright 2018, Springer Nature.

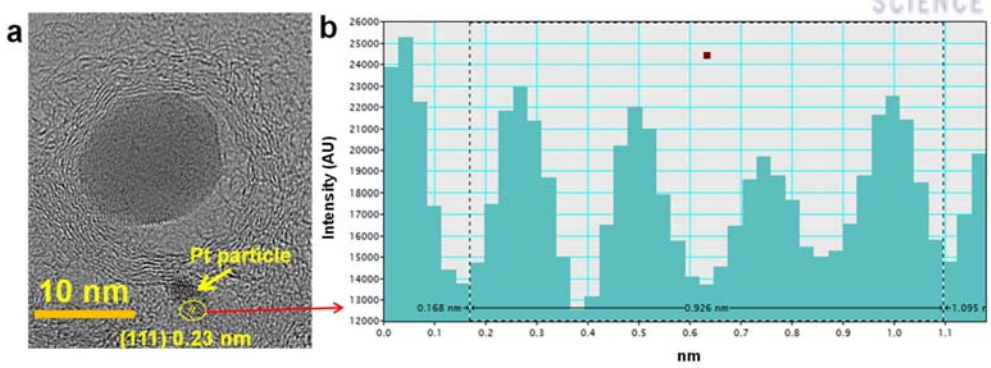

Figure 3.20. HRTEM image and lattice spacing analysis after durability tests (10000 CV cycles) of the Pt-GT-1 catalyst. **(a)** HRTEM image and **(b)** intensity profile used to measure the interplanar distances corresponding to (111) which show the presence of Pt particles. Copyright 2018, Springer Nature.

Table 3.5. Compositional change (Pt versus GT-1 alloys): The **e**ffect of current density and turnover frequency (TOF) at 66 mV overpotential. Copyright 2018, Springer Nature.

Catalyst	Pt amount (wt.%)	j (mA/cm^2)	TOF (s^{-1})
10	~ 0.28	6.73	8.70
15	~ 0.50	10.0	7.22
20	~ 2.20	10.95	1.78
25	~ 3.60	12.35	1.24

3.4.10. Atomistic characterization

Pt–GT-1 gives a 96 times better activity (for TOF) than Pt/C, which implies the existence of active sites better than or compatible with a Pt (111) surface. Noting that many defect sites are present on the GT surface, we theoretically investigated pyridinic N_nC_{4-n}/GT defect sites in which a Pt cation can be readily embedded in the center of the planar tetragonal structure with large binding energy. The HER activity was evaluated using density functional theory (DFT), based on a standard approach. We studied the Gibbs free energies (ΔG_{H^*}) for hydrogen adsorption/desorption for various active sites of Pt–GT-1, including the possible formation of Pt clusters/NPs in the defect sites of a GT. In particular, the formation of defect sites in a GT and single Pt atoms embedded in the defect sites of the GT and these populations were investigated based on their formation energies and Pt-clustering energies. The formation energies calculation predicted that during the synthesis of GT, the defect sites with N_3C_1, N_2C_2, N_4, in conjunction with N_2C_1 and N_3 structures are formed easily in harsh acidic solution due to its small formation energy ($\Delta E < 2$ eV), and single Pt atoms and some small Pt clusters can be readily captured in such defect sites, which was clearly elucidated from aberration-corrected TEM analysis. The DFT calculation demonstrated that the atomic Pt–N_2C_2 sites have very low ΔG_{H^*} (0.04 eV) compared to Pt (111) surface, which strongly supported the experimental results that the HER reaction

at Pt–GT-1 should be far better than Pt (111) surface (the detailed theoretical calculations, figure and their description are available from our published Nature energy paper "Nature Energy, 2018, 3, 773–782").

Our theoretical prediction led us to search successfully for single Pt atoms embedded in a GT using aberration-corrected TEM equipped with an ultrafine probe. Indeed, figure 3.21a-c shows the HAADF–STEM image of numerous single Pt atoms embedded at surface defects and few Pt clusters on the surface (Methods), an EDX image of a ~2 nm-sized Pt cluster with single Pt atoms around it and the EELS spectra of C and N on surface plane.

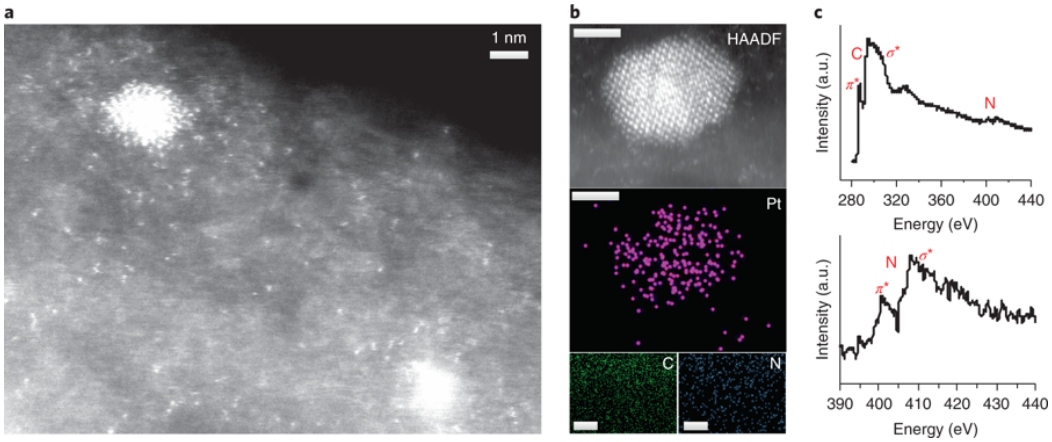

Figure 3.21. Images of single Pt atoms and Pt clusters/NPs on a GT surface. **(a)** The HAADF–STEM image (taken through the GT surface) displays the information of the *Z* contrast (which is roughly proportional to Z^2, where *Z* is the atomic number), which shows many single (0.1–0.2 nm in size) Pt atoms embedded at the GT surface and few (1–2 nm in size) Pt clusters on the GT surface. **(b)** The EDX maps show small Pt particles, which proves that the 0.1–0.2 nm-sized particles with a bright colour are single Pt atoms in the STEM image. Scale bars, 1 nm. **(c)** The EELS spectra for a region that comprises several single Pt atoms indicate that an N edge arises among graphitic matrix and the split π^*–σ^* N edge reflects planar Pt–N–C bonds on the GT surface. Co, Fe and Cu particles on the GT surface are not seen in EELS, which excludes galvanic displacements of FeCo/Cu for the possible Pt 3*d* skin–alloy effects, as evidenced also from EXAFS (Figures 3.8 and 3.9). Copyright 2018, Springer Nature.

3.5. Conclusion

In summary, we have demonstrated that an atomic-scale engineered electrocatalyst, with melamine-derived GTs that encapsulate an alloy (Fe_3Co_7) and have Cu layers deposited on the inner tube walls and a hyperlow loaded Pt on the GT surface exhibit a high HER activity with a large exchange current density and high TOF with a low overpotential. This striking activity is ascribed to the intriguing geometric/electronic structure of the catalyst, which brings together a near-zero value of ΔG_{H^*} and a rapid charge-transfer process to promote the hydrogen/proton adsorption and to lower the kinetic energy barrier via a minimal Pt incorporation. We suggest that this is caused by the synergistic conductivity-enhancement effect between the single Pt atoms embedded in the pyridinic N_2C_2 defect sites of the GT

and the Pt nanoclusters, as well as the high conductivity of N-doped GTs that encapsulate FeCo/Cu. The long-term durability (stable over 10,000 CV cycles) of Pt-GT-1 in acid media is attributed to the high stability of the GTs that encapsulate FeCo/Cu and the high stability of single Pt atoms embedded in the planar tetragonal defect sites of the GT.

3.6. Reference

1. Wang, H.; et al., Bifunctional non-noble metal oxide nanoparticle electrocatalysts through lithium-induced conversion for overall water splitting. *Nat. Commun.* **2015,** *6*, 7261.
2. Gong, M.; et al., Nanoscale nickel oxide/nickel heterostructures for active hydrogen evolution electrocatalysis. *Nat. Commun.* **2014,** *5*, 4695.
3. Yin, H.; et al., Ultrathin platinum nanowires grown on single-layered nickel hydroxide with high hydrogen evolution activity. *Nat. Commun.* **2015,** *6*, 6430.
4. Durst, J.; et al., New insights into the electrochemical hydrogen oxidation and evolution reaction mechanism. *Energy Environ. Sci.* **2014,** *7* (7), 2255-2260.
5. Lv, H.; et al., A New Core/Shell NiAu/Au Nanoparticle catalyst with Pt-like activity for hydrogen evolution reaction. *J. Am. Chem. Soc.* **2015,** *137* (18), 5859-5862.
6. Georgakilas, V.et al., Broad family of carbon nanoallotropes: classification, chemistry, and applications of fullerenes, carbon dots, nanotubes, graphene, nanodiamonds, and combined superstructures. *Chem. Rev.* **2015,** *115* (11), 4744-4822.
7. Geng, X.; et al., Pure and stable metallic phase molybdenum disulfide nanosheets for hydrogen evolution reaction. *Nat. Commun.* **2016,** *7*, 10672.
8. Zhou, H.; et al., Outstanding hydrogen evolution reaction catalyzed by porous nickel diselenide electrocatalysts. *Energy Environ. Sci.* **2017,** *10* (6), 1487-1492.
9. Wang, D.-Y.; et al., Highly active and stable hybrid catalyst of cobalt-doped FeS_2 nanosheets-Carbon nanotubes for hydrogen evolution reaction. *J. Am. Chem. Soc.* **2015,** *137* (4), 1587-1592.
10. Liu, W.; et al., A highly active and stable hydrogen evolution catalyst based on pyrite-structured cobalt phosphosulfide. *Nat. Commun.* **2016,** *7*, 10771.
11. Li, Y. H.; et al., Local atomic structure modulations activate metal oxide as electrocatalyst for hydrogen evolution in acidic water. *Nat. Commun.* **2015,** *6*, 8064.
12. Dendooven, J.; et al., Independent tuning of size and coverage of supported Pt nanoparticles using atomic layer deposition. *Nat. Commun.* **2017,** *8* (1), 1074.
13. Stephens, I. E. L.; Chorkendorff, I., Minimizing the use of platinum in hydrogen-evolving electrodes. *Angew. Chem. Int. Ed* **2011,** *50* (7), 1476-1477.
14. Subbaraman, R.; et al., Enhancing hydrogen evolution activity in water splitting by tailoring Li^+-$Ni(OH)_2$-Pt Interfaces. *Science* **2011,** *334* (6060), 1256.
15. Kibsgaard, J.; Jaramillo, T. F.; Besenbacher, F., Building an appropriate active-site motif into a hydrogen-evolution catalyst with thiomolybdate [Mo3S13]2− clusters. *Nature Chemistry* **2014,** *6*, 248.
16. Chen, Z.; et al., Core–shell MoO_3–MoS_2 nanowires for hydrogen evolution: A functional design for electrocatalytic materials. *Nano Lett.* **2011,** *11* (10), 4168-4175.
17. Ravel, B.; Newville, M., ATHENA, ARTEMIS, HEPHAESTUS: data analysis for X-ray absorption spectroscopy using IFEFFIT. *Journal of Synchrotron Radiation* **2005,** *12* (4), 537-541.
18. Kresse, G.; Furthmüller, J., Efficient iterative schemes for ab initio total-energy calculations using a plane-wave basis set. *Physical Review B* **1996,** *54* (16), 11169-11186.
19. Blöchl, P. E., Projector augmented-wave method. *Physical Review B* **1994,** *50* (24), 17953-17979.

20. Kresse, G.; Joubert, D., From ultrasoft pseudopotentials to the projector augmented-wave method. *Physical Review B* **1999,** *59* (3), 1758-1775.
21. Perdew, J. P.; Burke, K.; Ernzerhof, M., Generalized Gradient Approximation Made Simple. *Physical Review Letters* **1996,** *77* (18), 3865-3868.
22. Duchesne, P. N.; Chen, G.; Zheng, N.; Zhang, P., Local structure, electronic behavior, and electrocatalytic reactivity of CO-reduced platinum–iron oxide nanoparticles. *J. Phys. Chem. C* **2013,** *117* (49), 26324-26333.
23. Boita, J.; et. al., Reversible sulfidation of $Pt_{0.3}Pd_{0.7}$ nanoparticles investigated by in situ time-resolved XAS. *J. Phys. Chem. C* **2014,** *118* (10), 5538-5544.
24. Khabashesku, V. N.; Zimmerman, J. L.; Margrave, J. L., Powder Synthesis and Characterization of Amorphous Carbon Nitride. *Chem. Mater.* **2000,** *12* (11), 3264-3270.
25. Dai, K.; et. al., Sonication assisted preparation of graphene oxide/graphitic-C3N4 nanosheet hybrid with reinforced photocurrent for photocatalyst applications. *Dalton Transactions* **2014,** *43* (17), 6295-6299.
26. Su, C.-Y.; et. al., Atomic modulation of FeCo–nitrogen–carbon bifunctional oxygen electrodes for rechargeable and flexible all-solid-state zinc–air battery. *Adv. Energy Mater.* **2017,** *7* (13), 1602420.
27. Ali-Löytty, H.; et. al., Ambient-pressure XPS study of a Ni–Fe electrocatalyst for the oxygen evolution reaction. *J. Phys. Chem. C* **2016,** *120* (4), 2247-2253.
28. Aijaz, A. et. al., $Co@Co_3O_4$ encapsulated in carbon nanotube-grafted nitrogen-doped carbon polyhedra as an advanced bifunctional oxygen electrode. *Angew. Chem. Int. Ed* **2016,** *55* (12), 4087-4091.
29. Batista, J.; Pintar, A.; Mandrino, D.; Jenko, M.; Martin, V., XPS and TPR examinations of γ-alumina-supported Pd-Cu catalysts. *Applied Catalysis A: General* **2001,** *206* (1), 113-124.
30. Biesinger, M. C.; et. al., Resolving surface chemical states in XPS analysis of first row transition metals, oxides and hydroxides: Cr, Mn, Fe, Co and Ni. *Applied Surface Science* **2011,** *257* (7), 2717-2730.
31. Venugopal, G.; Krishnamoorthy, K.; Mohan, R.; Kim, S.-J., An investigation of the electrical transport properties of graphene-oxide thin films. *Materials Chemistry and Physics* **2012,** *132* (1), 29-33.
32. Zhao, X.; Hayner, C. M.; Kung, M. C.; Kung, H. H., In-Plane Vacancy-Enabled High-Power Si–Graphene Composite Electrode for Lithium-Ion Batteries. *Adv. Energy Mater.* **2011,** *1* (6), 1079-1084.
33. Morales-Guio, C. G.; Stern, L.-A.; Hu, X., Nanostructured hydrotreating catalysts for electrochemical hydrogen evolution. *Chemical Society Reviews* **2014,** *43* (18), 6555-6569.
34. Voiry, D.; et. al., Enhanced catalytic activity in strained chemically exfoliated WS2 nanosheets for hydrogen evolution. *Nat. Mater.* **2013,** *12*, 850.
35. Vij, V.; et. al., Nickel-based electrocatalysts for energy-related applications: oxygen eeduction, oxygen evolution, and hydrogen evolution reactions. *ACS Catal.* **2017,** *7* (10), 7196-7225.
36. Liu, Y.; et al., Coupling Mo_2C with nitrogen-rich nanocarbon leads to efficient hydrogen-evolution electrocatalytic sites. *Angewandte Chemie* **2015,** *127* (37), 10902-10907.
37. Lee, K. H.; Oh, J.; Son, J. G.; Kim, H.; Lee, S.-S., Nitrogen-doped graphene nanosheets from bulk graphite using microwave irradiation. *ACS Appl. Mater. Interfaces* **2014,** *6* (9), 6361-6368.
38. Rankin, D. W. H., CRC handbook of chemistry and physics, 89th edition, edited by David R. Lide. *Crystallography Reviews* **2009,** *15* (3), 223-224.
39. Tan, Y. W.; et al., Measurement of Scattering Rate and Minimum Conductivity in Graphene. *Physical Review Letters* **2007,** *99* (24), 246803.

Chapter 4

Highly efficient oxygen reduction reaction activity of graphitic tube encapsulating nitrided Co_xFe_y alloy

4.1. Abstract

Nonprecious metals are promising catalysts to avoid the sluggish oxygen reduction reaction (ORR) in next-generation regenerative fuel cells or metal-air batteries. Therefore, the development of nonprecious metal catalysts for ORR is highly desirable. Herein, precise tuning of the atomic ratio of Fe and Co encapsulated in melamine-derived nitrogen-rich graphitic tube (NGT) is reported. The $Co_{1.08}Fe_{3.34}$ hybrids with metal-nitrogen bonds (7@NGT: $Co_{1.08}Fe_{3.34}$@NGT) shows remarkable ORR catalytic activities (80 mV higher in onset potential and 50 mV higher in half-wave potential than those of state-of-the-art commercial Pt/C catalysts), high current density, and stability. In acidic solution, 7@NGT also shows compatible performance to commercial Pt/C in terms of ORR activity, current density, stability, and methanol tolerance. The high ORR activity is ascribed to the co-existence of Fe-N, Co-N, and sufficient metallic FeCo alloys which favor faster electron movement and better adsorption of oxygen molecules on the catalyst surface. In the alkaline anion exchange membrane fuel cell setup, this cell delivers the power density of 117 mW cm^{-2}, demonstrating its potential use for energy conversion and storage applications.

4.2. Introduction

Oxygen reduction reaction (ORR) activity and durability of fuel cells have gained continuous attention for possible replacement of platinum by nonprecious metal catalysts (e.g., Fe, Co, Ni, and Mn).[1-4] The proton exchange membrane fuel cells heavily rely on platinum-based catalysts which have precluded their widespread utilization.[5-7] To overcome this obstacle, alkaline anion exchange membrane fuel cells (AAEMFC) were proposed and intensively investigated in the last few years.[8-10] By switching from acidic to alkaline electrolyte, it is possible to use nonprecious metal catalysts for the cathode reaction which requires a large amount of Pt in acid.[11-13] However, the sluggish ORR kinetics at the cathode is considered as a major reason for the decrease in efficiency of the next-generation electrochemical energy-conversion devices. The nonprecious metal-containing N/C catalysts seem to be more suitable due to easy fabrication, high catalytic activity, and high stability in alkaline solution, as well as their competition with the state-of-the-art commercial Pt/C.[14-15] In this regard, several approaches have been made to enhance the ORR efficiency better than the commercial; however, their ORR activity performance in either acid or alkaline electrolytic condition remains a critical issue.[16-18]

More recently, bimetallic-based ORR electrocatalysts have been explored due to their higher activity and durability than single metal-based catalysts.[19-21] However, the exploration of simple and

effective technique for tuning catalysts based on nonprecious metals and the understanding of their fundamental reasons for the ORR catalytic activity remain challenging tasks.

Here, for the first time, we show the remarkably enhanced ORR catalytic activity in basic electrolytes by atomic modulation of Fe and Co inside the nitrogen-rich graphitic tube. Impressively, the optimized catalyst (7@NGT: $Co_{1.08}Fe_{3.34}$@NGT, where subscripts 1.08 and 3.34 denote the atomic percentage) exhibits predominant catalytic activity and durability, featuring, excellent onset potential (1.03 V), superb half-wave potential (0.94 V at 3 mA cm^{-2}), and small Tafel slope (44 mV dec^{-1}) for ORR in basic solutions, which significantly surpass those of precious metal benchmark (20 wt% Pt/C) catalyst. In acidic solution, 7@NGT also shows compatible performance to that of Pt/C and remarkable stability and methanol tolerance. During 10 h durability tests, the commercial Pt/C shows loss of more than 60% of their current density, while 7@NGT retained the constant current density under similar experimental conditions. The high activity and stability of this catalyst originate from nitriding (i.e., the heating process that diffuses nitrogen onto the metal surface which often creates surface hardening and corrosion resistance) and encapsulation in the graphitic shell, which facilitates the exposure of active sites and electronic transfer/mass transport.

4.3. Experimental Section

4.3.1. Chemicals

Melamine (99%), cobalt(II) perchlorate hexahydrate, iron(III) chloride (reagent grade, 97%), potassium hydroxide, and Nafion (5 wt%) were purchased from Sigma-Aldrich. Commercial 20 wt% Pt/C was obtained from Johnson Matthey. All the chemicals were analytical grade and used as received without further purification.

4.3.2. Synthetic procedure

For the synthesis of $Co_{1.08}Fe_{3.34}$@NGT (denoted as 7@NGT), the different weight ratios of iron chloride and cobalt perchlorate hexahydrate were used with 2.2 g of melamine (Table 4.1). In the synthesis procedure, the starting materials were first well ground, then dispersed in 80 mL of deionized water and sonicated for 15 h to attain the homogeneous mixture. The obtained mixture was dried at 80 °C and then ground to fine powder. The fine powder was calcined at 750 °C for 4 h under an argon atmosphere with a heating ramping rate of 5 °C min^{-1}. To remove unreacted or debris materials, the calcined product was leached in 0.1M $HClO_4$, then filtered and thoroughly washed with ethanol and deionized water, and finally dried under vacuum at 70 °C.

4.3.3. Optimization of Fe and Co weight ratio in Co_xFe_y@NGT catalyst

We also synthesized a series of Co_xFe_y@NGT catalyst by changing the weight ratio of Fe and Co in Co_xFe_y alloy. Initially, we studied the effect of Fe and Co weight ratio and their total weight amount in Co_xFe_y alloy (Table 4.1-4.2, Catalyst 1@NGT to 6@NGT), and found that the ORR activity increased with the increase in Fe concentration of Co_xFe_y alloy (Figure 4.11a). The catalyst having Fe (0.7 g) and Co (0.35 g) is better in ORR activity than other synthesized catalysts (Table 4.1-4.2 and Figure 4.11a).

Then, keeping the constant weight ratio of Fe (0.7 g), we again make a series of Co_xFe_y@NGT catalyst by changing the weight ratio of cobalt in Co_xFe_y alloy (Table 4.1-4.2), Catalyst 5@NGT, 7@NGT and 8@NGT). The Co_xFe_y@NGT catalyst having Fe (0.7 g) and Co (0.45 g) is better in ORR activity than other catalysts as well as commercial Pt/C (Figure 4.11b and c). We also synthesized Fe@NGT (Fe 0.7 g), Co @NGT (Co 0.7 g) and Co_xFe_y@G (in this catalyst 150 mg graphene oxide was used instead of melamine, while the Fe and Co amount is same as in 7@NGT), and found that the ORR activity of Fe@NGT is greater than that of Co@NGT, but lesser than that of 7@NGT. While the ORR activity of Co_xFe_y@G is much smaller than that of the catalyst having melamine (Figure 4.15b).

4.3.4. Characterization

The FE-SEM analysis was performed with a Hitachi High- Technologies S-4800 microscope. TEM, HR-TEM, and HAADF–STEM– EDS images were taken on JEM-2100F with an acceleration voltage of 200 kV. XPS data were measured on K-alpha (Thermo Fisher, UK) instrument. X-ray absorption fine spectroscopy measurements were carried out on ionization detectors (Oxford) at the Pohang Accelerator Laboratory (PAL). The BET surface area, pore-volume, and pore size distribution with N_2 adsorption/desorption isotherms were measured at 77 K using the BELSORP-miniII (BEL Japan, Inc.) system. For BET, the catalysts were degassed at 180 °C under vacuum for an overnight before measurements. Raman data were collected on a Confocal Raman alpha 300R system. High-power X-ray diffraction (HP-XRD) data were acquired on a Rigaku X-ray diffractometer/D/MAX2500V/PC equipped with a Cu Kα radiation (35 kV, 200 mA) system. The atomic and weight percent of elements in each catalyst were obtained from the Elemental analyzer (Truspec Micro, Leco) and inductively coupled plasma optical emission spectrometry (ICP-OES-700-ES, Varian).

4.3.5. Electrochemical Measurements

All electrochemical measurements were performed in 0.1M KOH and $HClO_4$ solutions using a three-electrode electrochemical workstation system (CHI 760E, CH Instruments, Inc.). The working electrodes in this study were the rotating disk electrode (RDE) and rotating ring-disk electrode (RRDE, PINE AFE7R9GCPT, Pine Instruments, Inc.) having a diameter of 5.61 (glassy carbon disk area = 0.247 cm^2) and 6.25 mm, respectively. SCE and graphite rods were used as a reference electrode and a counter electrode, respectively. To prepare the working electrode, 10 mg of powders of each catalyst was homogeneously dispersed in 1140 μL of water/ethanol (2:1 v/v) with 60 μL of Nafion solution (5 wt %) via sonication for 1 h. Then, for the ORR measurements in basic solutions, 6.00 μL of homogeneous ink was carefully loaded onto glassy carbon disk of an RRDE to achieve a 0.202 mg cm^{-2} loading amount of the catalyst. For acidic ORR measurements, the loading amount of Pt/C and this designed catalyst were 0.08 and 0.32 mg cm^{-2}, respectively. Before each ORR measurement, the electrolyte was bubbled with O_2 for 30 min and maintained over the electrolyte surface during the ORR testing to sustain the O_2 saturation. All the working electrodes were first activated by cycling the potential in the

range of 0.00–1.2 V versus RHE at a scan rate of 50 mV s^{-1} for at least 20 cycles. Linear sweep voltammetry data were recorded at a rotation speed of 1600 rpm at a scan rate of 10 mV s^{-1} in the disk potential range of 1.1–0.4 V versus RHE. The RRDE measurement was performed at a constant ring potential of 1.3 V versus RHE.

All the obtained potential data versus SCE in this study were converted to potential versus RHE using the equation of 4.1:

$$(\text{vs. RHE}) = \text{E(vs. SCE)} + \text{E}^0_{\text{SCE}} + 0.0591\text{pH} \quad (4.1)$$

The number of electrons transferred and hydrogen peroxide production were evaluated from RRDE measurement using the following the equations of 4.2-4.5.

The number of electron transfer (n) during ORR testing

$$\text{n} = 4 \times \frac{\text{I}_\text{d}}{\text{I}_\text{d}+\text{I}_\text{r}/\text{N}} \quad (4.2)$$

where I_d and I_r are disk and ring current densities, respectively, N is the current collection efficiency of the Pt ring which is 0.37.

The percentage of peroxide (% HO_2^-) during the ORR process were calculated using the equations of 4.3-4.5:

$$\frac{1}{\text{j}} = \frac{1}{\text{j}_\text{l}} + \frac{1}{\text{j}_\text{k}} = \frac{1}{\text{B}\omega^{0.5}} + \frac{1}{\text{j}_\text{k}} \quad (4.3)$$

$$\text{B} = 0.64\text{nFAC}_0\text{D}_0^{2/3}\text{n}^{-1/6} \quad (4.4)$$

$$\text{j}_\text{k} = \text{nFkC}_\text{d} \quad (4.5)$$

where J is the measured current density, J_l and J_k are the limiting and kinetic current densities, B is the slope of K-L plots, ω is the rotation rate of the disk electrode, n is the electrons transferred number in ORR, F is the Faraday constant (96485 C mol^{-1}), A is the geometric area of electrode (A=0.247 cm^2), C_0 is the concentration of O_2 which is 1.2 × 10^{-6} mol cm^{-3} in 0.1M KOH, D_0 is the O_2 diffusion coefficient (1.9 × 10^{-5} cm^2 s^{-1}), V is the kinematic viscosity of the solution (0.01 cm^2 s^{-1}), and k is the electron transfer rate constant.

To identify the ORR mechanism and calculate the kinetic parameters, the RRDE test was performed at different rotation rates (ω) at a constant ring potential of 1.3 V versus RHE and used the following equations 4.6-4.7.

$$\frac{\text{I}_\text{d}\text{N}}{\text{I}_\text{r}} = 1 + 2\frac{\text{k}_1}{\text{k}_2} + \left(\frac{1}{\text{Z}_{\text{H}_2\text{O}}}\right)\left[\text{k}_3 + (\text{k}_3 + \text{k}_4)\left(1 + 2\frac{\text{k}_1}{\text{k}_2}\right)\right]\omega^{-0.5} \quad (4.6)$$

$$\text{Z}_{\text{H}_2\text{O}_2} = 0.62\text{D}_{\text{H}_2\text{O}_2}^{\frac{2}{3}}\text{V}^{\frac{1}{6}} \quad (4.7)$$

where D is the diffusion coefficient in 0.1M KOH solution, V is the kinetic viscosity, and k_3 and k_4 are the rate constants in the forward and backward directions, respectively. The linear relationship between I_dN/I_r and $\omega^{-0.5}$ was observed with an intercept value of "A." The ratio of k_1/k_2 was obtained using the relation of equation 4.8.

$$A = 1 + 2\frac{k_1}{k_2} \qquad (4.8)$$

4.3.6. Estimation of Electrochemical double-layer capacitance, active surface area and roughness factor

The electrochemical active sites (ECS) of each catalyst were investigated from the double-layer capacitance (C_{dl}).[22] First, for C_{dl} the potential was cycled in the non-Faradic region (1.06 to 1.14 V vs RHE, because no electrochemical features of faradic current were observed in this region) at different applied scan rate of 5, 10, 20, 50, 100, 200 and 300 mV s^{-1} (Figure 4.13a-j). The current (mA) of each catalyst from CV plot of figure 4.13a-j at potential of 1.105 V vs RHE was plotted vs scan rate, which resulted into a straight line, and the slope of the straight line was assigned to C_{dl} (Figure 4.14a-j).[23] The C_{dl} of catalyst 7@NGT (1.16 mF) is much better compared to commercial Pt/C (0.79 mF) and other designed catalysts (Figure 4.14a-j and Table 4.3).

The ECS of the selected catalysts was obtained by dividing the C_{dl} with specific capacitance (ESCA=C_{dl}/CS, the CS value in 0.1M KOH lies between 0.025 and 0.035 mF, and we used average value of 0.03 mF).[23] Finally, the roughness factor (RF) was calculated by dividing the obtained EAS by geometrical area of electrode (in C_{dl} experiments the area of electrode is 0.196 cm^2).[22-23]

4.3.7. Fuel Cell Test

The $Co_{1.08}Fe_{3.34}$@NGT catalyst was used as a fuel cell cathode, and its performance in the real system was assessed by membrane electrode assembly (MEA) analysis in the AAEMFC. For the preparation of the cathode, the $Co_{1.08}Fe_{3.34}$@NGT catalyst and commercial ionomer (50 wt%) were well dispersed in isopropyl alcohol (IPA) via sonication. Subsequently, the homogeneous ink of $Co_{1.08}Fe_{3.34}$@NGT (3 mg cm^{-2}) as a cathode and Pt/C (0.4 mg cm^{-2}) as an anode were loaded on the active area of the gas diffusion layer (GDL). The MEA was fabricated by sandwiching the potassium hydroxide doped Tokuyama or Fumatech membrane between cathode and anode. Finally, the MEA was conducted in a single cell mode, which comprises serpentine flow field channels in the graphite plates. The steady-state polarization experiment (cell voltage and power) of the assembled MEA was measured at 60 °C by keeping a humidified flow (100% relative humidity) of hydrogen and oxygen at the flow rates of 200 cc min^{-1}.

Table 4.1. Experimental weight ratio of $FeCl_3$ and Co $(ClO_4)_2.6H_2O$ with 2.2 g of melamine in the synthesized catalysts. In catalyst 11@G, graphene oxide (150 mg) was used instead of melamine. Copyright 2018 John Wiley and Sons.

Catalysts	$FeCl_3$ (g)	$Co(ClO_4)_2.6H_2O$ (g)
1@NGT	0.45	0.45
2@NGT	0.50	0.25
3@NGT	0.25	0.50
4@NGT	0.60	0.30
5@NGT	0.70	0.35
6@NGT	0.80	0.40
7@NGT	0.70	0.45
8@NGT	0.70	0.55
9@NGT	0.70	0.00
10@NGT	0.00	0.70
11@G	0.70	0.45

Table 4.2. The atomic (at.)/weight (wt.) percentage of each element obtained from Elemental analyzer and inductively coupled plasma optical emission spectrometry (ICP-OES). Copyright 2018 John Wiley and Sons.

Catalysts	C (at./wt.%)	N (at./wt.%)	O (at./wt.%)	Fe (at./wt.%)	Co (at./wt.%)
1@NGT	91.92/82.2	2.68/2.8	2.60/3.1	1.61/6.7	1.19/5.2
2@NGT	93.33/85.6	2.80/3.0	1.72/2.1	1.64/7.0	0.51/2.3
3@NGT	91.85/84.49	3.08/3.3	3.19/3.91	0.68/2.9	1.20/5.4
4@NGT	92.04/82.4	3.35/3.5	1.76/2.1	2.19/9.1	0.66/2.9
5@NGT	89.52/77.4	4.07/4.1	2.60/3.0	2.96/11.9	0.85/3.6
6@NGT	88.34/73.8	3.80/3.7	2.97/3.3	3.89/15.1	1.00/4.1
7@NGT	89.84/76.3	3.53/3.5	2.21/2.5	3.34/13.2	1.08/4.5
8@NGT	87.29/72.2	4.67/4.5	2.90/3.2	3.64/14.0	1.50/6.1

4.4. Results and Discussion

4.4.1. Catalyst synthesis

7@NGT is obtained by a one-step carbonization process. In a typical synthetic process, the fine homogeneous mixture of melamine (2.2 g), $Co(ClO_4)_2 \cdot 6H_2O$ (0.45 g), and $FeCl_3$ (0.7 g) is annealed at 750 °C under Ar environment, and then the obtained product is treated with acid and deionized water

to leach away unreacted species (Figure 4.1a and experimental section). To tune the atomic ratio in Co_xFe_y@NGT, the catalysts with different ratios of Co:Fe are synthesized with the same procedure used in 7@NGT (Table 4.1).

4.4.2. Scanning and transmission electron microscopy analysis

7@NGT: The scanning electron microscopy (SEM) and transmission electron microscopy (TEM) images show that 7@NGT consists of bamboo-like nitrogen-rich graphitic tube (NGT) with an encapsulated alloy of CoFe nanoparticles (Figure 4.1b, c). The NGT shows the outer diameter of ≈60 nm originating from the polymerized carbon nitride after melamine polymerization in the presence of iron and cobalt salts at 750 °C (Figure 4.1c). The high-resolution TEM (HR-TEM) images reveal that the CoFe nanoparticles are further wrapped with outer thin layers (1-4 layers) (Figure 4.1d, e and h). The HR-TEM image in Figure 4.1e demonstrates that the lattice fringe of this outer layer around the nanoparticles is 0.34 nm, corresponding to the graphitic carbon,[24] whereas the lattice fringe of wrapped nanoparticles is 0.202 nm, corresponding to the (110) plane of the Co_3Fe_7 alloy. The X-ray diffraction (XRD) analysis of 7@NGT (Figure 4.9a) further explicates that the main dominant phase of the nanoparticles is Co_3Fe_7 with diffraction peaks at 44.73°, 65.10°, and 82.18°, which are attributed to the (110), (200), and (211) facets of Co_3Fe_7 alloy (JCPDS 00-048-1816). The wide and weak diffraction peak at 26.30° with an interlayer spacing of 0.34 nm is ascribed to the (002) plane of crystalline graphitic carbon (JCPDS 01-075-1621). The TEM–energy-dispersive X-ray (TEM-EDX) shows that the NGT is composed of C and N and encapsulates nanoparticles of Co and Fe alloy (Figures 4.1g and 4.2). The line profiles for a single particle in high-angle annular dark-field scanning TEM (HAADF–STEM) image (Figure 4.1f) show the stronger signal for Fe than Co with the indication of more Fe atoms, which is consistent with the experimental ratio.

5@NGT and 8@NGT: The SEM and TEM images of the catalyst 5@NGT and 8@NGT shows bamboo-like graphite tubes with encapsulated alloy of CoFe nanoparticles (Figure 4.3a, b and 4.4a, b). The HR-TEM images show that the CoFe nanoparticle in both 5@NGT and 8@NGT are wrapped with outer graphene layers (Figure 4.3c and 4.4c). The HRTEM image of individual CoFe nanoparticle in 5@NGT show the lattice fringe of ~0.202 nm, corresponding to the (110) planes of the Co_3Fe_7 alloy (JCPDS 00-048-1816) (Figure 4.3d). While in 8@NGT the lattice fringe of the CoFe nanoparticle is ~0.204 nm corresponding to the (110) planes of the CoFe alloy (JCPDS 00-044-1433) (Figure 4.4d). The element distribution is disclosed by TEM-EDX, showing that the NGT is composed of C and N with nanoparticles of Co and Fe alloy (Figure 4.3f and 4.4f). According to line scans, the encapsulated nanoparticle is the alloy of Fe and Co atoms, in which the concentration of Fe atoms is higher than Co, and the concentration of Co increases with the increase in the Co weight ratio of the catalyst (Figure 4.3e and 4.4e). The main dominant phase of CoFe nanoparticles in 5@NGT and 8@NGT is further explicates by X-ray diffraction analysis (Figure 4.9a). The first peak in all catalysts at $2\theta = 26.30°$ with an interlayer spacing of ~0.34 nm is assigned to crystalline graphitic layers.[25-26] According to XRD

results, the Fe and Co atoms in the synthesized catalyst are present in FeCo alloys form (without any metal oxide), which suggest that all nanoparticles are encapsulated in the metallic state inside the NGT. Furthermore, the XRD signals for catalyst 5-NGT and 8@NGT are matched with the Co_3Fe_7 alloy (JCPDS 00-048-1816), and CoFe alloy (JCPDS 00-044-1433), respectively, which are well consistent with HR-TEM lattice spacing.

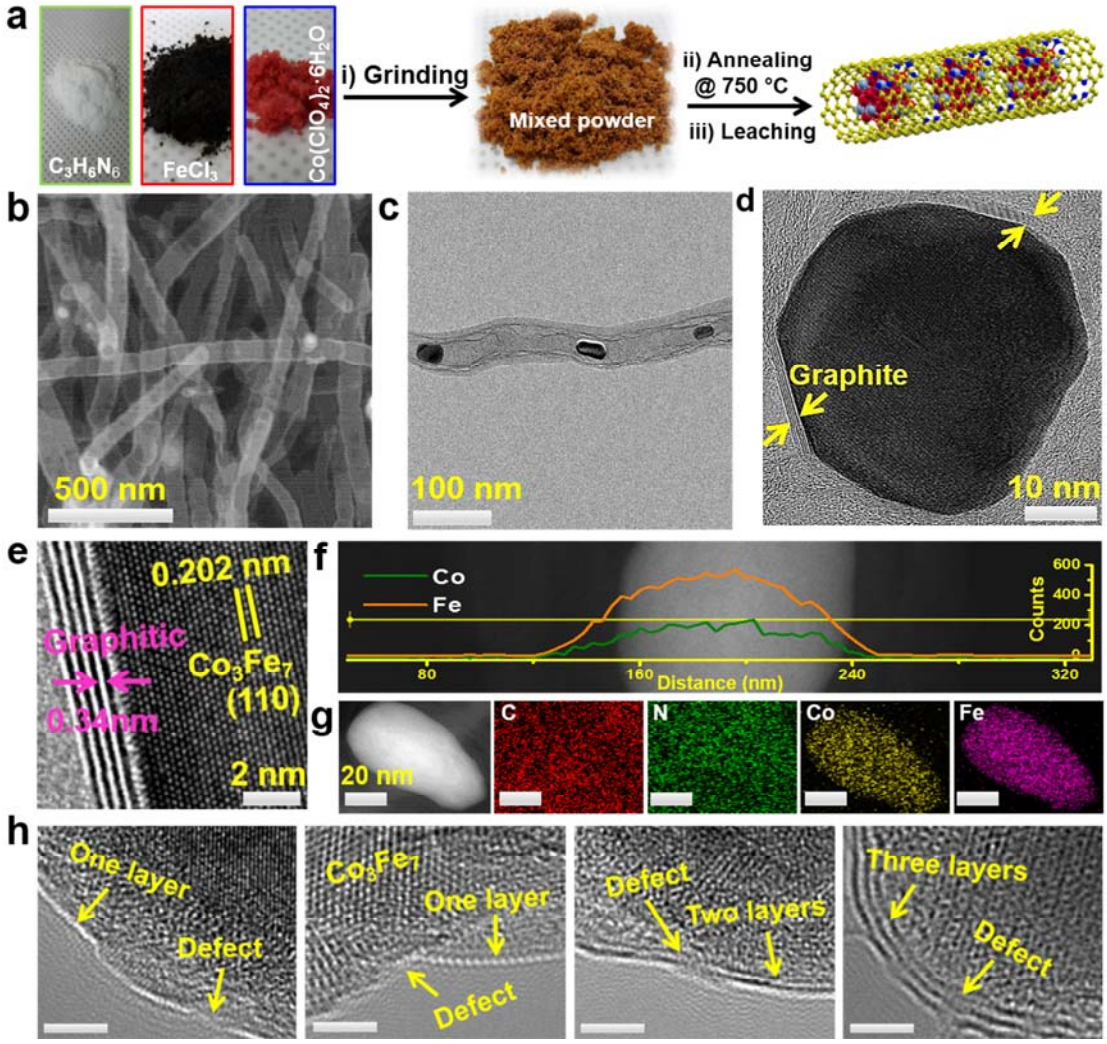

Figure 4.1. Synthetic procedure and physical characterization of 7@NGT. **(a)** Schematic illustration for the synthesis procedure ($Co_{1.08}Fe_{3.34}$@NGT) (C: yellow, Fe: red, Co: silver, N: blue). **(b)** SEM image. **(c)** TEM image of NGT with encapsulated FeCo alloy. **(d)** HR-TEM of FeCo alloy inside NGT. **(e)** HR-TEM image showing the presence of Co_3Fe_7 alloy. **(f)** HAADF–STEM image and the cross-sectional compositional profiles. **(g)** HAADF–STEM images with elemental mapping of C, N, Co, and Fe. **(h)** HR-TEM images for the number of outer layers and defect in graphite of 7@NGT. (Scale bare = 2 nm). Copyright 2018 John Wiley and Sons.

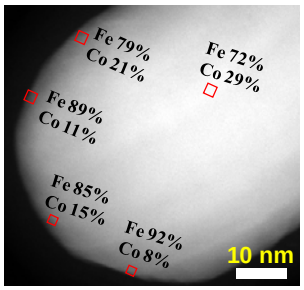

Figure 4.2. TEM-EDX image. Percentage composition of Fe and Co at different point of FeCo alloy in 7@NGT obtained from TEM-EDX. Copyright 2018 John Wiley and Sons.

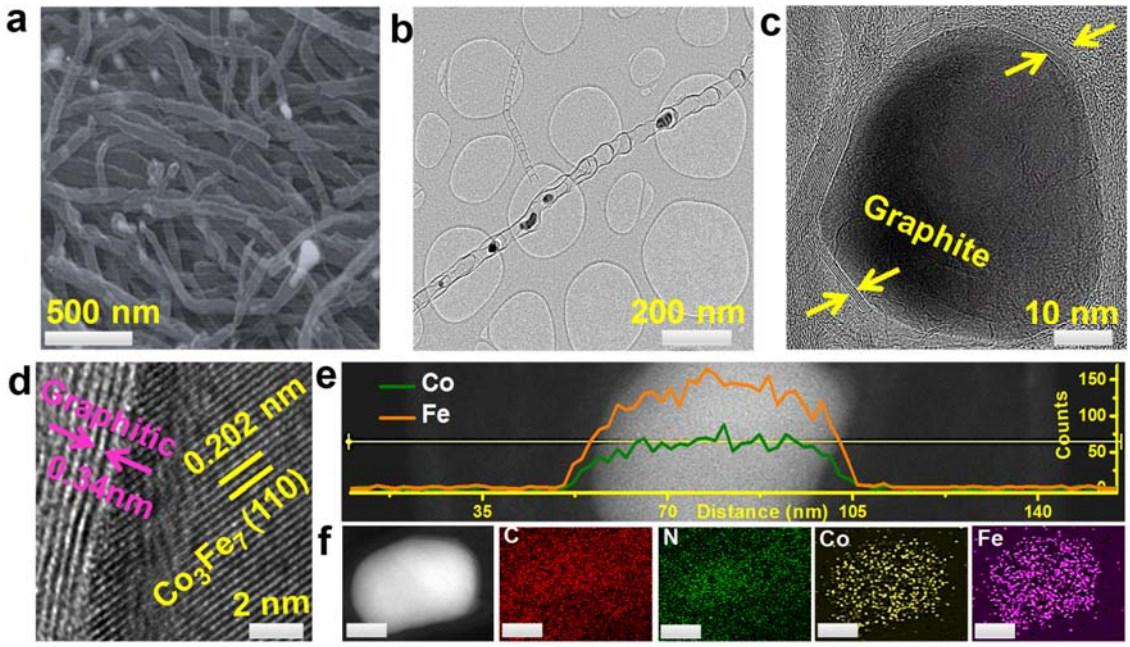

Figure 4.3. SEM, TEM, HR- TEM images, EDX line scan, HAADF- STEM and TEM-EDX analysis of 5@NGT. **(a)** SEM image. **(b)** TEM image. **(c)** HR-TEM of FeCo alloy inside NGT**,** which is further wrapped in 2 nm thick graphitic layers**. (d)** HR-TEM image showing the presence of Co_3Fe_7 alloy. **(e)** HAADF–STEM image and the cross-sectional compositional profiles of the Fe and Co. **(f)** HAADF–STEM images with elemental mapping of C, N, Co and Fe in 5@NGT. The scale bar is 20 nm. Copyright 2018 John Wiley and Sons.

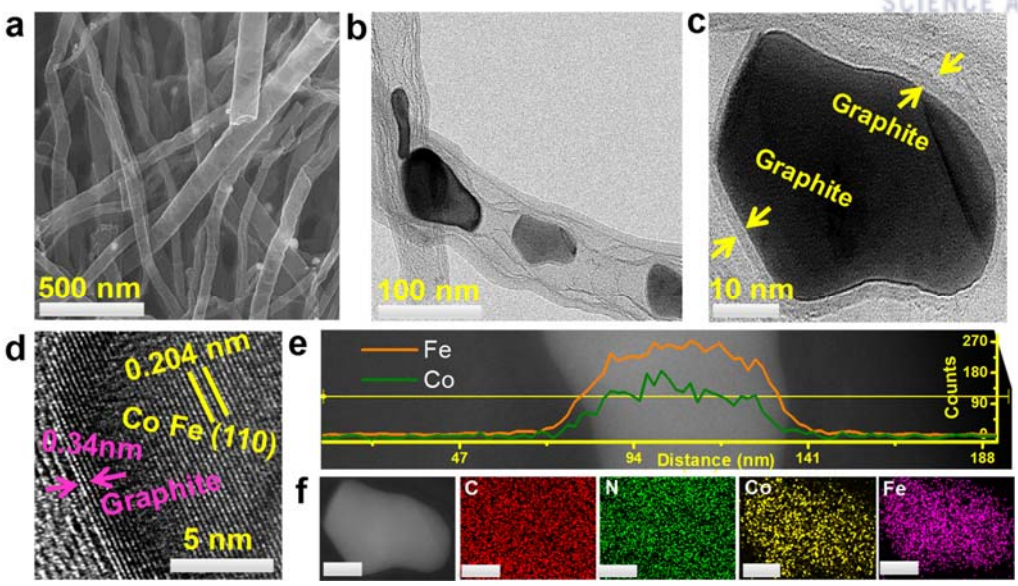

Figure 4.4. SEM, TEM, HR- TEM images, EDX line scan, HAADF- STEM and TEM-EDX analysis of 8@NGT. **(a)** SEM image. **(b)** TEM image. **(c)** HR-TEM of FeCo alloy inside NGT**.** which is further wrapped in 3.4 nm thick graphitic layers. **(d)** HR-TEM image showing the presence of CoFe alloy. **(e)** HAADF–STEM image and the cross-sectional compositional profiles of the Fe and Co. **(f)** HAADF–STEM images with elemental mapping of C, N, Co and Fe in Catalyst 8@NGT. The scale bar is 20 nm. Copyright 2018 John Wiley and Sons.

4.4.3. X-ray photoelectron spectroscopy and absorption fine structure analysis

7@NGT: The valence state of each constituent element in 7@NGT is examined by X-ray photoelectron spectroscopy (XPS). The high resolution XPS spectra of C, N, Co, and Fe in 7@NGT are shown in figure 4.5. In the core-level XPS C 1s spectrum, the main sharp and strong peak located at 284.5 eV corresponds to the graphitic carbon, while the peak centered at 285.8 eV is assigned to C-N and C-N bonds originating from g-C_3N_4 (Figure 4.5a).[27-28] The core-level XPS N 1s spectrum is deconvoluted into three peaks with binding energies of 398.3, 399.6, and 401.1eV, which is attributed to pyridinic-N, metal–N moiety, and graphitic-N, respectively (Figure 4.5b).[29-30] The Co 2p spectrum exhibits two pairs of peaks (Figure 4.5c). The peaks with the binding energies of 779.1 and 793.9 eV are assigned to zero valence Co atom in CoFe alloy,[31] while the peaks centered at 781.6 and 796.4 eV with shakeup satellites (785.2 and 802.7 eV) correspond to Co-N species.[31] Similarly, the core-level XPS of Fe 2p shows metallic state peaks at binding energies of 707.4 and 720.1 eV and ionic state peaks at binding energies of 710.9 and 724.8 eV with shakeup satellite peaks at 714.4 and 732.5 eV, which are attributed to CoFe alloy nanoparticles and Fe-N, respectively (Figure 4.5d).[32-33] The peaks position of C, N, Fe and Co in the XPS spectra of 5@NGT and 8@NGT are almost similar to that of 7@NGT (figures 4.6 and 4.7).

The Fourier transform extended X-ray absorption fine structure (FT-EXAFS) analysis of cobalt in 7@NGT (Figure 4.5e) exhibits the first peak at 1.65 Å, corresponding to Co-N bond distance and the

second peak at 2.31 Å assigned to the Co-Co bond distance, referring to Co foil.[34-35] The next three peaks at 3.11, 3.59, and 4.48 Å are derived from multiple Co-Co-Co scattering. Similarly, FT-EXAFS spectra of iron in 7@NGT (Figure 4.5f) exhibit the first peak at 1.45 Å corresponding to Fe-N bond distance, and the second peak at 2.21 Å is assigned to Fe-Fe bond distance.[29-30]

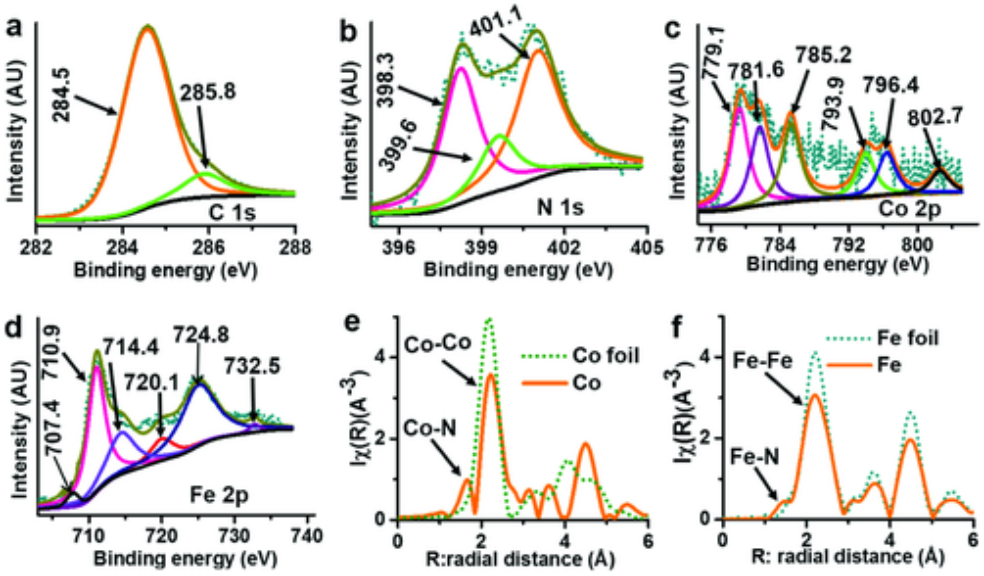

Figure 4.5. X-ray photoelectron spectroscopy (XPS) and X-ray absorption analysis of 7@NGT ($Co_{1.08}Fe_{3.34}$@NGT). The core level XPS spectra for constituent elements: **(a)** C 1s, **(b)** N 1s, **(c)** Co 2p, and **(d)** Fe 2p. **(e, f)** Fourier transform of the EXAFS spectra in *R*-space at Co K and Fe K-edges (AU = arbitrary units). Copyright 2018 John Wiley and Sons.

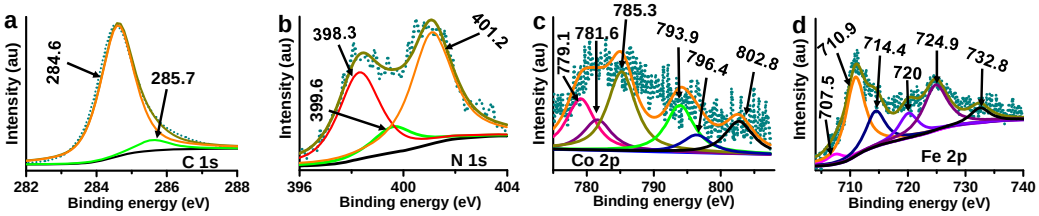

Figure 4.6. The core-level XPS spectra for **(a)** C 1s. **(b)** N 1s. **(c)** Co 2p. **(d)** Fe 2p of Catalyst 5@NGT. Copyright 2018 John Wiley and Sons.

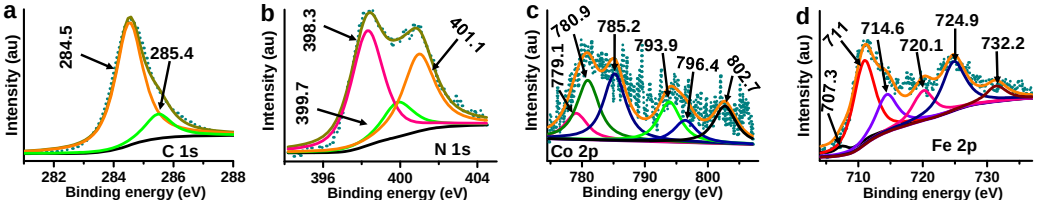

Figure 4.7. The core-level XPS spectra for **(a)** C 1s. **(b)** N 1s. **(c)** Co 2p. **(d)** Fe 2p of 8@NGT Copyright 2018 John Wiley and Sons.

4.4.4. BET Surface Area Analysis

The specific surface area and pore volume are examined via the Brunauer–Emmett–Teller (BET) technique (Figure 4.8a, b). 7@NGT exhibits a specific surface area of 235 m^2 g^{-1} and displays type IV isotherm. In hysteresis loop of isotherm curve, the relative pressure (P/P_0) ranges from 0.45 to 0.99, demonstrating the presence of mesoporous.[36] The Barrett–Joyner–Halenda (BJH) pore size distribution curve further confirms the existence of mesoporous structure with a pore diameter centered at 4.8 nm (Figure 4.8b). This large specific surface area and mesoporous structure of the catalyst are very useful in the exposure of active catalytic sites and the diffusion of electrolyte during the catalytic reactions.

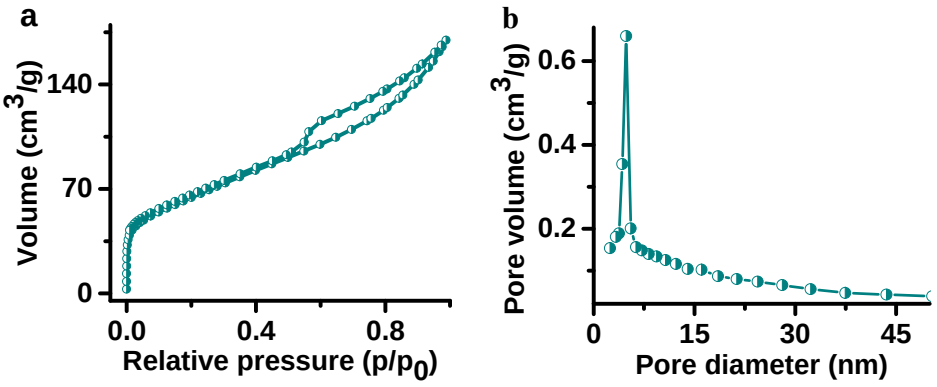

Figure 4.8. BET surface area. **(a)** Nitrogen adsorption-desorption isotherms. **(b)** Barrett–Joyner–Halenda (BJH) pore size distribution of the catalyst 7@NGT. Copyright 2018 John Wiley and Sons.

4.4.5. Raman spectroscopy Fourier-transform infrared Analysis

The Raman spectra show three peaks at 1353 (D-band), 1586 (G-band), and 2696 cm^{-1} (2D band) (Figure 4.9b). The D-band relates to sp^3 disordered and defect sites, and G-band corresponds to hybridized to sp^2 graphitic carbon layer, while the 2D band represents the existence of graphene-like sheets. Moreover, the number of defects and disordered sites in the carbon structure which correspond to active catalytic sites in ORR reaction can be estimated from the relative peak intensity ratio of D to G bands (I_D/I_G).[36-37] The calculated I_D/I_G value of 7@NGT is larger (1.05) than the other synthesized catalysts (Figure 4.9b) demonstrating that 7@NGT has more defects in the graphitic shell, which is well consistent with HR-TEM images (Figure 4.1h). Fourier-transform infrared spectroscopy (FT-IR) analysis was used to find the functional groups in the synthesized catalysts (Figure 4.9c**)**. The FT-IR spectra show one main peak at 1210 cm^{-1} assigned to the C–OH bonds and another main peak at 1566 cm^{-1} attributed to C=C bonds which are associated with the skeletal vibration of the graphitic-like layers.[38] FT-IR results demonstrate the presence of graphitic layers in all catalysts, which is consistent with HR-TEM images and XRD spectra.

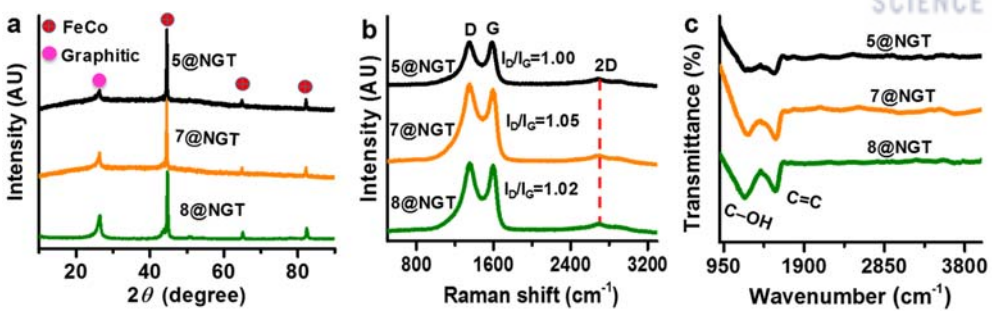

Figure 4.9. XRD, Raman, and FTIR analysis at room temperature of 5@NGT, 7@NGT, and 8@NGT. **(a)** XRD. **(b)** Raman spectra. **(c)** FTIR spectra. (AU = arbitrary units). Copyright 2018 John Wiley and Sons.

4.4.6. Electrochemical analysis

The electrocatalytic activities for ORR of all as-synthesized catalysts are assessed by RDE in an oxygen-saturated 0.1M KOH solution and compared with a 20% commercial Johnson Matthey Pt/C catalyst. The linear sweep voltammetry (LSV) curve of 7@NGT exhibits more positive onset potential of 1.03 V (the potential at which the reaction of ORR starts) and half-wave potential of 0.94 V than other synthesized catalysts and Pt/C as shown in figures 4.10a and 4.11a-c. The limiting current density (≈7.4 mA cm^{-2}; Figure 4.10a) outperforms that of Pt/C (≈5.8 mA cm^{-2}; Figure 4.10a). Furthermore, the obtained ORR by LSV curve (Figurea 4.10 and 4.11) is far superior in all potential regions of kinetic range (>0.9 V), mixed range (0.9–0.8 V), and mass transfer range (<0.8 V) to commercial Pt/C and other synthesized catalysts, representing its superior ORR activity. For the electrochemical reaction, the catalyst having a high current density at a low overpotential should have a smaller Tafel slope value.[30] As shown in figure 4.10c, 7@NGT exhibits the Tafel slope of ≈44 mV dec^{-1}, much smaller than that of commercial Pt/C (≈66 mV dec^{-1}), representing it as a highly active catalyst for ORR.

To understand the ORR mechanism in 7@NGT more quantitatively, we performed RRDE tests at a rotation speed of 1600 rpm in oxygen-saturated 0.1M KOH. Generally, the ORR can proceed via two-electron pathways, where oxygen molecules are reduced to peroxide and subsequently to water, or via four-electron pathways in which oxygen molecules are reduced directly to water. The ORR process proceeded through two-electron pathways in fuel cells is detrimental, because the resulting peroxide leads to cell corrosion and eventually decreases the efficiency of the fuel cell. The number of electrons transferred in 7@NGT is ≈4.0, similar to that of commercial Pt/C (Figure 4.10d), suggesting that 7@NGT catalyzes the ORR process in a four-electron pathway. Furthermore, figure 4.10d from RRDE measurement reveals that the evolution of peroxide (HO_2^-) during ORR process is strikingly suppressed. The percentage yield of HO^{2-} on 7@NGT is less than 2.4 and lower than that of Pt/C, demonstrating that 7@NGT is directly reducing oxygen molecule to water with high efficiency, which is very useful for fuel cell application. Suppression of the HO^{2-} yield on 7@NGT is further confirmed from the plot

of k_1/k_2 ratio (Figure 4.12b) in which k_1 corresponds to the direct reduction of O_2 to water, while k_2 corresponds to O_2 reduction through HO^{2-}. The k_1/k_2 ratio is in the range of ≈44 (Figure 4.12b), which is the highest among the reported values, suggesting that in this study the direct reduction of O_2 to H_2O via four-electron pathway is more facile than two-electron pathway.[39-40]

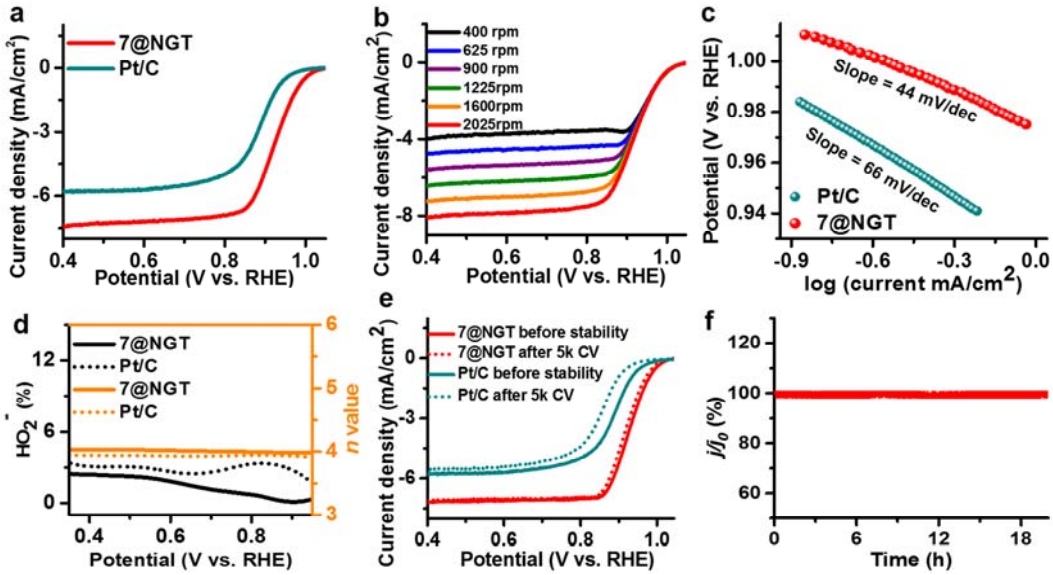

Figure 4.10. Electrochemical performance of 7@NGT compared with Pt/C. **(a)** Room-temperature RDE polarization curves in 0.1M oxygen-saturated KOH solution with a scan rate of 10 mV s^{-1} after subtraction of background measured in 0.1M nitrogen-saturated KOH solution. **(b)** RDE in 0.1M oxygen-saturated KOH solution with a scan rate of 10 mV s^{-1} at different rotation rates. **(c)** Tafel plots calculated from RDE polarization curves. **(d)** HO^{2-} % yield for oxygen reduction reaction and the number of transfer electrons (*n*) measured by the RRDE method. **(e)** RDE polarization curves after 5000 CV scans. **(f)** Chronoamperometric response of 7@NGT in oxygen-saturated 0.1M KOH solution. Copyright 2018 John Wiley and Sons.

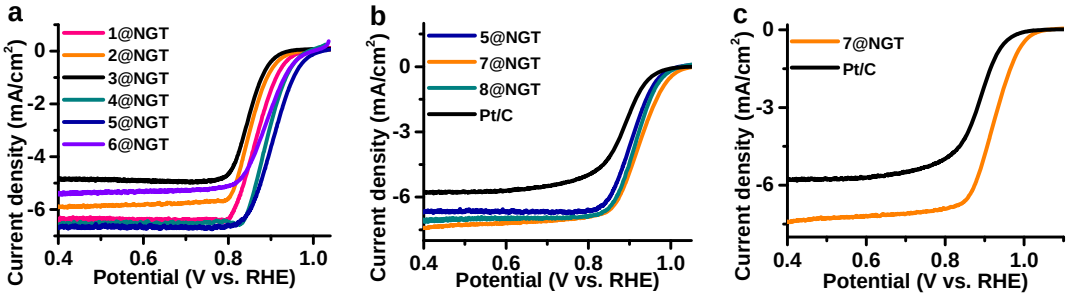

Figure 4.11. Oxygen reduction reaction (ORR) activities in 0.1M KOH solution. **(a)** Comparison of ORR activities of 1@NGT to 6@NGT, which showing the optimization of Co and Fe weight ratio and their total weight amount in Co_xFe_y. **(b)** Comparison of ORR activity of Catalyst 5@NGT, 7@NGT and 8@NGT, which showing the optimization of Co at fixed weight ratio of Fe in Co_xFe_y. **(c)** Comparison of ORR activities of 7@NGT and commercial Pt/C. "1=$Co_{1.19}Fe_{1.61}$, 2=$Co_{0.51}Fe_{1.64}$, 3= $Co_{1.20}Fe_{0.68}$, 4=$Co_{0.66}Fe_{2.19}$, 5=$Co_{0.85}Fe_{2.96}$, 6=$Co_{1.00}Fe_{3.89}$, 7 = $Co_{1.08}Fe_{3.34}$, and 8 =$Co_{1.50}Fe_{3.64}$."

The ORR kinetics of 7@NGT is evaluated from RDE tests at different rotation speeds ranging from 400 to 2025 rpm. The diffusion saturated current density increases with respect to the rotation rate, because at higher speed the diffusion distance of oxygen saturated solution is shortened (Figure 4.10b), which improves the mass transport efficiently. The Koutecky-Levich (K-L) plots obtained from RDE tests show good linearity and parallelism (Figure 4.12a), demonstrating the first-order reaction kinetics toward the dissolved oxygen concentration in the solution and the similar number of electrons transferred during the ORR reaction at different potentials. The number of electrons transferred is ≈4.08 between the potential of 0.82 and 0.90 V (Figure 4.12a), which matches well with the RRDE result. This high activity of 7@NGT is ascribed to alloying effect. Alloying two transition metals induce favorable changes in intrinsic properties by altering the density of state (DOS) at the Fermi level of the metallic sites, which plays an essential role in determining their enhanced catalytic activity.[41-43] Moreover, graphitic layer efficiently confines the FeCo alloy nanoparticles in a limited space to avoid agglomeration.

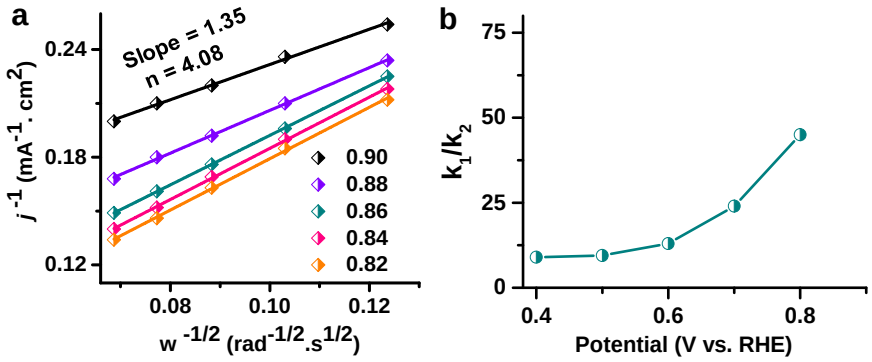

Figure 4.12. (a) K-L plots (J^{-1} versus $w^{-1/2}$) at different potentials ratio of 7@NGT. **(b)** The k_1/k_2 ratio of 7@NGTcalculated from RRDE measurements at potential of 0.4-0.8V. Copyright 2018 John Wiley and Sons.

To further confirm the high activity of 7@NGT compared to commercial Pt/C and other synthesized catalysts, we calculate electrochemical active sites (EAS) and roughness factor (RF) from electrochemical double-layer capacitance (C_{dl}) [22-23] (Figures 4.13a-j, 4.14a-j, and Table 4.3). The EAS and RF valves of 7@NGT (38.67 cm^{-2} and 197.28) are much better than the commercial Pt/C (26.35 cm^{-2} and 134.43) and other synthesized catalysts (Figure 4.14 a-j and Table 4.3), which strongly supports our experimental observations that tuning the atomic weight ratio of Fe to Co in Fe_xCo_y@NGT can dramatically alter the ORR activity of Fe_xCo_y@NGT catalysts. Furthermore, to find the active sites in 7@NGT, we examined the ORR activity of FeCo@G (G: graphene; in this catalyst we use graphene oxide as a supporting material instead of melamine), Co@NGT, Fe@NGT, and **7**@NGT in 0.1M oxygen-saturated KOH with/without 10×10^{-3} m KCN (Figure 4.15a, b), because it is well known that CN^- ions can poison metals and metal-N active sites of ORR.[30, 44] The ORR activity in the absence of

CN^- ions is in the order of 7@NGT > Fe@NGT > Co@NGT > Fe_xCo_y@G (Figure 4.15a, b). It can be seen in figure 4.15a, b that significant decreases in both $E_{1/2}$ and current density of Fe_xCo_y@G, Co@NGT, Fe@NGT, and 7@NGT are observed in KOH solution having KCN, which suggests that the metals and metal-N active sites are blocked by CN^- ions. The decreases in $E_{1/2}$ of CoFe@G, Co@NGT, Fe@NGT, and 7@NGT are 191, 41, 73, and 77 mV, respectively, representing that CN^- ions have a less poisoning effect on the Co center compared to Fe. These control experiments with CN^- ions clearly demonstrate that Fe-N, Co-N, and FeCo are the active centers for ORR in 7@NGT. Since the number of graphitic layers enclosing metal alloys is only 1-4 (Figure 4.1h), the ORR activity is governed by core metal alloys in addition to the N-doped graphitic carbon skeleton. Given that the graphitic carbon skeleton effects are similar for all NGT systems; the inner metal alloys would play a significant role in the ORR activity. The ORR results of Fe_xCo_y@G, Co@NGT, Fe@ NGT, and 7@NGT without CN^- ions show that the active sites should be in the order of Fe_xCo_y-N-C > Fe-N-C > Co-N-C >FeCo alloy. As the FeCo alloy in Fe_xCo_y@G gives very small ORR activity (Figure 4.15b), the Co/Fe-N-C coordination in 7@NGT is likely to be ORR active sites and the FeCo alloy can dramatically enhance the activity of the neighboring Fe-N and Co-N coordination for ORR.[30]

Long-term stability of the ORR catalyst is another important critical index in practical fuel cell applications. To evaluate the ORR stability of 7@NGT, the accelerated durability tests (ADTs) for 5000 cyclic voltammetry (CV) cycles are performed in a potential range of 0.6–1.0 V versus reversible hydrogen electrode (RHE) in 0.1M oxygen-saturated KOH solution at a scan rate of 50 mVs^{-1}. For comparison, the durability test of commercial Pt/C under similar conditions is also conducted. There is no obvious shift in the LSV curve before and after 5000 CV cycles for 7@NGT, while Pt/C shows ≈45 mV degradation in its half-wave potential (Figure 4.10e). The long-time durability of 7@NGT is further examined by the chronoamperometric response at a potential of 0.87 V versus RHE in 0.1M oxygen-saturated KOH solution, which shows constant current density for 20 h (Figure 4.10f). The high stability and durability of 7@NGT are due to in situ generation of core-shell from graphitic carbon. The graphitic layer protects FeCo alloy nanoparticles from corrosion of electrolyte, avoiding the process of the dissolution and re-deposition during electrochemical ORR testing. The morphological stability of this catalyst after durability test is analyzed by TEM, HR-TEM, and TEM-EDX, which shows similar hybrid morphologies to those before stability test (Figure 4.16). For industrial fuel cell application, the ORR catalysts will be highly robust toward methanol (MOH) fuel; therefore, it is crucial to check the MOH tolerance of ORR catalysts.[44] Dramatic change in the current density of Pt/C is detected with the injection of 3M MOH in 0.1M O_2-saturated KOH solutions, while no obvious change in the current density of 7@NGT is observed under similar experimental conditions (Figure 4.17). These experimental observations disclose that compared to commercial Pt/C, 7@NGT has better MOH tolerance and higher selectivity toward ORR.

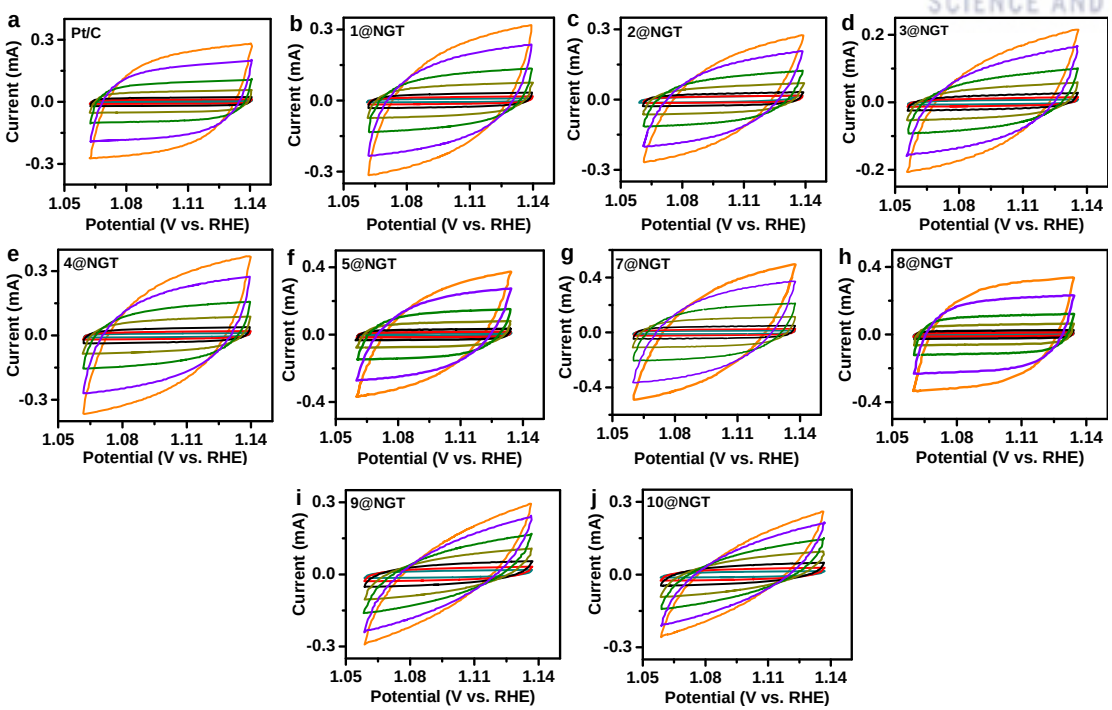

Figure 4.13. Capacitive CV profile recorded in non-Faradaic region with scan rates of 5, 10. 20, 50, 100, 20, 300 mVs^{-1} in 0.1M N_2 saturated KOH solution of **(a)** 20 % commercial Pt/C. **(b-j)** 1@NGT-10@NGT. Copyright 2018 John Wiley and Sons.

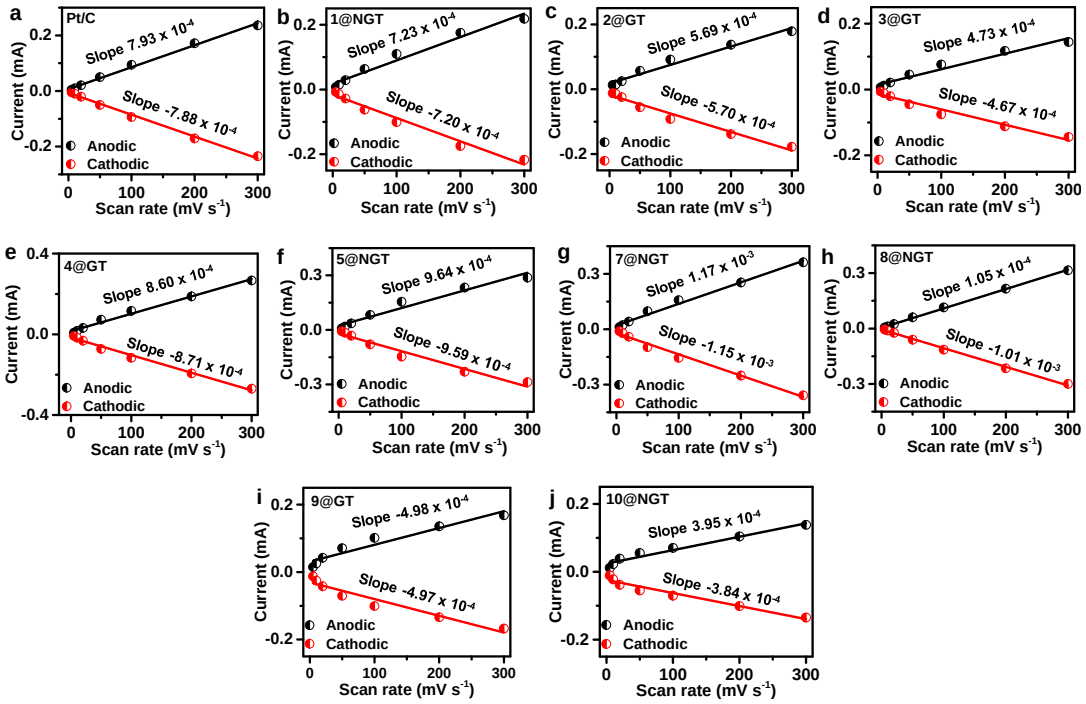

Figure 4.14. Cathodic and anodic current (mA) vs scan rates (mVs^{-1}) obtained from capacitive CV profile at potential of 1.105 V vs RHE of **(a)** 20 % commercial Pt/C. **(b-j)** 1@NGT-10@NGT. Copyright 2018 John Wiley and Sons.

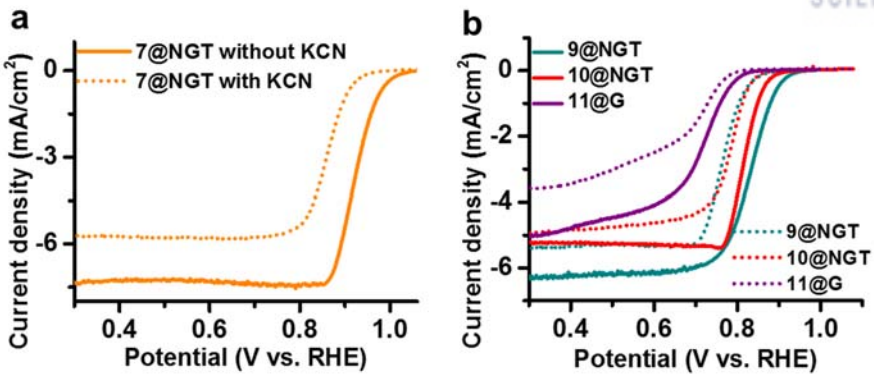

Figure 4.15. ORR activities in 0.1M KOH solution with and without KCN of **(a)** 7@NGT. **(b)** 9@NGT, 10@NGT, 11@G.Solid lines (ORR activities without KCN), dash lines (ORR activities with KCN). 9@NGT=Fe@NGT, and 10@NGT=Co@NGT, 11@G (In the 11-G graphene oxide was used as a supporting material instead of melamine). Copyright 2018 John Wiley and Sons.

Table 4.3. double-layer capacitance (C_{dl}), electrochemically active sites (EAS) and roughness factor (RF). Copyright 2018 John Wiley and Sons.

Catalysts	C_{dl} (mF)	EAS (cm^2)	RF
Pt/C	0.79	26.35	134.43
1@NGT	0.72	24.00	122.44
2@NGT	0.57	19.00	96.94
3@NGT	0.47	15.60	79.93
4@NGT	0.87	28.87	147.28
5@NGT	0.96	32.06	163.57
7@NGT	1.16	38.67	197.28
8@NGT	1.03	34.33	175.17
9@NGT	0.50	16.58	84.60
10@NGT	0.39	12.98	66.24

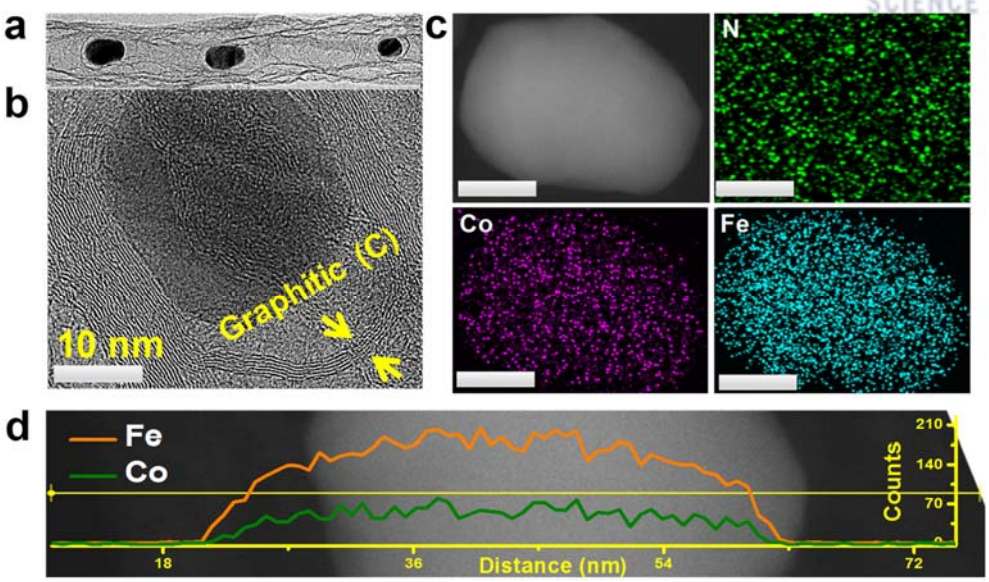

Figure 4.16. TEM, HR-TEM images, EDX line scan, HAADF- STEM and TEM-EDX analysis of 7@NGT after durability test: **(a)** TEM image representing that tube-like morphology of the 7@NGT catalyst is retained after long term durability test. **(b)**HR-TEM of FeCo alloy inside NGT**,** which is still wrapped in outer graphite layers **(c)** HAADF–STEM image with elemental mapping **(d)** HAADF–STEM image and the cross-sectional compositional profiles of Fe and Co. Copyright 2018 John Wiley and Sons.

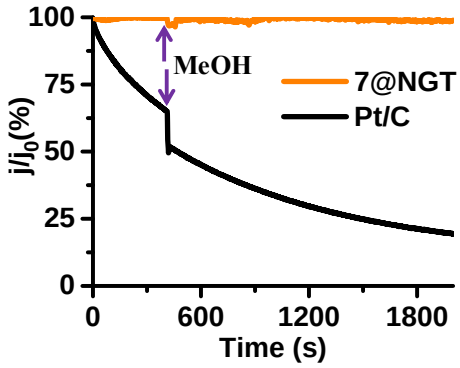

Figure 4.17. Chronoamperometric responses of 7@NGT and Pt/C at 0.84 V in 0.1M O_2-saturated KOH solution before and after 3 M methanol (4 mL of 3 M methanol). Methanol was injected in both 7@NGT and Pt/C at 400 s. Copyright 2018 John Wiley and Sons.

To evaluate the authenticity of 7@NGT in an acidic environment, the ORR activity and stability are conducted in 0.1M O_2-saturated $HClO_4$ solution. In acidic solution it displays a current density of 3 mA cm^{-2} at a similar potential to that of Pt/C catalyst (Figure 4.18a). Moreover, in the same selected potential region it shows similar Tafel slope (39.9 mV dec^{-1}) to that of commercial Pt/C (Figure 4.18b). Interestingly, during 10 h durability tests, 7@NGT exhibited superior stability (no obvious change in

current density) in acidic solution compared to Pt/C (more than 60% decline in the current density) (Figure 4.18c). It also shows high tolerance against MOH in 0.1M O_2-saturated HClO4 solution compared to Pt/C catalyst (Figure 4.18d). The impressive stability, high tolerance against MOH, and similar Tafel slope of 7@NGT to Pt/C in 0.1M O_2-saturated HClO4 validate that its ORR activity is superb not only in basic solution but also in acidic solution.

Overall, the electrochemical activity and stability depend on multiple factors.[36, 45-48] First, Fe-N, Co-N, and sufficient metallic FeCo alloys are inherently better in interacting with reactants (i.e., oxygen/water) than carbon atoms due to the presence of lone-pair electrons, thereby increasing the reactivity of reactants with the hybrid catalyst. Second, the graphitic structure around FeCo alloy with a high degree of carbon graphitization is intrinsically more stable toward oxidation and can well protect the active sites and maintain catalyst activity. The ORR occurring on more active Fe and Co provides an alternate pathway for donating electrons, which enhances the ORR activity and also protects the carbon structure. Third, due to the relatively higher electronegativity of N than that of C, the N dopants in 7@NGT render higher positive charge density on their adjacent carbon atoms, by virtue of which these carbon atoms could become active sites.[45] Finally, the presence of CoFe alloy inside NGT results in decreased local work function on the graphitic surface due to easy electron transfer from core metal alloy to the NGT.[45]

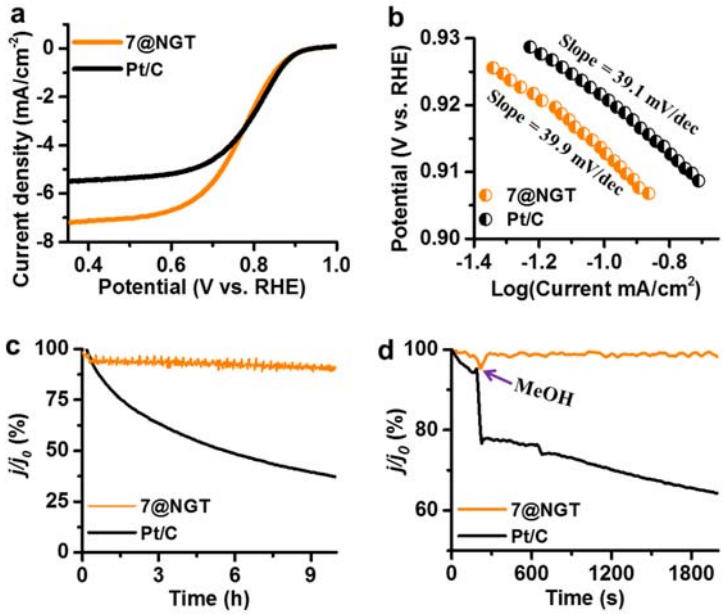

Figure 4.18. ORR activities in 0.1M-oxygen saturated-$HClO_4$ solution. **(a)** RDE polarization curves with a scan rate of 10 mV/s. **(b)** Tafel plots of 7@NGT and Pt/C **(c)** Chronoamperometric response of 7@GT and Pt/C at potential of 0.76 V. **(d)** Chronoamperometric responses of 7@NGT and Pt/C at potential of 0.76 V before and after 3M methanol (4 mL of 3M methanol). Methanol was injected in both 7@NGT and Pt/C at 200 s. Copyright 2018 John Wiley and Sons.

Lastly, for industrial application, the AAEMFC efficiency is evaluated using 7@NGT as an ORR catalyst and Tokuyama or Fumatech membrane as an anion exchange electrolyte. The single cell of 7@NGT shows an open-circuit voltage (OCV) of ≈0.95 V with the maximum power of 117 mW cm^{-2} and a current density of 300 mA cm^{-2} with Tokuyama membrane and a maximum power of 63 mW cm^{-2} and a current density of 188 mA cm^{-2} with Fumatech membrane (Figure 4.19) which are better than that of 40% commercial Pt/C having 0.8 mg cm^{-2} (a maximum power of 60 mW cm^{-2} and current densities of 120 mA cm^{-2} with Fumatech membrane).[8, 23] Additionally, we observe a large voltage drop near 0.95 V due to low conductivity across the membrane. We also note that AAEMFC performance is largely dependent on the kind of anion exchange membrane (Figure 4.19). Therefore, during the fabrication of fuel cell, selection of anion exchange membrane is one of the parameters due to its poor diffusion coefficient of OH^- ions. Thus, further development of an anion exchange membrane with fast OH^- ion transport remains an important issue in obtaining the maximum power and current densities of alkaline anion exchange membrane fuel cells.

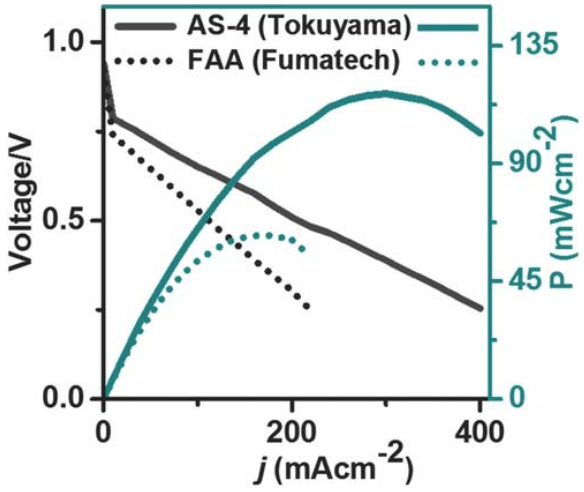

Figure 4.19. Cell voltage and power density versus current of the 7@NGT catalyst as a cathode for AAEMFC using two different membranes. Fuel cell working conditions: temperature (60 °C), fully humidified H_2 and O_2 flow rates (200 cc min^{-1}). To study the effect of membrane, two different membranes of Tokuyama with AS-4 ionomer and Fumatech with FAA ionomer is used for the AAEMFC test. Copyright 2018 John Wiley and Sons.

4.5. Conclusion

In summary, we have synthesized highly active and stable ORR electrocatalysts composed of melamine-derived NGT encapsulating $Co_{1.08}Fe_{3.34}$ alloy with metal-nitrogen bonds in the inside wall of NGT, which exhibits more positive onset potential, half-wave potential, and small Tafel slope than those of commercial Pt/C in basic solution. The four-electron transfer, less HO^{2-} percentage (≈2.4), and

high k_1/k_2 ratio (44) during the ORR process indicated that this catalyst directly reduces oxygen molecule to water with high efficiency. Moreover, in acidic solution this catalyst also shows compatible performance to that of Pt/C and extraordinary stability and methanol tolerance. The remarkable ORR activity of this catalyst could be ascribed to the nitrided $Co_{1.08}Fe_{3.34}$ alloy which favors faster electron movement and higher adsorption of oxygen molecule on the catalyst during catalytic reactions. Meanwhile, our study shows that tuning the Fe/Co nanoparticles in NGT significantly triggered the electrocatalytic active sites in the catalyst, which further enhance the ORR activity. The power density of AAEMFC with this catalyst is 117 mW cm^{-2}. The development of this nonprecious metal-based ORR catalyst not only leads to a significant reduction in fabrication cost of fuel cell but also improves their efficiency.

4.6. Reference

1. Kanan, M. W.; Nocera, D. G., In situ formation of an oxygen-evolving catalyst in neutral water containing phosphate and Co^{2+}. *Science* **2008,** *321* (5892), 1072.
2. Suntivich, J.; et al. Design principles for oxygen-reduction activity on perovskite oxide catalysts for fuel cells and metal–air batteries. *Nature Chemistry* **2011,** *3*, 546.
3. Chai, G.-L.; et al., Active sites engineering leads to exceptional ORR and OER bifunctionality in P,N Co-doped graphene frameworks. *Energy Environ. Sci.* **2017,** *10* (5), 1186-1195.
4. Sengodan, S.; et al., Layered oxygen-deficient double perovskite as an efficient and stable anode for direct hydrocarbon solid oxide fuel cells. *Nat. Mater.* **2014,** *14*, 205.
5. Ahluwalia, R. K.; et al., Kinetics of oxygen reduction reaction on nanostructured thin-film platinum alloy catalyst. *J. Power Sources* **2012,** *215*, 77-88.
6. Greeley, J.; et al., Alloys of platinum and early transition metals as oxygen reduction electrocatalysts. *Nature Chemistry* **2009,** *1*, 552.
7. Niu, J. J.; Wang, J. N., Activated carbon nanotubes-supported catalyst in fuel cells. *Electrochim. Acta* **2008,** *53* (27), 8058-8063.
8. Singh, S. K.; et al., Efficient and durable oxygen reduction electrocatalyst based on CoMn alloy oxide nanoparticles supported over N-doped porous graphene. *ACS Catal.* **2017,** *7* (10), 6700-6710.
9. Pan, J.; Han, J.; Zhu, L.; Hickner, M. A., Cationic side-chain attachment to poly(phenylene oxide) backbones for chemically stable and conductive anion exchange membranes. *Chem. Mater.* **2017,** *29* (12), 5321-5330.
10. Pan, Z. F.; Chen, R.; An, L.; Li, Y. S., Alkaline anion exchange membrane fuel cells for cogeneration of electricity and valuable chemicals. *J. Power Sources* **2017,** *365*, 430-445.
11. Huang, H.-C.; et al., Effect of a sulfur and nitrogen dual-doped Fe–N–S electrocatalyst for the oxygen reduction reaction. *J. Mater. Chem.A* **2017,** *5* (37), 19790-19799.
12. Liu, J.; et al., High performance platinum single atom electrocatalyst for oxygen reduction reaction. *Nat. Commun.* **2017,** *8*, 15938.
13. Tiwari, J. N.; et al., High-affinity-assisted nanoscale alloys as remarkable bifunctional catalyst for alcohol oxidation and oxygen reduction reactions. *ACS Nano* **2017,** *11* (8), 7729-7735.
14. Zhu, C.; Li, H.; Fu, S.; Du, D.; Lin, Y., Highly efficient nonprecious metal catalysts towards oxygen reduction reaction based on three-dimensional porous carbon nanostructures. *Chemical Society Reviews* **2016,** *45* (3), 517-531.
15. Lu, B.; et al., Nitrogen and iron-codoped carbon hollow nanotubules as high-performance catalysts toward oxygen reduction reaction: a combined experimental and theoretical study. *Chem. Mater.* **2017,** *29* (13), 5617-5628.

16. Wang, D.-W.; Su, D., Heterogeneous nanocarbon materials for oxygen reduction reaction. *Energy Environ. Sci.* **2014,** *7* (2), 576-591.
17. Tang, C.; Zhang, Q., Nanocarbon for Oxygen Reduction Electrocatalysis: Dopants, Edges, and Defects. *Adv. Mater.* **2017,** *29* (13), 1604103.
18. Tong, Y.; et al., A bifunctional hybrid electrocatalyst for oxygen reduction and evolution: cobalt oxide nanoparticles strongly coupled to B,N-decorated graphene. *Angewandte Chemie* **2017,** *129* (25), 7227-7231.
19. Lu, Y.; Wang, J.; Peng, Y.; Fisher, A.; Wang, X., Highly efficient and durable Pd hydride nanocubes embedded in 2D amorphous NiB nanosheets for oxygen reduction reaction. *Adv. Energy Mater.* **2017,** *7* (21), 1700919.
20. Li, H.; Ren, C.; Xu, S.; Wang, L.; Yue, Q.; Li, R.; Zhang, Y.; Xue, Q.; Liu, J., Te-template approach to fabricating ternary TeCuPt alloy nanowires with enhanced catalytic performance towards oxygen reduction reaction and methanol oxidation reaction. *J. Mater. Chem.A* **2015,** *3* (11), 5850-5858.
21. Hou, Y.; et al., Ag@CoxP core–shell heterogeneous nanoparticles as efficient oxygen evolution reaction catalysts. *ACS Catal.* **2017,** *7* (10), 7038-7042.
22. McCrory, C. C. L.; et al., Benchmarking hydrogen evolving reaction and oxygen evolving reaction electrocatalysts for solar water splitting devices. *J. Am. Chem. Soc.* **2015,** *137* (13), 4347-4357.
23. Palaniselvam, T.; Kashyap, V.; Bhange, S. N.; Baek, J.-B.; Kurungot, S., Nanoporous graphene enriched with fe/co-n active sites as a promising oxygen reduction electrocatalyst for anion exchange membrane fuel cells. *Adv. Funct. Mater.* **2016,** *26* (13), 2150-2162.
24. Zhao, X.; Hayner, C. M.; Kung, M. C.; Kung, H. H., In-plane vacancy-enabled high-power si–graphene composite electrode for lithium-ion batteries. *Adv. Energy Mater.* **2011,** *1* (6), 1079-1084.
25. Ren, W.; Li, F.; Chen, J.; Bai, S.; Cheng, H.-M., Morphology, diameter distribution and Raman scattering measurements of double-walled carbon nanotubes synthesized by catalytic decomposition of methane. *Chemical Physics Letters* **2002,** *359* (3), 196-202.
26. Venugopal, G.; Krishnamoorthy, K.; Mohan, R.; Kim, S.-J., An investigation of the electrical transport properties of graphene-oxide thin films. *Materials Chemistry and Physics* **2012,** *132* (1), 29-33.
27. Wang, Z.; et al., Cobalt nanoparticles encapsulated in carbon nanotube-grafted nitrogen and sulfur co-doped multichannel carbon fibers as efficient bifunctional oxygen electrocatalysts. *J. Mater. Chem.A* **2017,** *5* (10), 4949-4961.
28. Khabashesku, V. N.; Zimmerman, J. L.; Margrave, J. L., Powder Synthesis and Characterization of Amorphous Carbon Nitride. *Chem. Mater.* **2000,** *12* (11), 3264-3270.
29. Guo, J.; Li, Y.; Cheng, Y.; Dai, L.; Xiang, Z., Highly Efficient Oxygen Reduction Reaction Electrocatalysts Synthesized under Nanospace Confinement of Metal–Organic Framework. *ACS Nano* **2017,** *11* (8), 8379-8386.
30. Jiang, W.-J.; et al., Understanding the high activity of Fe–N–C electrocatalysts in oxygen reduction: Fe/Fe_3c nanoparticles boost the activity of Fe–Nx. *J. Am. Chem. Soc.* **2016,** *138* (10), 3570-3578.
31. Aijaz, A.; et al., Co@Co_3O_4 encapsulated in carbon nanotube-grafted nitrogen-doped carbon polyhedra as an advanced bifunctional oxygen electrode. *Angew. Chem. Int. Ed* **2016,** *55* (12), 4087-4091.
32. Ali-Löytty, H.; et al., Ambient-pressure xps study of a ni–fe electrocatalyst for the oxygen evolution reaction. *J. Phys. Chem. C* **2016,** *120* (4), 2247-2253.
33. Jiang, H.; et al., Iron carbide nanoparticles encapsulated in mesoporous fe–n-doped graphene-like carbon hybrids as efficient bifunctional oxygen electrocatalysts. *ACS Appl. Mater. Interfaces* **2015,** *7* (38), 21511-21520.
34. Zhou, T.; et al., Phosphonate-based metal–organic framework derived co–p–c hybrid as an efficient electrocatalyst for oxygen evolution reaction. *ACS Catal.* **2017,** *7* (9), 6000-6007.
35. Zhou, T.; et al., Nitrogen-doped cobalt phosphate@nanocarbon hybrids for efficient electrocatalytic oxygen reduction. *Energy Environ. Sci.* **2016,** *9* (8), 2563-2570.

36. Huo, L.; et al., 2D layered non-precious metal mesoporous electrocatalysts for enhanced oxygen reduction reaction. *J. Mater. Chem.A* **2017,** *5* (10), 4868-4878.
37. Sim, U.; et al., N-doped monolayer graphene catalyst on silicon photocathode for hydrogen production. *Energy Environ. Sci.* **2013,** *6* (12), 3658-3664.
38. Georgakilas, V.; et al., Multipurpose organically modified carbon nanotubes: from functionalization to nanotube composites. *J. Am. Chem. Soc.* **2008,** *130* (27), 8733-8740.
39. Anju, V. G.; Manjunatha, R.; Austeria, P. M.; Sampath, S., Primary and rechargeable zinc–air batteries using ceramic and highly stable TiCN as an oxygen reduction reaction electrocatalyst. *J. Mater. Chem.A* **2016,** *4* (14), 5258-5264.
40. Chang, S.-T.; et al., Vitalizing fuel cells with vitamins: pyrolyzed vitamin B12 as a non-precious catalyst for enhanced oxygen reduction reaction of polymer electrolyte fuel cells. *Energy Environ. Sci.* **2012,** *5* (1), 5305-5314.
41. Nemoshkalenko, V. V.; et al., Investigation of valence band structures in Cu-Pd alloys. *Solid State Communications* **1975,** *16* (6), 755-757.
42. Wang, Y.; Balbuena, P. B., Design of oxygen reduction bimetallic catalysts: ab-initio-derived thermodynamic guidelines. *J. Phys. Chem. B* **2005,** *109* (40), 18902-18906.
43. Lee, K.; et al., Methanol-tolerant oxygen reduction electrocatalysts based on pd-3d transition metal alloys for direct methanol fuel cells. *J. Electrochem. Soc.* **2006,** *153* (1), A20-A24.
44. Li, Y.; et al., An oxygen reduction electrocatalyst based on carbon nanotube–graphene complexes. *Nat. Nanotechnol.* **2012,** *7*, 394.
45. Yu, D.; Zhang, Q.; Dai, L., Highly efficient metal-free growth of nitrogen-doped single-walled carbon nanotubes on plasma-etched substrates for oxygen reduction. *J. Am. Chem. Soc.* **2010,** *132* (43), 15127-15129.
46. Deng, D.; et al., Iron encapsulated within pod-like carbon nanotubes for oxygen reduction reaction. *Angewandte Chemie* **2013,** *125* (1), 389-393.
47. Chung, H. T.; Won, J. H.; Zelenay, P., Active and stable carbon nanotube/nanoparticle composite electrocatalyst for oxygen reduction. *Nat. Commun.* **2013,** *4*, 1922.
48. Gong, K.; Du, F.; Xia, Z.; Durstock, M.; Dai, L., Nitrogen-Doped Carbon Nanotube Arrays with High Electrocatalytic Activity for Oxygen Reduction. *Science* **2009,** *323* (5915), 760.

Acknowledgement

Foremost, I would like to thank our God Almighty for the wisdom he bestowed upon me, the strength, peace of my mind and good health to complete my PhD program.

I would like to express my deep sense of appreciation to my advisor Prof. Kwang Soo Kim, for his insightful guidance, strong support, great help, fruitful discussions, and supervision throughout my PhD study. I am extremely proud that I did my PhD degree in the supervision of such a knowledgeable professor.

I would also express my appreciation to Dr. Jitendra N. Tiwari for his guidance, great help and helpful discussions. His expertise in electrochemistry has supported me to continue my PhD research on electrocatalysis, which is also sincerely appreciated.

I would like to express my sincere gratitude to my thesis committee members: Prof. Hyeon Suk Shin, Prof. Tae-Hyuk Kwon, Prof. Jong-Beom Baek and Prof. Ji Wook Jang for their kind examination of the PhD thesis and defense.

I am also grateful to friendly behavior and helping nature of my labmates (who are too many to name but all are amazing!) and administrative staff of the center for superfunctional materials UNIST.

Without the financial support from National Honor Scientist Program during the PhD program, my stay at UNIST would not have been possible. I acknowledge their support.

My time at UNIST was made enjoyable in large part due to the Pakistani friends and that became a part of my life. Thanks, guys for all the great times that we have shared in UNIST.

Finally, I would like to thank my parents, brothers, sisters, nephews, nieces and wife for their deep understanding, support, and love. I highly appreciate their patience, sacrifice, and prayers for my success.

The last word goes for Hannan Sultan, my son, whose smiling face always cheers me up. I will always be there for you to hold you, inspire you, guide you, protect you and love you with all my heart.

Publications

1. **Sultan, S.**; Ha, M.; Kim, D. Y.; Tiwari, J. N.; Myung, C. W.; Meena, A.; Shin, T. J.; Chae, K. H.; Kim, K. S., Superb water splitting activity of the electrocatalyst $Fe_3Co(PO_4)_4$ designed with computation-aid. *Nat. Commun.* **2019**, *10* (1), 5195.

2. **Sultan, S.**; Tiwari, J. N.; Singh, A. N.; Zhumagali, S.; Ha, M.; Myung, C. W.; Thangavel, P.; Kim, K. S., Single Atoms and Clusters Based Nanomaterials for Hydrogen Evolution, Oxygen Evolution Reactions, and Full Water Splitting. *Adv. Energy Mater.* **2019,** *9* (22), 1900624.

3. Tiwari, J. N.; Harzandi, A. M.; Ha, M.; **Sultan, S.**; Myung, C. W.; Park, H. J.; Kim, D. Y.; Thangavel, P.; Singh, A. N.; Sharma, P.; Chandrasekaran, S. S.; Salehnia, F.; Jang, J.-W.; Shin, H. S.; Lee, Z.; Kim, K. S., High-Performance Hydrogen Evolution by Ru Single Atoms and Nitrided-Ru Nanoparticles Implanted on N-Doped Graphitic Sheet. *Adv. Energy Mater.* **2019,** *9* (26), 1900931.

4. Meena, A.; Ha, M.; Chandrasekaran, S. S.; **Sultan, S**.; Thangavel, P.; Harzandi, Ahmad M.; Singh, B.; Tiwari, J. N.; Kim, K. S., Pt-like hydrogen evolution on a $V_2O_5/Ni(OH)_2$ electrocatalyst. *J. Mater. Chem.A* **2019,** *7* (26), 15794-15800.

5. **Sultan, S.**; Tiwari, J. N.; Jang, J.-H.; Harzandi, A. M.; Salehnia, F.; Yoo, S. J.; Kim, K. S., Highly Efficient Oxygen Reduction Reaction Activity of Graphitic Tube Encapsulating Nitrided Co_xFe_y Alloy. *Adv. Energy Mater.* **2018,** *8* (25), 1801002.

6. Tiwari, J. N.; **Sultan, S.**; Myung, C. W.; Yoon, T.; Li, N.; Ha, M.; Harzandi, A. M.; Park, H. J.; Kim, D. Y.; Chandrasekaran, S. S.; Lee, W. G.; Vij, V.; Kang, H.; Shin, T. J.; Shin, H. S.; Lee, G.; Lee, Z.; Kim, K. S., Multicomponent electrocatalyst with ultralow Pt loading and high hydrogen evolution activity. *Nat. Energy* **2018,** *3* (9), 773-782.

7. Singh, B. K.; Kim, Y.; Baek, S. B.; Meena, A.; **Sultan, S.**; Kwak, J. H.; Kim, K. S., Template free facile synthesis of mesoporous mordenite for bulky molecular catalytic reactions. *Journal of Industrial and Engineering Chemistry* **2018,** *57*, 363-369.

8. Vij, V.; **Sultan, S.**; Harzandi, A. M.; Meena, A.; Tiwari, J. N.; Lee, W.-G.; Yoon, T.; Kim, K. S., Nickel-Based Electrocatalysts for Energy-Related Applications: Oxygen Reduction, Oxygen Evolution, and Hydrogen Evolution Reactions. *ACS Catal.* **2017,** *7* (10), 7196-7225.

9. Tiwari, J. N.; Lee, W. G.; **Sultan, S**.; Yousuf, M.; Harzandi, A. M.; Vij, V.; Kim, K. S., High-Affinity-Assisted Nanoscale Alloys as Remarkable Bifunctional Catalyst for Alcohol Oxidation and Oxygen Reduction Reactions. *ACS Nano* **2017,** *11* (8), 7729-7735.